UNIVERSIDAD NACIONAL AUTÓNOMA DE MÉXICO

POSGRADO EN ASTROFÍSICA

ASTROFÍSICA TEÓRICA

A MULTI-COMPONENT APPROACH TO MODEL COMPLEX GASEOUS NEBULAE

TESIS

QUE PARA OPTAR POR EL GRADO DE:

DOCTORA EN CIENCIAS (ASTROFÍSICA)

PRESENTA:

VERÓNICA GÓMEZ LLANOS SANDOVAL

TUTOR

DR. CHRISTOPHE MORISSET

INSTITUTO DE ASTRONOMÍA

MÉXICO, ENSENADA B.C., JUNE 2021

JUNIO

Agradecimientos

A Dr. Michael Richer, Dr. César Esteban López, Dra. Mónica Rodríguez Guillen, Dr. William Henney Strutt y Dr. Roger Wesson, les agradezco por aceptar formar parte de mi sínodo, por tomarse el tiempo de revisar mi tesis en detalle y por sus correcciones que mejoraron de forma significativa el nivel de esta tesis.

Agradezco a los proyectos CONACyT-CB2015 254132, DGAPA/PAPIIT-107215 y DGAPA/PAPIIT-101220, por brindarme los apoyos necesarios para mejorar mi crecimiento académico y tener la oportunidad de presentar mi trabajo en congresos nacionales e internacionales.

Así mismo, agradezco a CONACyT por otorgarme los recursos que me permitieron dedicarme de tiempo completo a mis estudios. También a PAEP-UNAM por el apoyo para complementar mi formación académica y participación en congresos.

Al Programa de Posgrado en Astrofísica de la UNAM y al Instituto de Astronomía, en sus sedes de Ciudad Universitaria y Ensenda, por brindarme el espacio adecuado para realizar este trabajo en el mejor ambiente posible. Al personal administrativo de ambas sedes y al director del Instituto, gracias por estar siempre en la mejor disposición para ayudarme con todos los trámites necesarios durante mi formación académica.

A la Dra. Glora Delgado Inglada y al Dr. Alejandro Raga por aceptar ser parte de mi comité tutor, por sus evaluaciones cada semestre, por todos sus comentarios y sugerencias.

A Christophe, por ser el mejor asesor que pude elegir, por ser la guía en este trabajo, por valorar mis ideas y por siempre brindarme de su tiempo. Por preocuparse no solo de mi formación académica sino también de mi bienestar personal, porque me ha enseñado de mucho más que Astrofísica, muchísimas gracias.

A Daniel Pequignot por su trabajo en modelos combinados, que ha sido la base para poder realizar

esta investigación.

A Grazyna Stasińska y Jorge García Rojas, por revisar este trabajo, por sus comentarios que ayudaron a enriquecer esta investigación.

A Hektor Monteiro, por darme un espacio en su Universidad en una estancia que aunque fue bastante corta fue muy enriquecedora y me permitió conocer grandes personas.

A mis amigos Mayra, Liliana, Aguayo, Chimal, Trevor, Eliab, Norberto, René, Aroche, Sheila, Mabel, Alexia, Elizabeth, Luis Garma, Hecsari, Luis Carlos, Genaro, Javier, Manet, Martín, Pancho, Luis Canúl por las pláticas amenas, por ayudarme a resolver dudas, por los paseos en bici, el ejercicio virtual y por brindarme su amistad y hacer mis años de estudiante mucho más amenos.

A toda mi familia, en especial a mis padres por apoyarme y comprender que debía estar lejos para lograr mis metas. A mi hermana Laura, por siempre estar ahí para escucharme y preocuparse por mi, por ser mi inspiración y constante consejera. A mis abuelos y a mi tía Emma, que siempre han creído en mi y me han apoyado.

Contents

Resumen

La realidad siempre será mas compleja que los modelos teóricos que usamos para explicarla. Pero, ¿hasta qué punto se considera un modelo sencillo una buena aproximación? y ¿cuándo es necesario considerar modelos más complejos para entender y reproducir mejor los objetos reales? Si pensamos en objetos extendidos como nebulosas planetarias, regiones H II o incluso galaxias, reproducir en detalle la ionización, las velocidades, la morfología, la transferencia de radiación, puede ser considerablemente complejo si es que posible. En el caso de una nebulosa planetaria, podemos preguntarnos ¿cuándo es un modelo esférico una buena aproximación? (sabemos que gran parte no son esféricas) y ¿en qué casos es necesario aumentar la complejidad de los modelos para acercarnos más a la realidad?. Los modelos 3D son una buena herramienta para reproducir el detalle de los objetos extensos, sin embargo, el tiempo computacional requerido para explorar el espacio de parámetros puede ser muy elevado. Es por eso que modelos topológicamente equivalentes pueden ser una buena alternativa que permita modelar objetos complejos con un menor tiempo de cómputo. En este trabajo se exploran dos maneras de combinar modelos 1D para reproducir dos tipos de regiones fotoionizadas: nebulosas planetarias y regiones H II.

A las regiones de gas en el medio interestelar ionizadas por fotones emitidos en estrellas calientes se les conoce como regiones fotoionizadas. La emissión proveniente de estas regiones puede usarse para obtener las condiciones físicas como densidad y temperatura, así como las abundancias químicas en dichas regiones. Determinar las abundancias químicas del gas expulsado por estrellas evolucionadas de masa baja e intermedia ($<$ 6 - 8 $M_{\odot}$) nos permite conocer los elementos químicos presentes en el momento en que se formó la estrella, así como los elementos que se han generado en el núcleo de la misma. Este tipo de objetos, conocidos como nebulosas planetarias, ayudan a estudiar el pasado químico del gas en el que se formaron. En regiones de formación estelar, las estrellas masivas emiten fotones energéticos que ionizan el gas circundante. A este tipo de objetos se les llama regiones H II

debido a que el hidrógeno (que es el elemento más abundante) suele estar totalmente ionizado. Las regiones H II son objetos jóvenes que permiten conocer la composición química actual del gas al estudiar sus líneas de emisión.

Hay dos problemas importantes en el estudio del gas fotoionizado (nebulosas planetarias y regiones H II). El primero es la diferencia en las abundancias químicas determinadas a partir de líneas de recombinación y líneas de excitación colisional. El segundo es la diferencia, reportada hace más de 50 años, entre la temperatura electrónica que se estima con las líneas de excitación colisional ([O III] λ 4363/λ 5007) y el cociente del salto de Balmer normalizado por una línea de la serie de Balmer. En la primera parte de este trabajo se combinaron modelos suponiendo 2 metalicidades distintas en el gas, con el fin de estudiar su efecto en la emisión de cada región y como puede interpretarse en términos de los problemas de temperaturas y abundancias mencionados. Se generaron modelos de fotoionización, restringiendo los parámetros libres con base en observaciones y modelos previos de la nebulosa planetaria NGC 6153. Se exploraron las diferencias en metalicidad y volumen entre las dos regiones, hasta valores extremos con metalicidades 3 órdenes de magnitud mayores. Se encontró una degeneración entre el volumen y la diferencia en metalicidad. Al comparar con observaciones, se encontraron dos soluciones que reproducen la diferencia en temperatura y abundancia: una con menor metalicidad (2.1 dex) y mayor volumen (<0.5% del volumen total) y otra con mayor metalicidad (2.7 dex) y menor volumen (<0.2% del volumen total). Para las dos soluciones, la región de alta metalicidad ocupa una fracción de volumen menor al 1% del volumen total y su abundancia de oxígeno es entre el 25 y 60% de la abundancia total.

A partir de los resultados obtenidos en la primera parte del trabajo, se realizó un estudio adicional sobre la contribución de la recombinación a la intensidad de la línea de [O III] λ 4363 y su efecto sobre la temperatura cuando se tienen dos componentes de distinta metalicidad, para lo que se usaron observaciones de las nebulosas planetarias Abell 46 y NGC 6778. Se encontró que la contribución debida a recombinación puede ser de hasta el 70% y 40% de la emisión total de [O III] λ 4363.

Finalmente, se muestra una investigación (en fase de desarrollo), donde se utilizan las observaciones de la galaxia NGC 628, observada con el instrumento SITELLE como parte del *survey* SIGNALS. Esta investigación busca determinar parámetros de las regiones H II más brillantes a partir de observaciones con resolución espacial de los cocientes de emisión ([S II] λ 6716 + λ 6731)/Hα y [O III] λ 5007/Hβ, buscando reproducir su comportamiento con modelos de fotoionización pseudo-3D no esféricos.

Abstract

The reality will always be more complex than the theoretical models we use to explain it. Until what point a simple model can be considered a good approximation, and when is it necessary to consider more complex models to understand and reproduce better real objects? If we think of extended objects like planetary nebulae (PNe), H II regions, or even galaxies, reproducing in detail the ionization structure, the velocity field, and the morphology, the exact computation of radiative transfer can be considerably complex, if possible. In the case of PNe, we can wonder when a spherical model is a good approximation (we know most PNe are not spherical), and in which cases it is necessary to increase the complexity of the models to approach reality. 3D modeling can be a good tool to reproduce the detail of complex objects, however, the computational time required to explicitly explore the parameter space can be very high. That is why topologically equivalent models can be a good alternative to allow the modeling of complex objects with less computational time. In this work we explored two ways of combining 1D models, aiming to reproduce two types of photoionized regions: planetary nebulae and H II regions.

The gaseous regions of the interstellar medium that are ionized by photons emitted by hot sources are called photoionized regions. The emission coming from these regions can be used to obtain the physical conditions as electron density and temperature, and also the chemical abundances. Evolved low mass stars (< 6 - 8 $M_{\odot}$) that have expelled their outer layers and of which only the hot compact core remains, allow us to study chemical elements present at the moment of formation of the star, and also the elements generated in its interior. This type of object known as PN, helps us to study the chemical past of the gas in which they were formed. On the other hand, star-forming regions contain stars that are massive enough to emit energetic photons that ionize the surrounding gas. This type of object is known as H II region since hydrogen (the most abundant element) is usually fully ionized. The H II regions are young objects that help us to know the current chemical composition

of gas when studying its emission lines.

There are at least two problems in the study of photoionized gas. The first one is related to the difference in chemical abundances estimated from recombination lines and collisionally excited lines. The second one involves the difference between the electron temperature determined from collisionally excited lines ([O III] λ 4363/λ 5007) and from the Balmer jump normalized to a Balmer line. In the first part of this work, we combine bi-metallicity models to study the effect of the emission of each component and its implications on the open problems on the electron temperature and chemical abundances of the photoionized gas. We generate photoionization models, constraining the free parameters with observations and previous models of the planetary nebula NGC 6153. We explore the differences in metallicity and volume between the two regions and find differences of up to 3 orders of magnitude in the metallicity. A degeneracy was found between the volume and the difference in metallicity. When comparing with observations, two solutions were found that reproduce the differences in temperatures and chemical abundances: one with lower metallicity (log O/H = -1.15) and larger volume ($<$0.5% of the total volume) and the other with higher metallicity (log O/H = -0.55) and smaller volume ($<$0.2% of the total volume). Both solutions have a fraction of volume which is smaller than 1%, and the total amount of oxygen in the metal-rich zone is between 25 y 60% of the total oxygen abundance.

From the results obtained in the first part of this work, an additional study was performed exploring the effects that the contribution of recombination on the intensity of [O III] λ 4363 line has on the electron temperature estimations when two metallicity components are considered. This was done using observations of two planetary nebulae: Abell 46 and NGC 6778. It was found that the contribution of recombination to the total [O III] λ 4363 emission, can be up to 70% y 40%, respectively.

Finaly, we show a research (that is still in progress) based on observations of the galaxy NGC 628, observed using the instrument SITELLE as part of the SIGNALS survey. In this research we aim to determine some parameters of the brightest H II regions by comparing spatially resolved observations of ([S II] λ 6716 + λ 6731)/Hα and [O III] λ 5007/Hβ with non-spherical pseudo-3D photoinization modeling.

Chapter 1

Introduction

Looking at the sky on a dark night one may think that there is nothing between the stars that we see. We know this is not the case, there is gas, dust, and other components between the stars. The baryonic matter between the stars forms what we call the interstellar medium (ISM). From beautiful images like those taken during the 30 years lifetime of the Hubble Space Telescope, we can get a glance of the variety in morphology, ionization structure, brightness and sizes of the different components of the ISM. In figures 1.1 and 1.2 we show the *Pillars of Creation* and the Crab Nebula, respectively, which are some nice examples of the different structures and components that are present in the ISM.

The gas in the ISM can be in different ionization stages from fully ionized to neutral, atomic or molecular, and it can have a large range of physical conditions, such as temperatures and densities that go from $\sim$ 10 K to 10^6 K and $\sim 10^{-3}$ cm^{-3} to 10^5 cm^{-3}, respectively. These parameters will vary according to the conditions of the environment within and surrounding the gas. From the different ionization stages in the ISM we can get information that contributes to our understanding of our Galaxy and other galaxies. Particularly, the gas that is ionized by ultraviolet photons, i.e. photoionized gas, will shine at signature energies that not only can produce a beautiful image (see fig. 1.2) but also can be used to determine the physical and chemical properties of the gas. In this chapter we will explain the key concepts for understanding such regions.

Figure 1.1: Hubble Space Telescope image of the *Pillars of Creation* from Eagle Nebula.

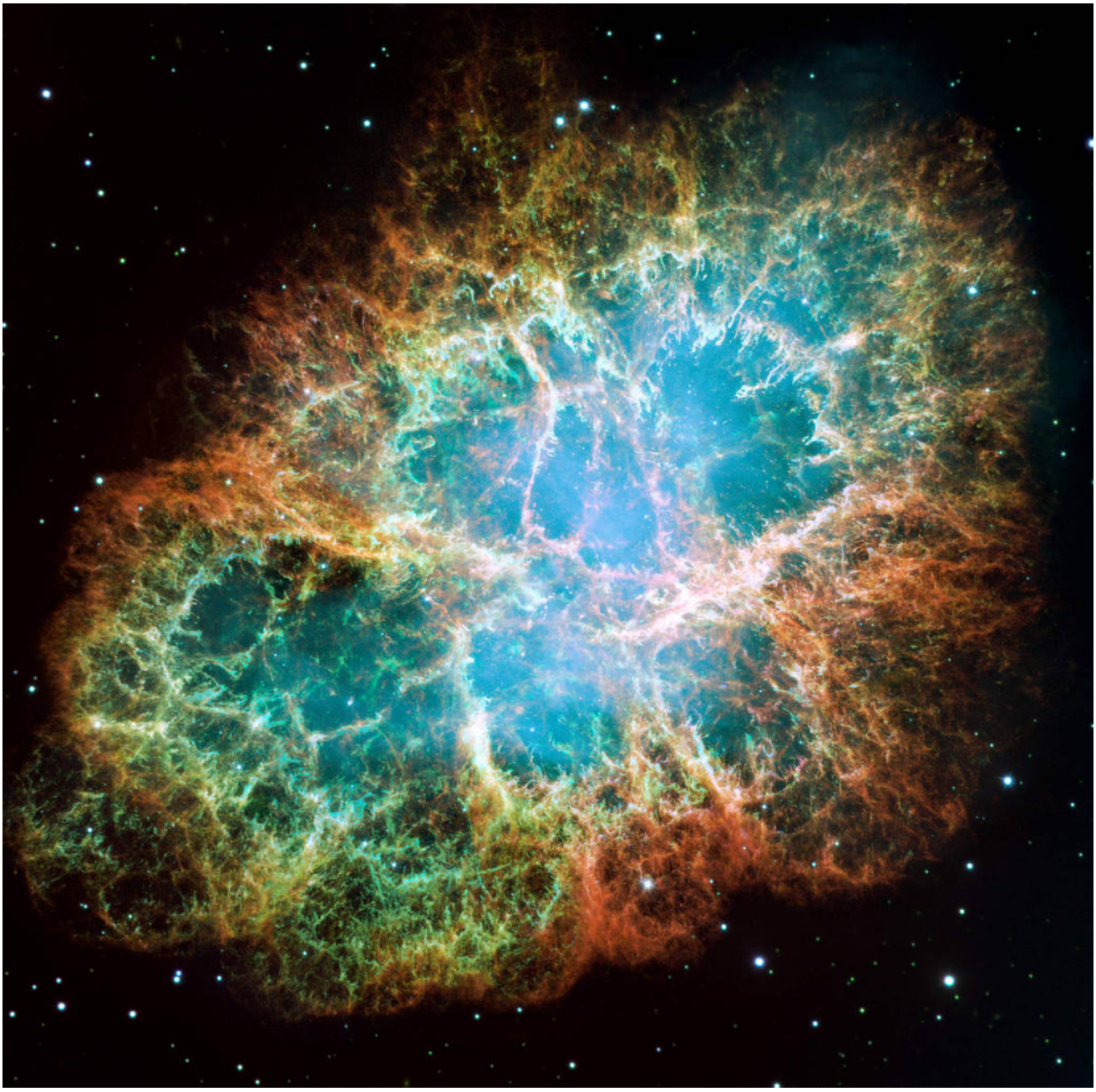

Figure 1.2: Image of the supernova remnant Crab Nebula observed with the Hubble Space Telescope.

1.1 Physics of the photoionized gas

This and the following sections draw on material from Rybicki & Lightman (1981), Osterbrock & Ferland (2006) and Peimbert et al. (2017).

In a neutral gas, the electrons are bound to the nuclei. When an electron receives enough energy to go from a bound to a free state, it becomes a free electron and the remaining part of the atom, now positively charged, is called an ion. An ionized gas (plasma) is mainly composed of free electrons and ions. The temperature of the gas can be represented by the kinetic energy of the free electrons which follows a Maxwell-Bolztmann distribution. The gas can be ionized by shocks or by energetic photons. This work is focused on the study of gas ionized by photons (photoionized gas).

Two important examples of photoionized regions are planetary nebulae (PNe) and H II regions. PNe are evolved low- and intermediate-mass stars ($<$ 6-8 $M_\odot$) that have expelled their outer layers during the final stages of their stellar evolution and only the core of the star remains (white dwarf). This core is very hot and produces photons that ionize the previously released envelope that has swept the surrounding material. H II regions are the hosts of recent stellar formation. The young and massive stars in the H II region dominate the energy production, emitting photons that ionize the gas around them. The size of H II regions can go from ultracompact ($\sim$ 0.01 pc) to giant ($\sim$ 100 pc), so they can have a similar size or be larger than PNe ($\sim$0.1 pc) and have lower densities. The source of ionizing photons can go from a single star to a stellar cluster, but the physics needed to analyze the gas is in principle the same. The physical concepts are detailed in the following sections.

1.1.1 Radiative transfer

The light emitted by near or far away objects in space is measured by the flux received at the telescope. The flux is the energy passing through a surface element from all directions. If the flux is integrated over all wavelengths it has units erg cm^{-2} s^{-1}, and if it is a monochromatic flux, the units can be erg cm^{-2} s^{-1} Hz^{-1}, erg cm^{-2} s^{-1} $Å^{-1}$, or erg cm^{-2} s^{-1} μm^{-1}, if the flux is measured by frequency or by wavelength unit. The specific intensity can be measured when the source is resolved and the solid angle is known. This quantity give us the energy flow per unit area, unit time, frequency range, and solid angle in a given direction. It is a more adequate measurement of the energy since it does not depend on the distance to the object. The units of the specific intensity, $I_\nu(\theta, \varphi)$ are

erg cm^{-2} s^{-1} sr^{-1} Hz^{-1}. The flux and the specific intensity are related by:

$$F_\nu = \int I_\nu \cos\theta d\Omega. \tag{1.1}$$

Other important quantity is the mean intensity, which is defined as:

$$J_\nu = \frac{1}{4\pi}\int I_\nu d\Omega \tag{1.2}$$

it has units erg cm^{-2} s^{-1} sr^{-1} Hz^{-1}. If the radiation field is isotropic, then the specific intensity and the mean intensity are equivalent, i.e. $J_\nu = I_\nu$.

The specific intensity from a source remains constant if no additional light is added or subtracted in the line of sight. The radiative transfer equation describes the changes with the position of the specific intensity due to emission, absorption or scattering of light. If we only consider emission and absorption the equation is as follows:

$$\frac{dI_\nu}{ds} = -\alpha_\nu I_\nu + j_\nu \tag{1.3}$$

the left side of the equation is the change in the specific intensity for a small displacement in the line of sight (ds), the first term of the right side of the equation represents the absorption of light which includes true absorption and stimulated emission, both are proportional to I_ν. The term α_ν is the true absorption coefficient (including absorption and stimulated emission) and has units of cm^{-1}. The second term of the right side of the equation is the spontaneous emission coefficient with units erg cm^{-3} s^{-1} sr^{-1} Hz^{-1}.

Dividing eq. (1.3) by the absorption coefficient, α_ν, we get:

$$\frac{dI_\nu}{d\tau_\nu} = -I_\nu + S_\nu \tag{1.4}$$

where $d\tau_\nu = \alpha_\nu\, ds$ and $S_\nu = j_\nu/\alpha_\nu$ are the differential optical depth and the source function, respectively. The optical depth is a quantity that tell us how opaque or transparent a medium is, and is defined as the integral of the absorption coefficient in the line of sight:

$$\tau_\nu(s) = \int_{s_0}^{s} \alpha_\nu(s')ds' \tag{1.5}$$

with $\tau_\nu(s_0) = 0$.

There are three important cases for the optical depth:

- $\tau_\nu \gg 1$, the medium is optically thick or opaque and a photon of frequency ν can not go through the whole medium without being absorbed.
- $\tau_\nu \approx 1$, part of the radiation is absorbed, and part is escaping the gas.
- $\tau_\nu \ll 1$, the medium is optically thin or transparent and a photon of frequency ν can go through the whole medium without being absorbed.

1.1.2 Photoionization equilibrium

In stationary-state models of photoionized nebulae, a balance is often assumed between photoionization and recombination (for every atom and ion). This assumption is valid when the ionizing radiation continuum and the geometry of the plasma change at larger timescales than the ionization equilibrium timescales.

Photoionization occurs when an electron absorbs a photon (emitted by some source) of sufficient energy to become unbound from an atom or ion. The energy of the photon must be above the ionization potential (IP), which is the minimum energy required to release the electron from the atom or ion. The IP is different for each element and ion, for hydrogen, the most abundant element, the IP is 13.6 eV. For other elements, like oxygen, the IPs (from the ground state) to generate O^+, O^{+2}, and O^{+3} are 13.6 eV, 35.1 eV, and 54.9 eV, respectively.

On the other hand, recombination is the recapture of a free electron by an ion. This process turns a free electron into a bound one, and the difference in energy between the two states is released by the emission of a photon.

If we consider a pure hydrogen gas, the photoionization equilibrium is described by:

$$n(\mathrm{H}^0) \int_{\nu_0}^{\infty} \frac{4\pi J_\nu}{h\nu} a_\nu(\mathrm{H}^0) d\nu = n_e n_p \alpha(\mathrm{H}^0, T) \tag{1.6}$$

where the left side of the equation represents the number of ionizations and the right side the number of recombinations, both per time unit. For the left hand side of the equation: $n(\mathrm{H}^0)$ is the neutral hydrogen density, $a_\nu(\mathrm{H}^0)$ is the H^0 ionization cross section in the ground level ($1^2\mathrm{S}$) for a photon with frequency ν ($a_\nu(\mathrm{H}^0) \approx 6\times10^{-18}$ cm^2), and $\nu_0 \approx 3.3\times10^{15}$ Hz is the minimum frequency corresponding to the IP of H in the ground state. For the right side of the equation: n_e and n_p are the electron and proton densities, respectively, and $\alpha(\mathrm{H}^0, T)$ is the recombination coefficient of hydrogen at the

temperature T (e.g., $\alpha(\mathrm{H}^0, T) \approx 4 \times 10^{-13}$ cm^3 s^{-1}, for $T = 10^4$ K). The equation 1.6 considers the following approximation: all the ionizations of H^0 occur from the ground level and they are balanced with the H^+ recombinations at different energy levels. This approximation is valid because the mean delay between ionizations of H^0 is much larger ($\sim 10^8$ s) than the lifetime of the electron in an excited state of the H atom ($\sim$0.12 s to 10^{-4} s), so the electron in an excited state has time for the transition downwards to the ground state before it can be ionized.

In the recombination process, when the electron recombines directly to the ground level, the photon released has an energy equal or larger than the IP of the recombined ion. This photon can then produce another ionization. Two approximations can be considered for the optical depth of the emission lines of the Lyman series*: an optically thin nebula, called case A, where the photons escape the nebula, and an optically thick nebula, called case B, where the photons are absorbed within the nebula. The recombination coefficient in the case B is denoted by $\alpha_B(\mathrm{H}^0, T)$. Raičević et al. (2014) includes in a radiative transfer scheme the possibility that recombination radiation travels a certain distance instead of being absorbed 'on-the-spot' and compares the results with case B approximations finding that case B is accurate near the ionization front.

The ionic fraction is the ratio of abundance of an ion to the total abundance of the element. The fraction of ionized hydrogen is given by:

$$\chi_{\mathrm{H}^+} = \frac{n(\mathrm{H}^+)}{n(\mathrm{H})} \tag{1.7}$$

where $n(\mathrm{H}^+)$ and $n(\mathrm{H})$ are the ionized and total densities of hydrogen, we do not consider here molecular hydrogen. In most photoionized regions, the hydrogen ionization fraction, χ_{H^+}, is close to unity throughout the gas, that is, the hydrogen is fully ionized, then there is a transition zone and beyond it, the gas is neutral.

For a pure hydrogen nebula with a single ionizing star and a filled sphere gas distribution, the radius of the H^+ sphere is called the Strömgren radius (R_S). This radius can be estimated from:

$$Q(\mathrm{H}^0) = \frac{4\pi}{3} R_S^3 \; n^2(\mathrm{H}) \, \alpha_B(\mathrm{H}^0, T) \tag{1.8}$$

where $Q(\mathrm{H}^0)$ is the rate of ionizing photons produced by the central star. The approximation only considering ionization and recombination of H is an idealized case, but for most of the typical abundances in the ISM, the He, heavier elements, and dust do not have an important effect on the

*Hydrogen spectral series of transitions from higher n levels to the ground state ($n = 1$).

ionization balance. This is not the case for gas with an H-poor content, as it will be shown in the next chapters.

1.1.3 Thermal equilibrium

Another assumption in the treatment of photoionized gas is the balance between the heating and the cooling of the gas, or thermal equilibrium. This assumption, that considers the gas in a stationary state, is valid when the timescales of the variability in the ionizing radiation or the geometry of the nebula are much larger than the timescales of heating and cooling of the gas. The heating can be seen as a gain of energy of an element of volume of a nebula, and the cooling as a loss of energy. The principal source of heating in photoionized gas is photoionization, mainly of H with a small fraction from He and even smaller from heavier elements. In fig. 1.3[†], we plot an illustrative example of energy rates for some heating and cooling processes. The energy gain rate due to H ionization by a 50,000 K blackbody, as a function of the electron temperature, is represented as a blue solid line. It can be seen that the energy gain follows a linear relationship in a loglog diagram, decreasing as the electron temperature rises. Other sources of heating are cosmic rays (Peimbert & Goldsmith 1972; Giammanco & Beckman 2005), shocks (Peimbert et al. 1991), and photoelectric heating by dust grains (Oliveira & Maciel 1986; Draine 1978).

The importance of heavier elements concerns the cooling, since collisionally excited lines (CELs, sec. 1.2.2) produced by heavy elements are the main cooling mechanism. The CELs are mainly emitted by metals (elements heavier than H and He), because the energies of the first excited levels are of a few eV and thus can be excited collisionally. The solid green line in fig. 1.3 shows the cooling rate due to CELs of O^{++}, for $O^{++}/H^{+} = 5{\times}10^{-4}$ and $n_e = 10^2$ cm^{-3}.

The recombination also contributes to the cooling, generating a continuum (sec. 1.3.1) and emission lines (sec. 1.2.1). The dotted green line of fig. 1.3 shows an example of the energy loss by H^{+} recombination as a function of electron temperature and $n_e = 10^2$ cm^{-3}.

Another cooling process is the free-free or Bremsstrahlung radiation (sec. 1.3.3). For interactions between e^{-} and p^{+}, the free-free energy loss is ploted as a green dashed line in fig. 1.3 assuming

[†]The formulas for the energy rates in this plot are based on the Notebook `https://github.com/Morisset/NEBULATOM-tools/blob/master/Notebooks/NC_2_2.ipynb` of the Nebulatom school `https://eventos.redclara.net/event/343/program`.

$n_e = 10^2$ cm^{-3}. From the three cooling mechanisms plotted in fig. 1.3, it can be seen that the CELs of O^{++} are the major contributors to the cooling.

The thermal equilibrium equation is:

$$G = L_R + L_{FF} + L_C \tag{1.9}$$

where G is the heating rate by photoionization, L_R is the recombination cooling rate, L_{FF} is the free-free cooling rate and L_C is the collisionally excited lines cooling rate. In fig. 1.3 the intersection of the energy gain and loss (shown in blue and black lines, respectively) will give the electron temperature at thermal equilibrium. At the particular case represented in fig. 1.3, the intersection occurs at about 8700 K, but other cooling contributors must be considered such as CELs of the rest of the metals and under some conditions H collisional excitation. An example of a more complete calculation of the energy loss rate is shown as green lines in the fig. 1.4. This is done with simple photoionization models (see sec. 2.2) at different electron temperatures[‡] and three metalicities (that are scale factors of the solar abundances): $Z = 0.01$, 1 and 10 plotted in dotted, solid, and dashed green lines, respectively. The energy gain plotted in blue lines, is due to H ionizations and is calculated the same way as for fig. 1.3. For the energy gain three stellar blackbody temperatures are considered: 20 kK, 50 kK, and 300 kK shown in dotted, solid, and dashed blue lines in fig. 1.4, respectively. Each of the nine intersections of the gain and loss of energy in the plot, will represent the equilibrium temperature for the corresponding metallicity and stellar temperature. For $Z = 0.01$ and 1, equilibrium temperature is very similar for the different stellar temperatures, which is close to 10^4 K. This is the reason why the electron temperature is usually close to 10^4 K for a different range of conditions in both PNe and H II regions. For $Z = 10$, the equilibrium temperature is about one order of magnitude smaller (1000 - 3000 K) for the different stellar temperatures. This shows that for a higher metal content the electron temperature will be much smaller.

The dust grains can contribute to the heating and the cooling of the gas. For a simplified model of an H II region presented by Maciel & Pottasch (1982), if the photoelectric heating by dust grains is considered, the electron temperature can increase to 9,000 K from a value of 7,500 K when this effect is not taken into account.

[‡]Based on the examples presented in `https://github.com/Morisset/Cloudy_Summer_School/blob/master/Notebooks/Coronal.ipynb` of the Cloudy Summer School.

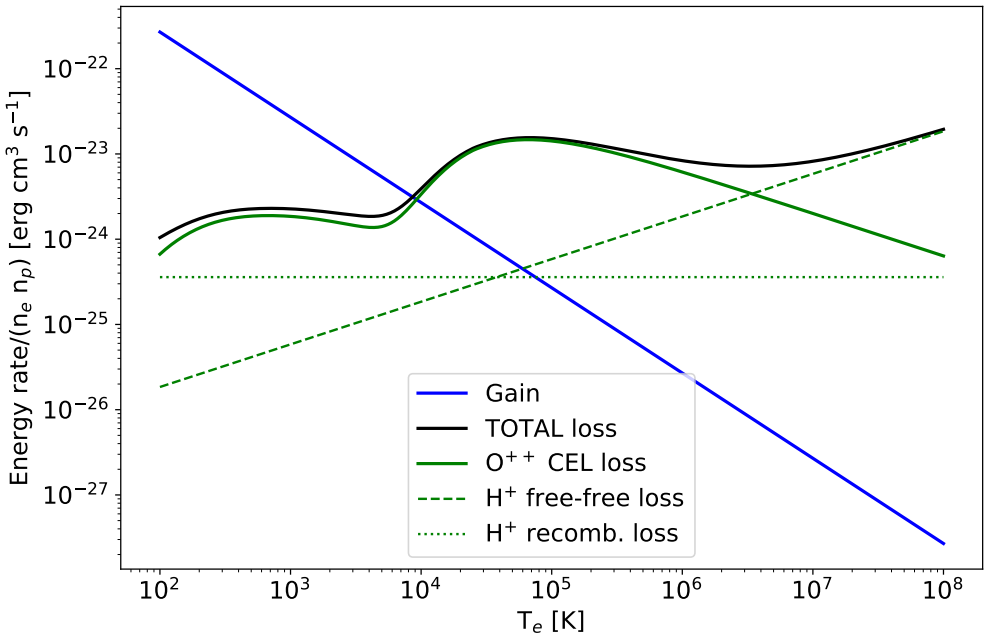

Figure 1.3: The blue line represents the rate of energy gain (due to hydrogen ionization) as a function of electron temperature for a star with 50 kK. The dotted, dashed and solid green lines represent, as a function of electron temperature, the rate of energy loss due to H^+ recombination, free-free emission (e^- and H^+ collision), and CELs from O^{++}, respectively. The black line is the sum of energy losses considered. A ionic abundance of $O^{++}/H^+ = 5{\times}10^{-4}$ and electron density of 10^2 cm^{-3} are assumed.

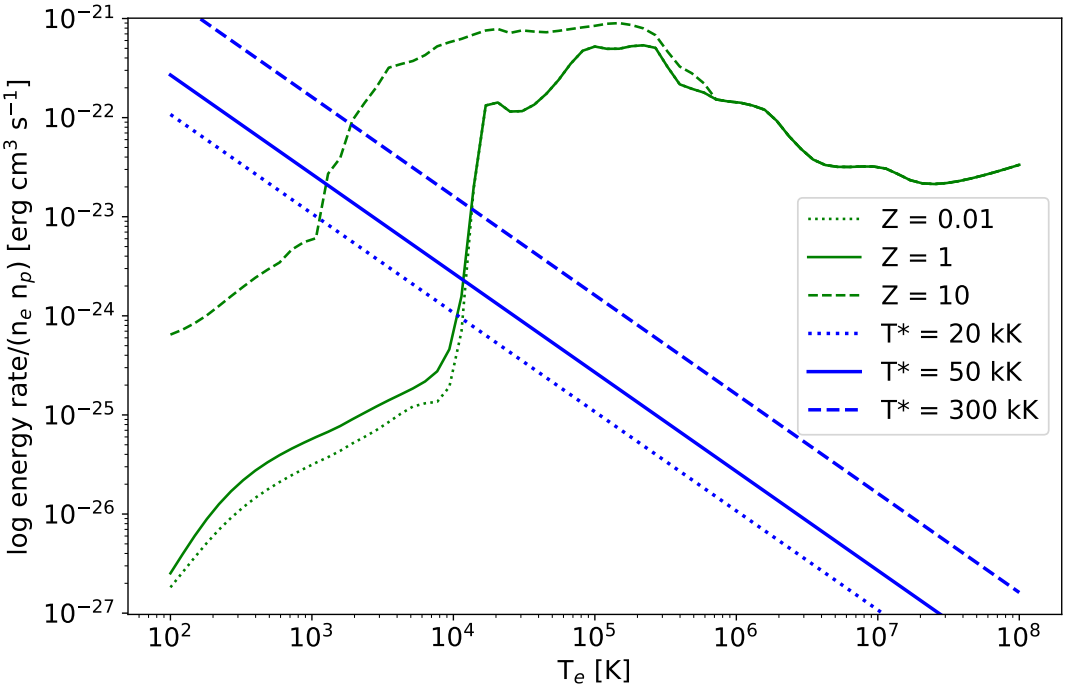

Figure 1.4: All the blue (green) lines represent the rate of energy gain (loss) as a function of electron temperature. Three stellar temperatures (20 kK, 50 kK, and 300 kK) and three metallicities (0.01, 1, and 10) are plotted (dashed, solid, and dotted lines). The energy gain is due to hydrogen ionization and the energy loss rate is estimated with a simple photoionization model with hydrogen density 1 cm^{-3} that considers the cooling from free-free, recombination and colisionally excited lines for all the ions in the gas. Intersections between blue and green lines represent the equilibrium temperature.

1.2 Emission line processes

The emission as a function of wavelength in a photoionized gas has two main components: a continuum and emission lines. If the observation is not highly contaminated by the light of the star (or stars), the continuum in the optical range will be faint and the emission lines will be more prominent. The emission lines are produced by the elements that compose the gas. The principal mechanisms that generate emission lines are described below.

1.2.1 Recombination lines

To generate recombination lines (RLs), it is first necessary for a free electron to be captured by an ion in an energy state higher than the ground level. Then, the electron at this high state cascades downward to lower energy states emitting photons at each downward energy transition. These photons are emitted at signature energies for each element. When a large number of photons are emitted at the same signature energy there is a peak in the emission, thus generating emission lines. Due to the high abundance of hydrogen in diffuse nebulae, the most prominent recombination lines are of H, followed by helium lines, the second most abundant element. Heavy elements also produce emission lines, but since they are less abundant, their recombination lines are fainter (*e.g.*, O II λ 4649.13/Hβ = 0.014, N II λ 5666.6/Hβ = 0.0022, He I λ 4471/Hβ = 0.062, for PN NGC 6153, see Liu et al. 2000).

In the left panel of fig. 1.5, we show the emissivities as a function of electron temperature for Hα, Hβ, He I λ 4471, O II λ 4649.13, and N II λ 5666.63. An electron density of 100 cm^{-3} was adopted for the calculations in the plot.

1.2.2 Collisionally excited lines

Collisionally excited lines (CELs) are generated when a free electron collides with an ion, in the collision a bound electron gains energy and is excited to a higher energy state. It may go back to the ground energy level, emitting photons at each transition.

In the right panel of figure 1.5, the emissivities of some optical and IR CELs produced by O^{++} are plotted as a function of electron temperature, considering an electron density of 100 cm^3. For the

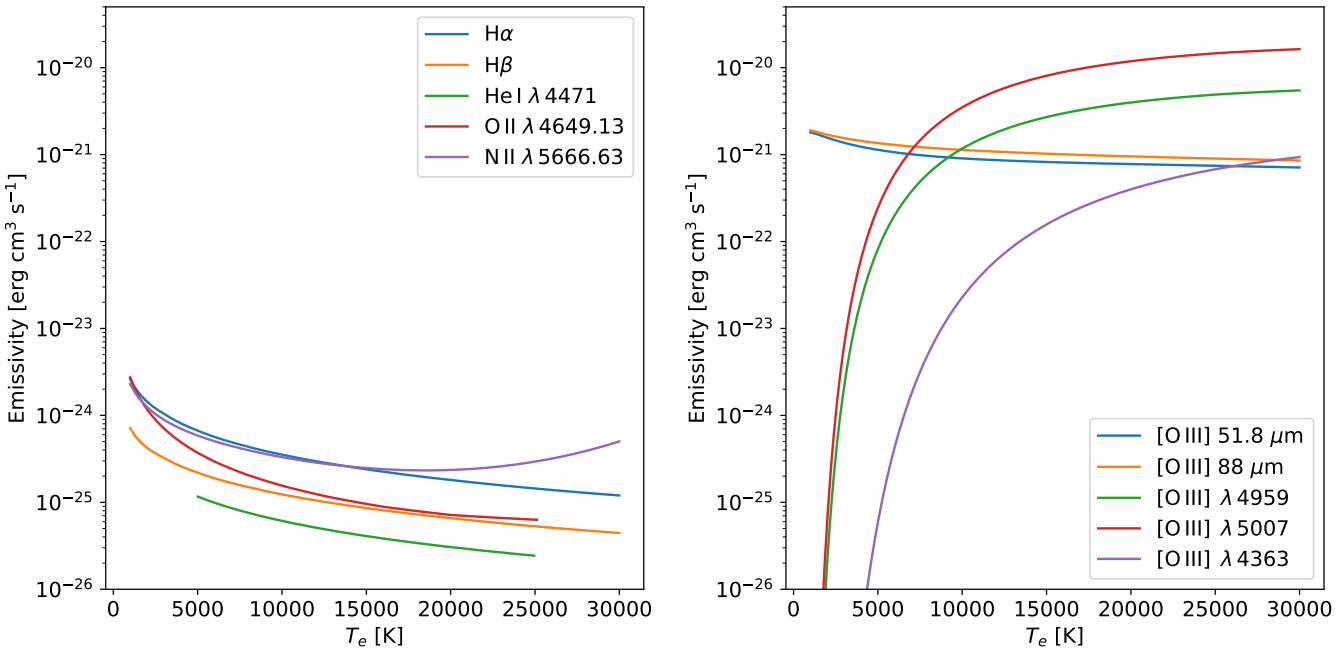

Figure 1.5: Left panel: Emissivities for the RLs produced by H^+, O^{+3} and N^{+3}, as a function of electron temperature. Right panel: Emissivities for the CELs produced by O^{++}, as a function of electron temperature. An electron density of 100 cm^{-3} was used. Figure obtained using PyNeb (Luridiana et al. 2015) with the predefined atomic data `pyneb_20_01` (Morisset et al. 2020).

[O III] λ 4363, λ 4959, and λ 5007 optical lines, a similar behaviour is observed, with an exponential decay at low temperatures. These CELs have an important contribution to the cooling of the gas, as it was shown in fig. 1.3, where their contribution is much larger than for free-free and recombination of H^+. The [O III] λ 51.8 μm and λ 88 μm IR lines show a more constant behaviour with a small increase at low temperatures. This is due to the small energy required to generate these lines, making it possible that they can be produced even at very low temperatures.

1.2.3 Fluorescence

Another process of emission lines is fluorescence, in which an electron of an ion is excited to a higher level through absorption of a photon with sufficient energy. The electron then decays to the ground level, emitting one or more photons corresponding to each intermediate transition. This effect has been described first by Bowen (1934), identifying the boosting of the O III λ 3133, λ 3428, and λ 3444 lines to a fluorescence due to pumping by the He II λ 303.78 far UV line. The pumping may also arise due to the stellar continuum, as described by Escalante et al. (2012), where the fluorescence contribution to C II, N II, and O II lines has been computed for the PN IC 418.

Raman scattering is also another way of producing emission lines, as identified for example in PN NGC 7027 by Pequignot et al. (1997).

1.3 Continuum in gaseous nebulae

As mentioned in the previous section, the continuum and emission lines are the main components of the spectrum in photoionized gas. Emission lines are generated at signature energies because the energy levels of the different elements are quantized. The continuum is generated by processes that allow non-discrete values of energy in a large part of the electromagnetic range. The main continuum processed in gaseous nebula are described in the following subsections.

1.3.1 Free-bound

The kinetic energy distribution of the electrons in the gas is a continuum, so when an electron is recombined by an ion, the energy difference between the free and bound state will depend on

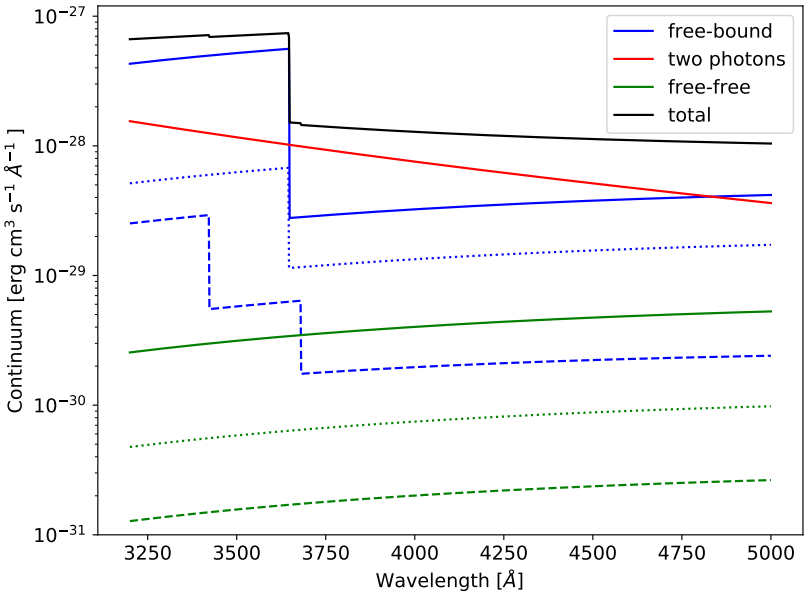

Figure 1.6: Continuum emission as a function of wavelength for free-bound, free-free and two photon emission process. Solid line is for H I, dashed for He I and dotted for He II. The emissions are estimated for: $He^+/H^+ = 0.05$, $He^{++}/H^+ = 0.05$, $T_e = 10^4$ K and $n_e = 100$ cm^{-3}.

the kinetic energy of the free electron and on the energy of the level at which is captured. The difference between these energies is released radiatively. The photons emitted by this process generate a continuum, because the kinetic energy of the free electron is not restricted to quantum values. The main contributor of this emission mechanism is hydrogen, due to its large abundance. The free-bound emission for H^+, He^+, and He^{++} recombination are shown as blue solid, dashed and dotted lines in figure 1.6 as a function of wavelength, with $He^+/H^+ = 0.05$, $He^{++}/H^+ = 0.05$, $T_e = 10^4$ K and $n_e = 100$ cm^{-3}. The plot is generated with PyNeb package v.1.1.13 (Luridiana et al. 2015) using the coefficients presented in Ercolano & Storey (2006). From the figure, it can be seen that the dominant contribution is due to the H^+ recombination. It is also noticeable that with equal ionic abundances of He^+/H^+ and He^{++}/H^+, the He^{++} recombination is more important, so the ionization degree will have an important role in the total free-bound continuum.

1.3.2 Two photons

This emission occurs when an electron goes from the level 2^2S to 1^2S, in a H atom, via an intermediate state between the two levels. The intermediate state can be at any energy between the energies of

the 2^2S and 1^2S levels. In this process two photons are emitted, one at each transition level of the electron. The 2^2S level is populated by recombination of electrons to higher levels and followed by radiative de-excitation transitions until 2^2S level. The energy sum of the two photons equals the energy between the 2^2S and 1^2S levels. Individually, the energy of each photon can have any value in the range of available energy given by the two levels. This less restricted range of energies for each of the two photons is what causes this emission to be a continuum instead of an emission line. Fig. 1.6 shows the continuum emission for the two emission process, the values are obtained for an electronic temperature of 10^4 K and electronic density of 100 cm^{-3}, using the `Continuum class` of the python package PyNeb (Luridiana et al. 2015, see sec. 2.1). When the electronic density is very low, the only process that depopulates the 2^2S level is the two photons decay. For higher densities, collisions with electrons or protons that change the angular momentum from 2^2S to 2^2P^0 need to be considered. For proton densities $\geq 10^4$ cm^{-3}, the colisional de-excitation to 2^2P^0 dominates over two photon decay in depopulating the 2^2S level.

1.3.3 Free-free

The Coulomb collision of charged particles can produce radiation. Since the collisions between two electrons or two ions generate electric fields that approach zero at large distances, only collisions between free electrons and ions are important. The Coulomb force has the same magnitude for the ion and the electron, but the acceleration of electrons is larger due to their smaller mass compared to the ions. The only radiation considered is the one due to the acceleration of electrons. The change in the velocity of the electron is released by the emission of a photon equal to the loss in kinetic energy. The electrons remain free after the collision, hence the free-free name for the emission. The collision of the free electron can be with H^+, He^+, He^{++} or metals. Due to the large abundance of H, followed by He, the ions of these elements are the major contributors to the free-free emission. In solid, dashed and dotted green lines of fig. 1.6 are shown the free-free continuum emission of electron collisions with H^+, He^+, He^{++} for the wavelength range 3200 to 5000 Å, and assuming: $He^+/H^+ = 0.05$, $He^{++}/H^+ = 0.05$, $T_e = 10^4$ K and $n_e = 100$ cm^{-3}. From the figure, it can be seen that the free-free emission is not an important contributor to the continuum for the plotted wavelength range, and that the collisions with H^+ are dominant followed by He^{++}, so the ionization stage of He is important. Free-free emission becomes important at radio wavelengths.

1.3.4 Dust grains

The dust grains can have an effect in the continuum emission of the nebula by two means:

- Scattering the light from the star (or stars) and redirecting it into the line of sight (more important in H II regions).
- Absorbing the UV and optical stellar light and then re-emitting it as thermal and non-thermal continuum emission at IR wavelengths (Draine 2003).

1.4 Different processes that contribute to emission lines

An emission line is produced when an electron falls downwards from an excited level (n_{high}) to a lower energy level (n_{low}).

The n_{high} level can be populated by different processes, such as:

- Radiative recombination: an electron is captured by an ion at an excited energy state, and a photon is released with energy given by the difference between the kinetic energy of the electron ($m_e v^2/2$) before it is captured and the binding energy of the level ($E_b = h(\nu_0 - \nu)$) at which it is captured.

  $$e^- + \mathrm{X}^{i+1} \rightarrow \mathrm{X}^{i*} + h\nu'$$

  where $h\nu' = \frac{1}{2} m_e v^2 + h(\nu_0 - \nu)$, the ν' photons generate the free-bound continuum (see sec. 1.3.1).

- Collisional excitation: the collision of a free electron with an ion transfers some of the energy of the free electron to an electron bound to the ion, sending it to the n_{high} level.

  $$e^- + \mathrm{X}^{i} \rightarrow e^- + \mathrm{X}^{i*}$$

- Fluorescence: a photon of a specific energy is absorbed by an ion and an electron of the ion jumps to an energy state with approximately the same energy of the photon absorbed.

  $$h\nu + \mathrm{X}^{i} \rightarrow \mathrm{X}^{i*}$$

- Dielectronic recombination: an electron is captured by an ion at an excited state, the energy released in the capture process is absorbed by another electron of the ion, exciting this second electron to a higher energy state corresponding to this energy.

$$e^- + \mathrm{X}^{i+1} \rightarrow \mathrm{X}^{i**}$$

- Charge exchange: a collision process of an ion with another ion, atom or molecule, where the latter transfers one (or more) electron(s) to the ion, with the electron(s) arriving at an excited state.

$$\mathrm{Y}^{j} + \mathrm{X}^{i+1} \rightarrow \mathrm{Y}^{j+1} + \mathrm{X}^{i*}$$

  In all the cases, * denotes that the ion has an electron at an excited state ($n_{high} > 1$) and ** denotes that the ion has two electrons at a excited states.

Once the n_{high} level is populated, the radiative transition to a lower energy level (that produces the emission line) can be:

- Permitted: when they follow the selection rules[§]. These transitions are denoted by the element, ionization sate, and the wavelength of the transition, e.g., O II λ 4649.13.

- Semi-forbidden: they follow the selection rules, except $\Delta S \neq 0$. These transitions are denoted by the element, ionization sate, one square bracket (']') and the wavelength of the transition, e.g., C III] λ 1908.7.

- Forbidden: they follow the selection rules, except $\Delta l \neq \pm 1$, $\Delta S \neq 0$, or $\Delta L \neq 0, \pm 1$. These transitions are denoted by two square brackets ('[ ]') between the element and ionization state, followed by the wavelength of the transition, e.g., [O III] λ 5007.

A given emission line, whatever it is permitted, semi-forbidden or forbidden, can result from the population of an excited level by several processes (recombination, collisional excitation or fluorescence), each one contributing to the total line intensity. The recombination lines affected by fluorescence effects are not usually used to estimate physical and chemical parameters, due to the complex estimation of the contribution of this process to their intensity (See nevertheless Escalante et al. 2012).

For heavy elements, the energy difference between the ground level and the first excited levels are a few eV, comparable to the energies of free electrons in the gas at typical nebular temperatures,

[§] $\Delta J = 0, \pm 1$, $\Delta M_J = 0, \pm 1$, parity change, $\Delta S = 0$, $\Delta l = \pm 1$, $\Delta L = 0, \pm 1$

so collisions with free electrons are able to excite the bound electrons to these levels. Most of the transitions issuing from these excited levels are violating the selection rule, leading to forbidden lines. For hydrogen, the first excited level is at 10.2 eV, making it difficult to be excited by collision with free electrons at the usual nebular temperatures of $\sim 10^4$ K.

Chapter 2

Some computational tools for studying photoionized gas

In this chapter we present the software tools that we use to study the photoionized gas from a theoretical point of view. We give a brief description of the operation and the physical bases for the tools we use. As mentioned at the end of the chapter, the approach we use is based on stationary photoionization modelling of nebulae, and is one of the possible methods to study nebulae.

2.1 PyNeb

PyNeb is a python package developed by V. Luridiana, C. Morisset and R. Shaw (Luridiana et al. 2015; Morisset et al. 2020) to analyse emission lines in gaseous nebulae. Comparing observed or theoretical emission line ratios, PyNeb can be used to determine physical conditions (i.e. electron temperature and density), ionic and total abundances. Corrections for dust extinction can be made with the code for several extinction laws both for PNe and H II regions. Several options are also available for ionization correction factors (ICFs), to correct for the unobserved ions when determining total abundances. This is the so-called direct method to determine chemical abundances. It is also possible to use a Monte Carlo method*, by adding small variations to the input data (the amplitude of variations is based on the data uncertainties) and generate a distribution of values instead of a

*`addMonteCarloObs` of the `Observation` class

single value for each determined parameter. The code can be parallelized so the computational time is reduced when the Monte Carlo option is included.

The code is public, documented and regularly updated[†]. Since its publication new options have been added to the code, as for determining chemical abundances with recombination lines of metals, or to estimate the electronic temperature associated with the Paschen or Balmer jump of H I.

2.1.1 Emissivities

The equations and theory from this and the following subsections are taken from Pequignot et al. (1991), Osterbrock & Ferland (2006), Luridiana et al. (2015) and Morisset et al. (2020).

The emissivites of CELs and RLs can be obtained with PyNeb as a function of electron temperature and density. Some examples are shown in fig. 1.5 for RLs of H^+, He^+, O^{++}, and N^{++}, and CELs of O^{++}, in the left and rigth panels, respectively. From the figure we can see that the emissivities of CELs have a stronger dependence on temperature than RLs.

The atomic data for CELs and RLs is available for 20 and 5 elements, respectively, in different ionic stages, and many more if the `Chianti`[‡] atomic data base is used (Dere et al. 1997, 2019).

For recombination lines, the emissivity for the transition with wavelength λ, can be defined as:

$$\epsilon_\lambda = n_e \, n_{i+1} \, \alpha_\lambda \, E_\lambda \quad [\mathrm{erg \cdot cm^{-3} \cdot s^{-1}}] \tag{2.1}$$

where n_e and n_{i+1} are the electron and recombining ion densities (units $\mathrm{cm^{-3}}$), α_λ is the effective recombination coefficient (units $\mathrm{cm^3\ s^{-1}}$), and E_λ is the energy of the transition with wavelength λ (units erg).

The effective recombination coefficient of the transition from j to i (with associated wavelength λ), is the product of:

- α_j, the recombination coefficient to the level j (units $\mathrm{cm^3\ s^{-1}}$), including direct recombinations and downward radiative transitions.
- $Br(\lambda)$, the Branching ratio, which is the ratio of the decay probability for the transition from the levels j to i (with wavelength λ) to the total decay probability coming from the level j.

[†] `https://github.com/Morisset/PyNeb_devel`

[‡] `https://www.chiantidatabase.org/`

For RLs the emissivities are obtained in terms of the effective recombination coefficient by interpolating from tables (or defined as a function) for a range of electron temperatures and densities. There can be more than one reference of the atomic dataset available for a single ion, so the user can choose the one they wish to use, although PyNeb has a default dataset (see Morisset et al. 2020, for more details on the atomic data used in PyNeb.). The recombination coefficients from Pequignot et al. (1991) are available for the ions: H^+, He^+, He^{++}, C^+, C^{++}, C^{+3}, C^{+4}, N^+, N^{+2}, N^{+3}, N^{+4}, N^{+5}, O^+, O^{+2}, O^{+3}, O^{+4}, O^{+5}, O^{+6}. Other available data are: Storey & Hummer (1995) for H^+ and He^{++}, Palay et al. (2012) for He^+, Fang et al. (2011) for N^{+2}, Kisielius et al. (1998) for Ne^{+2}, Storey et al. (2017) for O^{+2}, Davey et al. (2000) for C^{+2}, Smits (1996) for He^+, and Storey (1994) for O^{+2}.

The emissivity for CELs, the transition from level j to i, is defined as:

$$\epsilon_{ji} = n_j \, A_{ji} \, h\nu_{ji} \quad [\mathrm{erg \cdot cm^{-3} \cdot s^{-1}}] \tag{2.2}$$

where n_j is the density of the ions with an electron in the level j (units $\mathrm{cm^{-3}}$), A_{ji} is the transition probability for going from the level j to the level i (units $\mathrm{s^{-1}}$), and $h\nu_{ji}$ is the energy difference between the j and i levels (units erg).

The emissivity of a CEL is estimated solving for n_j the $n+1$ coupled equations of the level population balance (eq. 2.3 and 2.4) in an n-level atom. Usually 5 or 6 levels are considered, which is a good approximation since the energy to excite higher levels is larger than the average energy of the thermalized electrons.

For the level j, the level population balance equation is (neglecting other processes like fluorescence or recombination in the populating of the levels):

$$\sum_{j \neq i} n_e n_j q_{ji} + \sum_{j>i} n_j A_{ji} = \sum_{j \neq i} n_e n_i q_{ij} + \sum_{j<i} n_i A_{ij} \quad (i = 1, ..., n_{max}) \tag{2.3}$$

where n_e is the electron density (units $\mathrm{cm^{-3}}$), n_i is the density of the ions with an electron in the level i (units $\mathrm{cm^{-3}}$), and q_{ij} (q_{ji}) for $j > i$, is the rate for collisional excitation (de-excitation) with units $\mathrm{cm^3\,s^{-1}}$. The left (right) side of the equation is for the de-population (population) of the level j.

The total ion density, n_{total}, for a n-level atom is considered as follows:

$$n_{total} = \sum_{i=1}^{n} n_i \tag{2.4}$$

PyNeb gives the emissivity per ionic and electron density: $\epsilon_{ji}/(n_e n_{ion})$ with units erg$\cdot$ cm$^3\cdot$ s^{-1}, both for RLs and CELs. Where n_{ion} is the total ion density, represented by n_{i+1} for RLs (eq. 2.1) and n_{total} for CELs (eq. 2.4).

The atomic data (i.e., collision strengths and transition probabilities) is one of the sources of uncertainties in the physical and chemical parameter determination (Juan de Dios & Rodríguez 2017; Rodríguez 2020). Recently, an assesment of the atomic data was made with PyNeb (Morisset et al. 2020), exploring the different available atomic data for: O II, Ne IV, S II, Cl III, and Ar IV and selecting the default atomic datasets.

2.1.2 Continuum

PyNeb can be used to estimate the continuum for a wavelength range, as a function of electron temperature and density, and ionic abundances of He^+/H^+ and He^{++}/H^+. The continuum considers the following processes:

- Free-bound emission for recombination of H^+, He^+, and He^{++} (see sec. 1.3.1). Computations estimated following Ercolano (2006).
- Two photon decay (see sec. 1.3.2) of H I, estimated based on Osterbrock & Ferland (2006).
- Free-free emission for electron collisions with H^+, He^+, and He^{++} (see sec. 1.3.3). It is based on Storey & Hummer (1991).

The continuum obtained has units of erg cm^3 s^{-1} Å^{-1}. An example of the estimation including all the mentioned continuum emission processes is show in fig. 1.6.

2.1.3 Electron temperature and density

The electron temperature and density can be obtained with PyNeb from the intensities of sensitive line ratios. There are several line ratios that can be used as either density or temperature diagnostics. Some examples for density sensitive line ratios are: [S II] λ 6731/λ 6716, [O II] λ 3727/λ 3729, [Cl III] λ 5538/λ 5518, and [Ar IV] λ 4740/λ 4711. These density diagnostics are for transitions with very similar energies so they don't have a strong dependence with the temperature, they arise from different levels but fall to the same level (the ground level for the transitions previously mentioned).

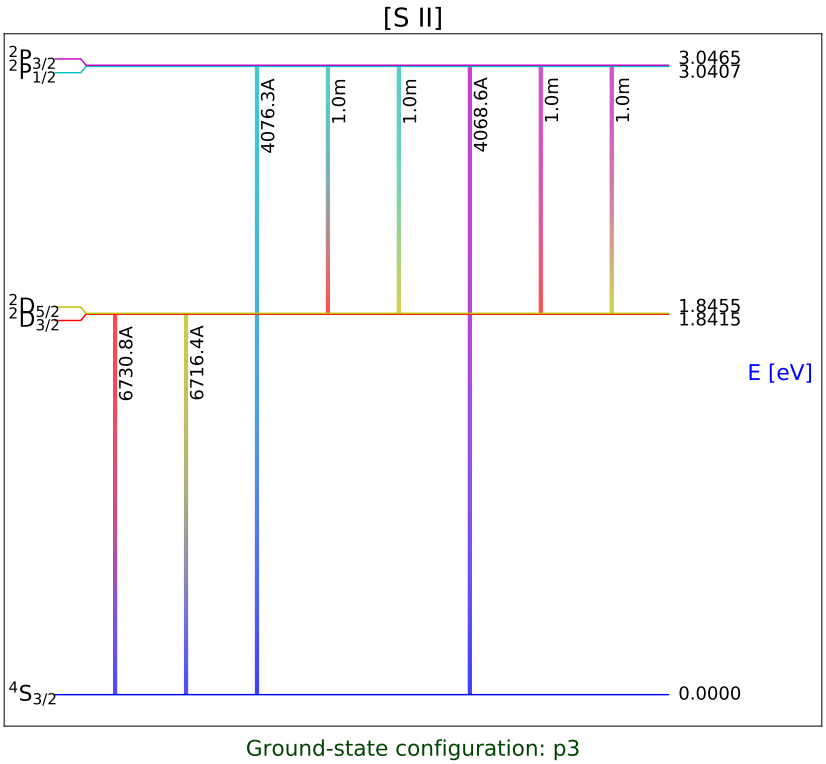

Figure 2.1: Diagram of the first 5 energy level of S^+, the level transitions corresponding to the CELs are marked in different colors. In the labels for the transitions wavelengths, 'A' stands for Å, and 'm' for μm. Figure generated with PyNeb.

To exemplify this, the first 5 energy levels of the S^+ ion are shown in fig. 2.1. The level transitions that correspond to [S II] CELs are marked in different colors. For S^+, the emission lines [S II] $\lambda\,6731, \lambda\,6716$ are generated by electron transitions from level ^{2}D to ^{4}S, and are called nebular lines. While the emission lines [S II] $\lambda\,4076, \lambda\,4069$ arise from transitions from ^{2}P to ^{4}S, and are called trans-auroral lines. To see the dependence on the electron temperature and density, we plot in fig. 2.2 the [S II] $\lambda\,6731/\lambda\,6716$ emissivity grid for densities ranging from 10 to 10^8 cm^{-3} and temperatures from 5,000 and 20,000 K. We can see that in the density range from $10^{1.8}$ to $10^{4.6}$ cm^{-3}, with the S^+ line ratio the density can be derived if the temperature is known.

Some widely-used temperature diagnostics are: [O III] $\lambda\,4363/\lambda\,5007$ and [N II] $\lambda\,5755/\lambda\,6584$. These temperature diagnostics are the ratio of an auroral[§] to nebular[¶] line, the dominant dependence of these line ratios is on the electron temperature (T_e), and only at densities close to the critical

[§]Forbidden transitions from ^{1}S to ^{1}D.
[¶]Forbidden transition from ^{1}D to ^{3}P.

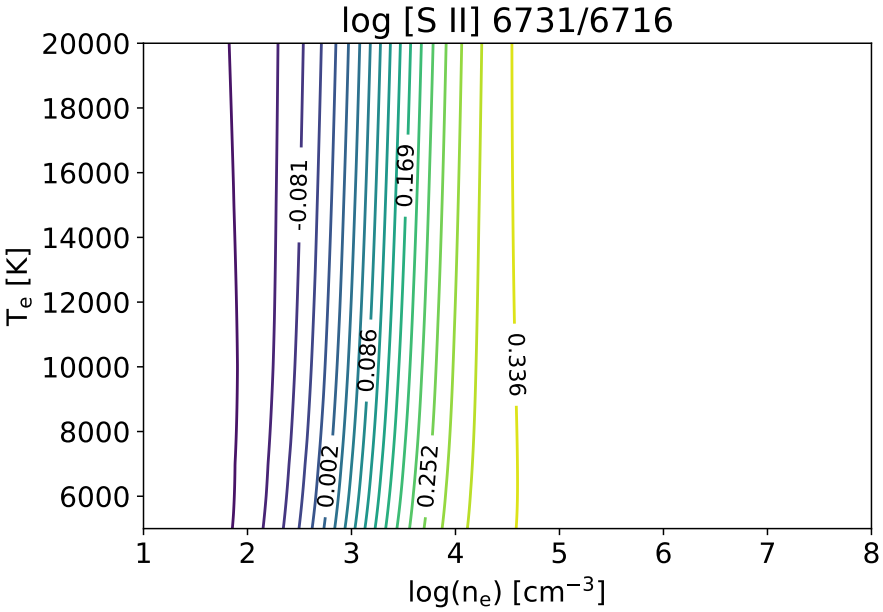

Figure 2.2: Emissivity grid of log([S II] λ 6731/λ 6716) for electron temperature and density ranging from 5,000 to 20,000 K and 10 to 10^8 cm^{-3} respectively, computed with PyNeb. The regions of high density ($> 10^5$ cm^{-3}) have a constant emissivity ratio, independently of the density.

density[‖] is the line ratio no longer a temperature diagnostic. In fig. 2.3, we plot the emissivity grid of [O III] λ 4363/λ 5007, for a range of T_e from 5,000 to 20,000 K for densities ranging from 10 to 10^8 cm^{-3}. We notice that for densities lower than 10^5 cm^{-3}, the O^{++} line ratio is a good temperature diagnostic.

To get the electron temperature, PyNeb (with the `getTemDen` method) requires the observed intensity ratio, the diagnostic to be used, and the electron density. The temperature estimation is made computing the emissivity ratio of the selected diagnostic for a range of temperatures and the density given. The match between the computed emissivity ratio and the observed intensity ratio will determine the temperature. An example for the [O III] λ 4363/λ 5007 temperature diagnostic is shown in fig 2.4, with an intensity ratio of 0.01 and $n_e = 10^2$ cm^{-3}. The estimated temperature is about 11,500 K.

Each temperature or density diagnostic has a validity range, outside of which the code will return

[‖]The critical density is the density at which the collisional desexcitation and the radiative desexcitation of a given level have the same rates.

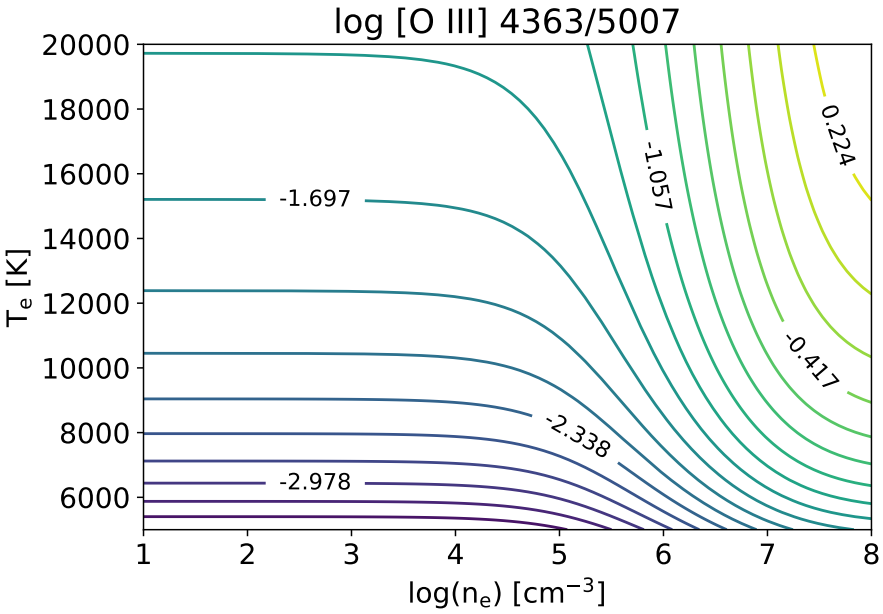

Figure 2.3: Emissivity grid of log([O III] $\lambda\,4363/\lambda\,5007$) for electron temperature and density ranging from 5,000 to 20,000 K and 10 to 10^8 cm^{-3} respectively, computed with PyNeb.

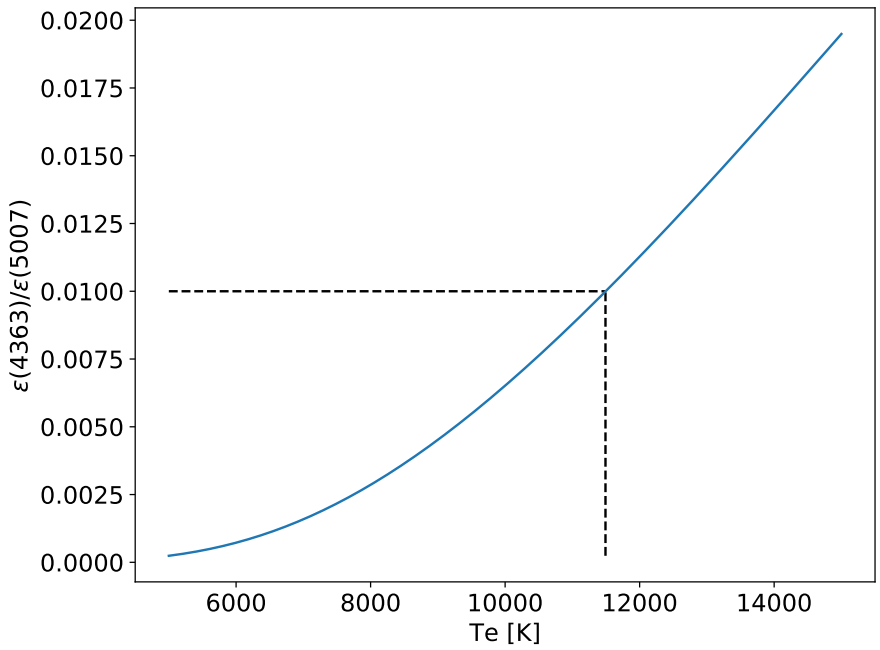

Figure 2.4: Blue solid line: emissivities ratio of [O III] $\lambda\,4363/\lambda\,5007$, determined with PyNeb for $n_e = 10^2$ cm^{-3}. Horizontal dashed black line corresponds to a value of 0.01 of the emissivities ratio. Vertical dashed black line is the electron temperature at the intersection value (about 11500 K).

NaN[**]. The analogous process is made to estimate the density. If the temperature is known, the density can be estimated from a sensitive line ratio and vice versa. It is also possible to simultaneously estimate the temperature and the density with a temperature and density sensitive line ratio[††].

There is also an option to combine several temperature and density diagnostics in the same plot, and for each intersection, a temperature and density are simultaneously estimated. The errors in the line intensities can be taken into account here.

2.1.4 Ionic and total abundances

Ionic abundances can be obtained once the electron temperature and density are known. The abundances are obtained relative to hydrogen. For a given ion, X^{+i}, the ionic abundance is estimated from:

$$\frac{n(X^{+i})}{n(H^{+})} = \frac{I(\lambda)}{I(H\beta)} \frac{\epsilon(H\beta)}{\epsilon(\lambda)} \tag{2.5}$$

where $I(\lambda)$ is the line intensity for a transition with wavelength λ emitted by the X^{+i} ion.

To get the total abundance of an element, all the ionic abundances for that element are required (see eq. 2.6). It is not always possible to compute all of them, so a correction is made to consider the ions with unknown abundance. This correction is called ionization correction factor (ICF) and is based on the proximity of the IP between ions of known and unknown abundance (like for N^+ and O^+, see Peimbert & Costero 1969) or photoionization models (Kingsburgh & Barlow 1994; Delgado-Inglada et al. 2014b). PyNeb contains a library of ICF[‡‡] for different elements from the literature which can be applied to different objects like PNe or H II regions.

When all the ionic abundances of the element are known, the total abundance is given by:

$$\frac{n(X)}{n(H)} = \sum_i \frac{n(X^i)}{n(H^+)} \tag{2.6}$$

Otherwise it is necessary to apply an ICF, and the total abundance is given by:

$$\frac{n(X)}{n(H)} = \sum_{\bar{i}} \frac{n(X^{\bar{i}})}{n(H^+)} \times ICF \tag{2.7}$$

where $\bar{i}$ is only for the ions with known abundance.

[**]stands for *not a number*, represents any value that is undefined.

[††]The method used to do this is called `getCrossTemDen`

[‡‡]`all_icfs` method of the `ICF` class

2.2 Photoionization models

The physical conditions of photoionized gas can be simulated with codes that compute the radiation transfer, and the thermal and photoionization equilibrium (sec. 1.1.2 and 1.1.3). Some examples of such codes are CLOUDY (Ferland et al. 1998, 2013, 2017), MAPPINGS (Sutherland & Dopita 1993, 2017), MOCASSIN (Ercolano et al. 2003a), and others (Wood et al. 2004). These codes are helpful for studying the physical conditions in plasma in a wide range of conditions from active galactic nuclei (AGN) to the solar corona. All the models presented in this work are built under the assumption of static photoionization equilibrium.[§§] In the work reported here, we use CLOUDY, described in more detail in what follows.

2.2.1 CLOUDY

CLOUDY is a free access code for modelling plasma in non-local thermodynamic equilibrium (NLTE). It was originaly developed to model the gas near a black hole and its accretion disk, such gas is called broad line region (BLR) in the AGN unified model. CLOUDY is updated constantly to improve and solve problems in the code, with a new version released every few years. For this work the version C17.02 was used (Ferland et al. 2017). The code allows to model gas from fully ionized to molecular gas for densities that go from the low density limit to 10^{15} cm^{-3} and temperatures from the cosmic microwave background (CMB) to 10^{10} K. It can be applicable to the interstellar and intergalactic medium, to the coronal gas of a star. The code includes all the ions of the 30 lightest elements and considers 625 species. A species can be an atom, ion or molecule (CO, H_2, H^+, O^{++}).

CLOUDY models the ionization, the thermal and chemical states of the matter. This is done by solving the ionization balance (sec. 1.1.2), the thermal balance (sec. 1.1.3), the level populations (eq. 2.3) and the radiative transfer (sec. 1.1.1) simultaneously for each concentric cell in a spherical symmetric simulation. A radiation or other heating source must be included in the simulation, and the code will predict observables like the emission and absorption spectrum.

For each atom in the simulation the number of levels is predefined but can be modified. Increasing

[§§]The timescale for the recombination of the gas can be approximated by $(n_e \cdot \alpha_A)^{-1}$s, which is close to $10^5/n_e$ yrs. In the case studied here, the density is of order of 10^3cm^{-3}, leading to a typical timescale of a century, smaller than any expected change in the stellar luminosity or shape of the nebula.

(decreasing) the number of levels will improve (worsen) the accuracy of the calculations but make the computation time longer (shorter). It is assumed that the populations of the levels for the different species are mainly in the ground level.

To model a photoionized region, like a planetary nebula (PN) or H II region, CLOUDY requires (among other inputs not used in this work):

- The source of ionization (single star, cluster of stars), including the shape (e.g. a Blackbody at T_{eff}, a stellar atmosphere model) and the hardness (e.g. luminosity) of the spectral energy distribution (SED).
- The hydrogen density distribution. The models are spherical 1D, so the density can only change as a function of the radius in a single model.
- The chemical abundances of the gas. When they are not specified a set of default abundances is used.
- The stopping criteria. If left undefined, the simulation will stop at any temperature below 4,000 K.
- Morphology of the gas, which can be spherical or plane parallel.

When solving for the radiation transfer, and the ionization and thermal balance, the code calculates among others:

- Electron temperature
- Electron density
- Ionic fractions
- Line emission

for each cell in the computation.

2.2.2 PyCloudy

PYCLOUDY[¶¶] (Morisset 2013) is a python library that manages CLOUDY input and output files. It

[¶¶] https://sites.google.com/site/pycloudy/home

allows to write input files for CLOUDY in an easy way with a python script, being able to generate grids of models by adding a few lines of code. PyCLOUDY can read the CLOUDY output files and manage the results in vectorized arrays of data. The CLOUDY models can be run directly from python and be parallelized using PyCLOUDY.

PyCLOUDY allows the computation of pseudo-3D models. This is done by running several 1D models changing some parameters as a function of the polar and azimuthal angles. The models are later combined and interpolated. The line profile, position-velocity diagrams and emission line images can be obtained. The 3D emission cubes can be summed over one axis to obtain the projected 2D image. Observation through a slit can be simulated by applying a mask on the resulting 2D image. This type of modeling is valid when non-radial radiation is not dominant. The advantage with pseudo-3D models is the much shorter computation times as it is computed in only a few minutes, compared to hours for computing a full 3D model.

Gesicki et al. (2016) generate pseudo-3D axisymetric models (using PyCLOUDY) for 6 bipolar and 2 proposed post-bipolar PNe. They successfully reproduce the Hα image observed with HST and the emission line profiles for Hα, [O III] λ 5007 and [N II] λ 6583 observed with VLT/UVES spectrograph. The models help to constrain the ionized mass (0.02-0.1$M_{\odot}$) and the age of the bipolar PNe (1300 - 2000 yr), which are important results in the study of bipolar PNe.

2.3 Computational approach to complex objects

In real astronomical objects, some degree of complexity is almost always observed. This breaks the simple spherical symmetry obtained with a 1D radial description of the object properties. Photoionization models need, before to be computed, that some parameters are defined, like the stellar SED shape, its intensity, the distance of the ionized plasma from the ionizing source, the gas density, as well as its composition, in terms of chemical elements and dust, and its geometrical or optical thickness. Each of these parameters can take a single value or a single radial distribution, leading to a spherical symmetric model. But when the object is obviously complex (as seen from from imaging for example) or when some important observed properties can not be reproduced by a simple 1D model, some parameter(s) can take different values depending on the direction considered from the central ionizing source, leading to distinct 1D models, which are then combined to obtain a complex

multi-phase model. The exact geometrical description of the different components in the object is not always needed, most of the time a weighted sum of the components is enough. Nevertheless, when imaging needs to be reproduced, a 3D model can be generated by combining and interpolating between different 1D models in a 3D grid, or by using a full 3D approach.

In the following lines some examples from the literature are presented, where the complexity of the observed objects can not be reproduced with simple models of one component and where the authors use a multiple component modeling approach.

Morisset & Pequignot (1996) show that a one component spherically symmetric photoionization model, computed with the code `NEBU`, can not simultaneously reproduce the He II λ 4686 and [N II] λ 5755 lines observed in the Nova GQ Mus for a period of 6 years (1984-1990). The high intensity of He II λ 4686 (at day 822 of the observation period) requires a matter-bounded nebula while the observed [N II] λ 5755 is consistent with a radiation-bounded nebula (for the same observation date). A homogeneous opacity model is not suited for the observed emission lines. They found that the emission lines are reproduced in the observed time period with a two component model that has the same abundances and radiation field but different density distribution, column density, and covering factor (fraction of solid angle) for each component.

In the work by Morisset et al. (2002) a two density component photoionization model is used to reproduce simultaneously [O III] λ 51.8 μm/λ 88.3 μm and 6 cm radio flux densities observed for the ultracompact H II region G29.96-0.02. This two density model reproduces most of the radio and IR observations of the H II region. The two components were computed in two independent models and then combined linearly. The diffuse radiation between the two components was not considered, which can be a good approximation only when the opacity is not too high. They assume a total covering factor of 1 between the two components, so no photons escape the region. In their model, the required densities to reproduce the observations, namely [O III] λ 51.8 μm/λ 88.3 μm and 6 cm radio flux densities, were 2 orders of magnitude different (600 cm^{-3} and 50,000 cm^{-3}). This work is an example of the usefulness of considering multi-component models when simple spherical models are not suitable for the complexity of the observed objects.

Aside from observations showing that most PNe are not round (Parker et al. 2006), they also show small-scale structures, like knots with higher opacity than the rest of the gas. If these knots are optically thick (at wavelengths $\leq$ 912 Å), they will shadow nebular zones located in the same direction

but at larger distances from the central star. However, the diffuse radiation from the surrounding gas can ionize this shadowed zone. A 1D model with spherical symmetry is not suitable for modeling the ionization in the shadowed zone, so in the work presented by Morisset & Ercolano (2004), they use the 3D photoionization code MOCASSIN (Ercolano et al. 2003a) to model a cubic shape knot and its shadow (which they call tail). The knot has a density of 10^5 cm^{-3}, the tail of 1.6×10^2 cm^{-3}, and the surrounding gas of 10^2 cm^{-3}. The density in the tail is a bit higher than in the surroundings to maintain pressure equilibrium. The ionization source is a black body at 120 kK and the radiation illuminates the knot and surrounding gas in a plane parallel approximation. The results found in the model (which they mention to be preliminary) are: an enhanced emission of the recombination lines in the shadowed zone due to the lower temperature of the gas, a lower ionization structure in the shadow region, that results in a larger (smaller) emission of the lower (higher) ionization ions for the shadow. The emission lines compared to the surroundings have the following behaviour: Hβ emission line increases about a factor two in the tail, the [N II] λ 6584 decreases in the knot and increases a factor $\sim$ 2.5 in the tail, [O III] λ 5007 decreases more than one order of magnitude in the tail. The work by Morisset & Ercolano (2004) shows that there are significant changes in the emission when a shadow is present, and a non-spherical approach needs to be used to model this knots and its shadow, like in this case a 3D modelling code.

A more recent example is shown in Ramambason et al. (2020). They use the grid of photoionization models from the project BOND (Vale Asari et al. 2016) (for giant H II regions) of the 3MdB*** database (Morisset et al. 2015). With one and two component photoionization models from the grid they try to fit the observed emission lines in z$\sim$0.3-0.4 galaxies with Lyman continuum (LyC) leaking. To simultaneously reproduce the emission lines of ions with different ionization degrees (O^0, S^+, O^+, N^+, and O^{++}) they use a combination of two models with high and low ionization parameter (log U). They consider two scenarios: the model with low log U is density-bounded (scenario 1), and the model with high log U is density-bounded (scenario 2). With the two component models, Ramambason et al. (2020) can reproduce the low ionization [O I] λ 6300 and [S II] λ 6716, λ 6731 emission lines, which is not possible with one component models. They found that the scenario 1 works better for low fraction of escaping LyC (less than 10%) and scenario 2 is better for higher fraction of escaping LyC. This is another good example that shows that a combination of two models is an appropriate method for explaining the complexity of the observed objects to a good extent.

***https://sites.google.com/site/mexicanmillionmodels/

The mentioned works show that a one component model is too simplified to reproduce the observed behaviour in different types of photoionized objects (Novae, H II regions, and giant H II regions), and a combination of two opacities, densities or ionization parameters is necessary to better model such objects. The main focus of the present work continues in that direction, to investigate how multiple-component models can be used to constrain the parameters in otherwise puzzling objects. A full 3D model could also be a good way to reproduce complex objects, but given the large computational times required, the parameter space can not be explored as broadly.

It is worth noticing that it is not always necessary to build a complex (pseudo) 3D model to fit observations of a complex object. In the case multiple phases are suspected to be present, but no spatial information is available to compare with, the exact geometrical distribution of the different regions is not constrained. The complex model can then be obtained by simply summing up the contribution of the different components, without each component being actually associated to a position in the space. The only important and mandatory parameter is the weight of each component in the sum. This is what we call topological equivalent models: one that describe the exact morphology of the object, as would be obtained by a full 3D model, and one that simply sum up the contribution of each component, in the same proportions as the full model. The two models will predict the same integrated line ratios. The first model requires a 3D or pseudo-3D model, the second only needs a few runs of 1D models.

The stationary photoionization modelling approach we use in this work it is one of the ways of studying nebula and it is worth mentioning here that other alternative and complementary approaches can be used to study nebulae from a theoretical point of view: see the works on PNe published by the Schönberner's group from Perinotto et al. (2004) to Schönberner et al. (2010) and the development of the WARPFIELD tool for HII region described by Pellegrini et al. (2020)

In the next two sections of this thesis, we will explore two ways of combining multiple 1D models to describe complex objects.

Chapter 3

Chemically inhomogeneous models

3.1 The temperature discrepancy in photoionized regions

More than 50 years ago, Peimbert (1967) reported a discrepancy in the electron temperature determined with the ratio of CELs from the ions N^+, O^+, and O^{++}, and with both Balmer continuum to Balmer line of hydrogen and free-free continuum emission to high order hydrogen lines, for 5 Galactic H II regions. A higher value was found for the temperature estimated with both lower and higher ionization CELs than for the Balmer continuum or radio observations. The ratio of the CELs, Balmer continuum to Balmer line, and radio observations all have different dependence on the electron temperature, so Peimbert (1967) proposes that this discrepancy is due to fluctuations of the temperature from a volume average value. He includes in the equations for the intensity of the CELs, the $H\beta$ recombination line, and the Balmer decrement, to simulate the effect of temperature fluctuations a Taylor series expansion. Considering a gas of an average temperature $T_0{}^*$ that has small fluctuations (represented with the second order term of the Taylor expansion $t^{2\dagger}$), Peimbert (1967) found that estimations based upon CELs will indicate a temperature higher than the average value, while Balmer continuum over Balmer line will favor lower values than the average temperature. This is consistent with the values reported in the paper for the observed objects, but it must be considered that this Taylor's expansion is only valid for small fluctuations.

---

*$T_0(N_i, N_e) = \dfrac{\int T(r) N_i(r) N_e(r) d\Omega dl}{\int N_i(r) N_e(r) d\Omega dl}$

†$t^2 = \langle [(T(r) - T_0)/T_0]^2 \rangle$

Viegas & Clegg (1994) propose that high-density clumps could be responsible for the temperature discrepancy reported by Peimbert (1967). They found that the clumps require densities higher than 10^6 cm^{-3} and a filling factor* of 10^{-4} to explain the temperature differences. The main constraint is that the high-density clumps must be in a high ionization region for O^{++} to be the dominant ion.

Zhang et al. (2004) present a method for determining the electron temperature and density by comparing the observed and theoretical recombination spectrum of H (including the continuum and emission lines). They generate the synthetic spectrum considering the following processes: free-free continuum (e^- collisions with H^+, He^+, and He^{++}), free-bound continuum (recombination of H^+, He^+, and He^{++}), two photon decay of H, the stellar continuum (with a Rayleigh-Jeans approximation to a Blackbody), and the bound-bound emission lines from H^0, He^0, and He^+. They determine the electron temperature and density with this method (hereafter T_e(BJ) and n_e(BJ)) and with CELs in the optical and IR. They find that n_e(BJ) is higher than the density determined with CELs of O^+, S^+, Cl^{+2}, and Ar^{+3}, and suggest that this is due to density fluctuations in the gas. Zhang et al. (2004) also found that the temperature from both nebular-to-auroral [O III] λ 4959/λ 4363 (T_e([O III]$_{na}$)) and IR ([O III] λ 52 μm + λ 88 μm)/λ 4363 (T_e([O III]$_{IR}$)) CELs are higher than T_e(BJ) in the majority of the objects. When comparing the temperature from both CELs diagnostics, they found that about 2/3 of the objects have $T_e([\mathrm{O\,III}]_{IR}) > T_e([\mathrm{O\,III}]_{na})$, and that temperature fluctuations alone (as suggested by Peimbert 1967) cannot explain this behaviour. Zhang et al. (2004) propose a two component model with density fluctuations and found that clumps with $n_e \sim 10^5$ cm^{-3} can explain this temperature difference. This is because the critical density for IR lines is lower than for nebular-to-auroral optical lines.

Some diagnostics of the electron temperature and/or density can also be obtained from recombination lines: Wesson et al. (2005) used N II, O II, and He I recombination lines, as well as Balmer Jump, to determine temperatures of galactic planetary nebulae. They show that Te(ORLs) $\leq$ Te(He I) $\leq$ Te(H I BJ) $\leq$ Te(CELs). McNabb et al. (2013) found the same result for a series of H II regions. Peimbert & Peimbert (2013) use O II lines to obtain temperatures for H II regions, and also found they are systematically lower than the values they obtained using [O III] λ 4363/λ 5007. Richer et al. (2019) use spatial- and velocity-resolved spectroscopic observations of PN NGC 7009 (with VLT-UVES instrument) to derive electron temperature maps from O II lines, differing from the CELs-based

*For an idealized nebulae that contains small clumps of density n_e that are separated by a vacuum (zero electron density), the *filling factor* is the fraction of the total volume that is occupied by the clumps.

values in some parts of the nebula.

Méndez-Delgado et al. (2021) use He I and O II lines, Balmer and Paschen jumps as well as classical CEL ratios to determine temperatures for Herbig-Haro objects, the latest being higher than the RLs- or continuum-based ones.

Radio observations can also be used to determine electron temperature (using the critical frequency or low frequency turn-over), and electron density (using the brightness temperature), see e.g. Menon & Terzian (1965); Heckathorn (1971).

3.2 Abundance discrepancy problem

Determining the chemical abundances of photoionized regions, PNe or H II regions, is a very important tool for studying the chemical evolution of galaxies, because this estimation can give us information about the past and present of the gas in which these regions were formed.

To estimate chemical abundances in photoionized regions the direct method can be used (see sec. 2.1). This calculation involves a thorough knowledge of the atomic physics describing the processes that occur in the photoionized gas. Roughly, one can determine the abundance of a certain element, X, with respect to the hydrogen abundance, by summing up all the ionic abundances of that element (with respect to the ionic abundance of H^+). However, it is not always possible to observe, in the same wavelength range, the emission of all the ions for a single element, so an ionization correction factor (ICF) must be used to correct for the unseen ions. If we only focus on the calculation of a single ionic abundance (X^{+i}/H^+), this can be done using observations of RLs or CELs. Even though supposedly we are dealing with the same ion, as will be detailed in the next paragraphs, it has been found that the abundance estimated using RLs is systematically higher than the one obtained using CELs. This is known as the abundance discrepancy (AD) problem.

Spectroscopic observations of nine PNe and the Orion nebula, in the range from 3700 to 6750 Å, are presented in Wyse (1942). Together with the work of Bowen & Wyse (1939), these papers represent some of the first chemical abundance determinations using RLs of heavy elements in PNe. For PN NGC 7009, Wyse (1942) determines the ionic abundance of O^{++}/H^+ using about 20 RLs of O II, finding that this abundance is 500 times higher than what Menzel & Aller (1941) estimate for the same object using [O III] emission lines. This was one of the fist evidences of the AD problem.

However, Aller & Menzel (1945) report no such difference in the estimation of O^{++}/H^{+} with RLs and CELs. The abundance with CELs is estimated from the [O III] $\lambda\,4959, \lambda\,5007$ emission lines, using the method described in Menzel & Aller (1941). For the RLs, Aller & Menzel (1945) use the observations presented in Wyse (1942), and a different method[†]. Aller & Menzel (1945) find a consistency between the CELs and RLs determinations and argue that the difference reported by Wyse (1942) is not present. Also, Aller & Menzel (1945) point to an error in the rate of recombination capture considered by Wyse (1942), that should go as Z^4 instead of Z^2. Given the low resolution of the observations at that time and the lack of suitable atomic data for O II RLs, it was understandable that Aller & Menzel (1945) reported no discrepancy. With more recent data, Liu et al. (1995) find a factor of 5 between the O^{++}/H^{+} ionic abundance from RLs and CELs for NGC 7009, two orders of magnitude lower than what was reported by Wyse (1942).

Torres-Peimbert & Peimbert (1977) determine the carbon abundance for 33 PNe (correcting by the temperature fluctuations t^2 reported by Peimbert 1967, see sec. 3.1). They compare the abundances with those of the Orion Nebula and find that the average PNe values are a factor 9 higher than for the Orion Nebula (a similar result is found by Aller & Menzel 1945). Torres-Peimbert & Peimbert (1977) do not correct for fluorescence by stellar light and do not take into account the contribution by dielectronic recombination, when estimating the C^{++} abundance from the C II $\lambda\,4267.02$ + $\lambda\,4867.27$ RLs. So they mention that the difference in the abundances can be due to those two contributions to the line intensity that were not considered when estimating the ionic abundance.

To address this carbon problem, optical and UV observations of PNe NGC 6720, NGC 7009, and NGC 6853 were developed by Barker (1982, 1983, 1984). These studies show that for the three PNe the abundance of C^{++} obtained from C II $\lambda\,4267$ is larger than the estimation obtained from UV C III] $\lambda\,1906, \lambda\,1909$. For NGC 6720, the abundance obtained from RLs is 10 times larger than from UV CELs, for NGC 7009 and NGC 6853 the difference is smaller. An interesting result from these works is that for the 3 PNe the discrepancy decreases when the distance to the central star increases (until there is no discrepancy far away from the star). Similar to what is mentioned by Torres-Peimbert & Peimbert (1977), Barker mentions that the difference could be mainly due to the contribution by fluorescence from the central star.

The difference found by Wyse (1942); Aller & Menzel (1945); Torres-Peimbert & Peimbert (1977);

[†]LS coupling and transition probabilities of O II computed using the wave functions of Slater (1930)

Barker (1982, 1983, 1984) on the ionic abundances of O^{++} and C^{++} when estimated from RLs and CELs were pioneering works that reported and discussed this abundance discrepancy issue, which is yet to be fully understood. Since then, many works have been devoted to study the AD in both, H II regions and PNe (e.g., García-Rojas & Esteban 2007; Henney & Stasińska 2010; Richer et al. 2017; Peña et al. 2017; Wesson et al. 2018; Esteban et al. 2018; García-Rojas et al. 2019, and references therein).

To measure the abundance discrepancy of a given ion, X^{+i}, the ratio between the abundance obtained from RLs and CELs is used, namely, the abundance discrepancy factor (ADF):

$$ADF(X^{+i}) = \frac{\left(X^{+i}/H^{+}\right)_{RLs}}{\left(X^{+i}/H^{+}\right)_{CELs}} \tag{3.1}$$

In fig. 3.1, we present the distribution of the ADF of O^{++} for H II regions and PNe using the data from the literature collected by R. Wesson[‡]. For PNe, the data are plotted separating by single and binary central star. We can see that for PNe the ADF(O^{++}) goes to extremely high values (up to 700 for some spatially resolved observations), while for H II regions the mean ADF(O^{++}) is close to 2. In Wesson et al. (2018) a relationship is shown between binary central stars in PNe and extreme ADF values.

In Liu et al. (2001b), a correlation between the nebular electron temperature and abundance discrepancy is shown. In their figure 8, they plot the difference in temperatures estimated from [O III] $\lambda\,4363/\lambda\,5007$ and from the Balmer jump to a Balmer line (ΔT = T([O III]) - T(BJ)) vs the ADF(O^{++}) for a sample of 10 PNe and one H II region. The trend of the data is that for a higher temperature difference there is a higher abundance discrepancy (of O^{++}). A positive linear fit is also plotted considering nine of the PN with a 0.92 linear correlation coefficient.

As summarized in García-Rojas et al. (2019), in the now almost 80 years of knowledge of the AD, some scenarios have been proposed to try to explain the discrepancies in chemical abundances. However, none of these scenarios is able to fully explain the range of ADF found in both H II regions and PNe. We list below the most studied scenarios to explain the AD:

- Temperature fluctuations (t^2):

  The temperature variations (t^2, see previous section) in a chemically homogeneous photoionized gas, were proposed by Peimbert (1967) to explain the difference in temperatures from CELs of

[‡] `https://www.nebulousresearch.org/adfs/`

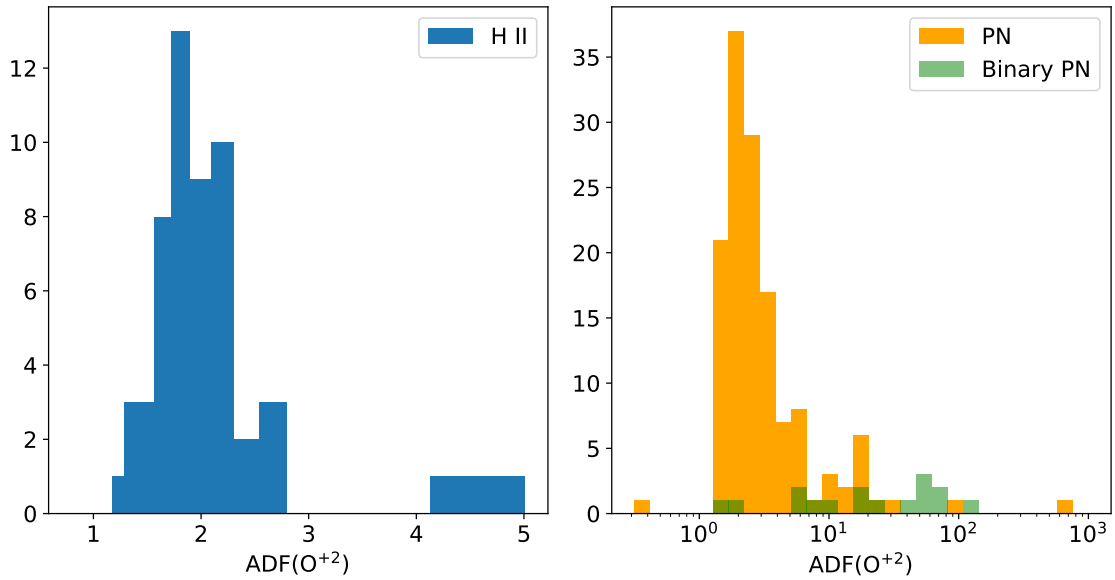

Figure 3.1: Distribution of ADF(O^{++}) for H II regions in left panel and for PNe and PNe with close binary central stars in the right panel, using the data from the literature collected by R. Wesson and available at `https://www.nebulousresearch.org/adfs/`.

[O III] and from the Balmer jump of H I. Later, in the works by Peimbert & Costero (1969); Rubin (1969) the chemical abundances of: He, C, N, O, Ne and S, for the former, and: O, N, and Ne for the latter, were determined from CELs considering such temperature fluctuations. In both works it is pointed out that without correcting for t^2, the CELs abundances are underestimated, reaching up to a factor of 3 according to theoretical models (Peimbert & Costero 1969). In Torres-Peimbert et al. (1980) the chemical abundances of C, N and O are determined from UV and optical observations of the Orion nebula and PN IC 418. The discrepancy of C^{++} when estimated from ORL C II λ 4267 and from UV CELs is studied, to see if the fluorescence by stellar radiation absorption or other recombination processes can significantly contribute to the emission of C II λ 4267, thus explaining the discrepancy. They found that C II λ 4267 is mainly produced by radiative recombination process. Finally, they mention that the difference in C^{++} with UV CELs and RLs ($\sim$ 0.2 dex) can be explained with temperature variations in the observed volume, and even mention that estimating both of these abundances can be a good way for determining the value of t^2. Some of the proposed causes for these temperature fluctuations are: gain of kinetic energy by shocks produced by the stellar winds, high density condensations, inhomogeneous dust distribution, shadows, ionization of neutral

regions by cosmic rays, variability of the ionizing source, among others (García-Rojas et al. 2019, and references therein). Under this hypothesis, the question of determining the chemical abundances of the observed gas is meaningful, and may be resolved by considering the values obtained from the RLs.

- Chemical inhomogeneities:

  Peimbert (1983) suggested an inhomogeneous distribution of carbon as a possible explanation for the abundance discrepancy of C^{++} derived from RLs (λ 4267) and UV CELs (λ 1909) in PNe. The first model with an inhomogeneous C distribution was developed by Torres-Peimbert et al. (1990), for PN NGC 4361 with ADF(C^{++}) = 14. The model had a C-rich inner shell (r_{in} = 0.056 pc, r_{out} = 0.112 pc) and "normal" composition outer shell (r_{in} = 0.112 pc, r_{out} = 0.243 pc). The inner shell with log C/H = -2, produced about 98% of the C recombination lines, 48% of Hβ, 55% of C III] λ 1909, 65% of C IV λ 1550, and about 1 - 20% of other metals CELs, with an electron temperature of about 11,400 K. The outer shell with log C/H = -3.9, was hotter with an electron temperature of 20,200 K. With this inhomogeneous model, the UV CELs of C^{++} and C^{+3} were reproduced, as well as the recombination lines of C, which was not possible with the homogeneous model. The "lower" electron temperature in the C-rich shell, enhances the emission of the carbon recombination lines, while the hotter outer shell has basically no contribution to the carbon recombination lines and emits less than half UV CELs of C, half the Hβ, and most of the other metals CELs. As it will be shown in sec. 3.5, a much lower temperature ($\sim$600 K) is needed to reproduce fainter O^{+2} RLs. However, the model in Torres-Peimbert et al. (1990) was only C-rich so the temperature can not decrease as much as it would for a region that is also O-rich ([O III] λ 5007 is a much better coolant). Under this hypothesis, the question of determining the chemical abundances of the gas is more problematic, as two (or more) sets of abundances are needed to describe the gas. The "normal" composition is obtained from the CELs, while the determination of the metal rich component composition is a challenge (see next sections).

- Kappa distribution:

  Nicholls et al. (2012) proposed that the AD could be due to variations in the Maxwell-Boltzman (MB) energy distribution of electrons, i.e., the κ-distribution, previously used to describe the electron energy distribution in the solar corona (Owocki & Scudder 1982; Dzifčáková & Kulinová 2003). This distribution deviated from the MB by having a tail of superthermal electrons that

enhanced the intensity of CELs. However Ferland et al. (2016) showed that the distances on which the heating rates change are much smaller than the distance the superthermal electrons can travel and also that the time scales for thermalizing these electrons are much shorter than the heating and cooling timescales. So even if the gas has these superthermal electrons they will be thermalized to a MB distribution before affecting the CELs. Draine & Kreisch (2018) also ruled out the hypothesis of the κ distribution, on basis related to the speed of the local relaxation to a near-Maxwellian energy distribution. They claim "there is no basis for using κ-distribution to describe the electrons in H II regions or planetary nebulae."

- Uncertainties in the atomic data:
  The atomic data can be sources of large uncertainties in the chemical abundance determinations (Juan de Dios & Rodríguez 2017). Rodríguez & García-Rojas (2010) reproduce the temperature structure (Te[N II]/Te[O III]) in nine H II regions with simple models that consider the abundances based on CELs. They suggest that the AD could be caused by errors in the recombination coefficients of the order of a factor 2, in which case the abundance from CELs would be a more reliable determination of the metallicity. Storey et al. (2017) present a detailed estimation of the recombination coefficients of O^{++} that consider determinations at lower electron temperatures and non-LTE. With these new atomic data the O^{++} abundance from RLs was not significantly changed and the AD remained.

- Fluorescence:
  Other proposed explanation for the AD was the fluorescence by star light that contributes to the emision of recombination lines (Escalante et al. 2012), but the aforementioned difference with ORL C II λ 4267 and UV CELs C II] λ 1909 can not be explained by fluorescence.

3.3 Model description

The work described in this section has been published by Gómez-Llanos & Morisset (2020), and a follow-up work on the emission of the [O III] λ 4363 line has been published by Gómez-Llanos et al. (2020), which is included verbatim in section 3.6.

There are some works where plasma with chemical inhomogeneities has been modeled, aiming to simultaneously reproduce RLs and CELs in PNe: Torres-Peimbert et al. (1990); Péquignot et al.

(2002, 2003); Tsamis & Pequignot (2004). For H II regions, metal-rich condensations or "droplets" have also been proposed to explain the ADF (Tsamis et al. 2004). The droplets are supposed to be generated by Type II Supernova and are yet to be mixed with the ISM. Stasińska et al. (2007) generates photoionization models of H II regions considering these metal-rich droplets, finding that the abundances determined with RLs highly overestimate the abundances of the mixed gas, while with CELs the abundances are closer to the abundances of the mixed gas but still slightly larger.

Péquignot et al. (2002) generates chemically inhomogeneous models of PN NGC 6153, assuming that in a later stage of evolution, the nucleus of the PN ejects H-deficient material that mixes with the inner parts, reaching pressure equilibrium with the rest of the gas. The H-deficient gas is colder (10^3 K), and condensed in smaller clumps with higher density. Models with 2 different chemical compositions reproduce most of the spectral lines observed. Tsamis & Péquignot (2005) model the giant H II region 30 Doradus and compare with observations in UV, optical, IR and radio. They find that with chemically homogeneous models the heavy elements RLs are not reproduced, while with two abundances models (a small volume of H-poor gas embedded in a large volume of "normal"-abundance gas) a better fit to the observed RLs is found. The H-poor gas contains ∼2% of the total gas mass and emits ∼8% of the total Hβ flux. Yuan et al. (2011) modeled the PN NGC 6153 with the 3D photoionization code `MOCASSIN`. They consider a chemical homogeneous model and another one with two abundances: an H-poor gas and a "normal"-abundance gas. With the chemically inhomogeneous model, they succeed in reproducing the RLs and CELs observed in the nebula.

The work presented in this and the following sections considers the bi-abundance scenario, in order to explore its effects on the determined ADF. Our goals are twofold: (1) study the possible degeneracy between the metalicity of the H-poor gas (or metal-rich) and its volume relative to the nebula; (2) show the capabilities of combining 1D models to generate topologically equivalent models (see end of Sec. 2.3) that are representative of complex objects in a short computation time, and which allows exploration of a larger parameter space.

The simulations are carried out with the photoionization code Cloudy v.17.02 (Ferland et al. 2017). We developed a script in python to manage the Cloudy inputs and outputs. It makes use of the PyCloudy library (Morisset 2013).

The RLs of O II (Storey et al. 2017), N II and C II (Pequignot et al. 1991) are not predicted by Cloudy in details, only the sum of the multiplets are computed. It is nevertheless possible to compute them

with the method `add_emis_from_pyneb` from the CLOUDY outputs. This method uses the electron temperature and density, and the corresponding ionic abundances at each radial step to estimate the emissivities of the line (vía PYNEB method Atom), and integrates the values over the volume in the same way that it is done in CLOUDY.

The emission of the central star (CS) of the PN is modelled assuming a blackbody (BB) at an effective temperature (T_{eff}) and luminosity (L). We know the blackbody option may be a bit too simple approximation, but the main effects that aim to be explored are those produced by the change of the metallicity in the gas, so we expect the BB to be a good enough approximation.

The gas distribution is modeled with spherical symmetry (CLOUDY is a 1D spherical code) and constant hydrogen density. For the chemical composition, two metallicities are considered: close-to-solar (cts) and metal-rich (mr). This is done with two independent models. One model (M_1) only has cts metallicity and is called the "normal" (N) component. The other model (M_2) has mr clumps in the inner part and cts composition in the outer regions. These components are called metal-rich (MR), and behind clumps (BC), respectively. These two models were combined to generate a bi-metallicity model. For some of the larger mr metallicities considered in the models, the radial extension from the central star to the photoionization front of the BC component is smaller than for the N component. Given than these components are combined in a spherical geometry, there is a shadow that can be ionized tangentially by the diffuse radiation of the N component at the radius between the ionization front of the BC and N components. A third model (M_3) was then computed to simulate this shadow. It only considers ionization from the diffuse radiation of the N component. This fourth component will be referred to as shadow (S). In some cases, the MR component may be optically thick, leading to the lack of the BC component: the MR component is directly followed by the S component (see Sec. 3.5.2). The contribution of the diffuse radiation from the N component on the BC component, and vice versa, are not considered since it would highly increases the complexity in the computation of the models. However, this effect is not expected to highly contribute to the ionization, since the stellar radiation will dominate the ionization. A 2D scheme combining all the components is shown in fig. 3.2, where N, MR, BC, and S are shown in blue, red, cyan, and dark blue, respectively. The different tones of blue have the same cts metallicity and the red are mr. In table 3.1, we summarize the different components, their abbreviations, the model to which they correspond, and the metallicity type.

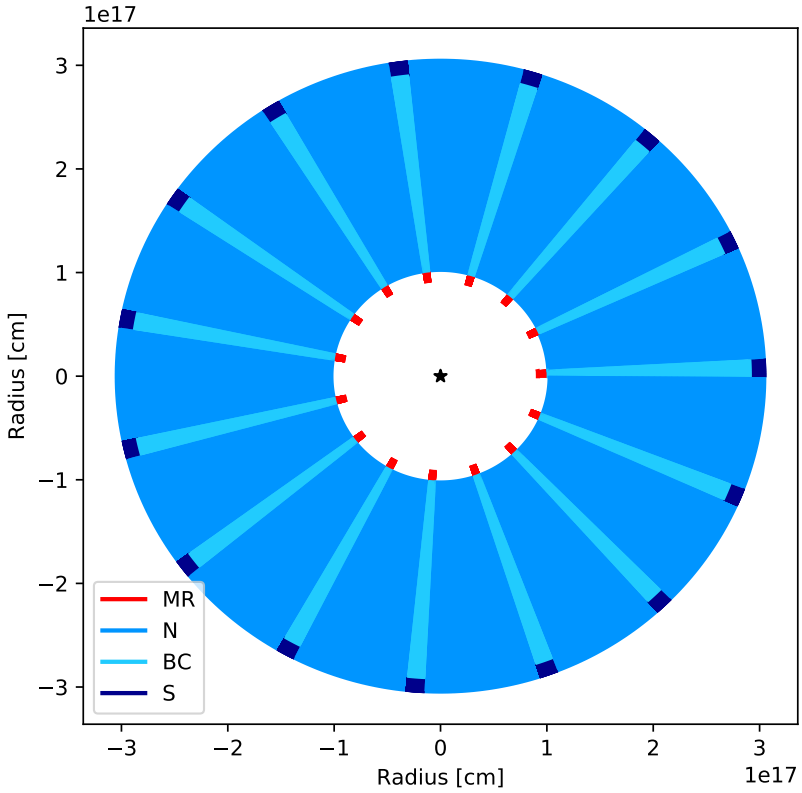

Figure 3.2: Schematic representation of the morphology of the 4 components in the PN bi-metallicity model. All blue regions are gas with close to solar metallicity, and the red regions represents metal-rich (MR) clumps that in this case are about 630 times more metallic. The blue region is the "normal" gas (N), the cyan region is the gas behind the clumps (BC), and the dark blue region is a shadow (S) ionized by the diffuse of the normal component. The fraction of solid angle for: MR, BC and S is $\Omega/4\pi = 0.25$. This detailed description of the morphology of the object shown here is topologically equivalent to only 4 1D models, see end of Sec. 2.3.

Table 3.1: Some properties of the four components used to build the PN model in this work.

Name	Abbreviation	Model	Metallicity
"normal"	N	M_1	close to solar
metal-rich	MR	M_2	rich
behind clump	BC	M_2	close to solar
shadow	S	M_3	close to solar

3.3.1 Normal component

This is the main component of the nebula, referred as the N component. It is compared to the observations of PN NGC 6153 in the UV, optical and IR (Pottasch et al. 1984; Liu et al. 2000). Yuan et al. (2011, hereafter Y11) developed a chemically inhomogeneous 3D model with the code MOCASSIN to reproduce the observations of this PN. In this work we use the model by Y11 as a base, with the purpose of exploring in detail the metal-rich (H-poor) component.

The T_{eff} and luminosity we initially adopt to ionize this component are 92 kK and $1.3{\times}10^{37} erg/s$, based on the B_n model by Y11. The chemical abundances in this region are presented in table 3.2 and are based on the B_n model of Y11. For the elements not presented in Y11 for the B_n model, the abundances are set at the solar values. From the HST/WFPC2 observations of the Hα surface brightness distribution in NGC 6153 presented by Y11, we consider an inner and outer radius for this component of 5 arcsec and 15 arcsec, respectively. The distance to NGC 6153 is 1.36 kpc (Gaia Collaboration 2018), thus the inner and outer radii are $1.02{\times}10^{17}$ cm and $3.05{\times}10^{17}$ cm, respectively.

Based on the density distribution proposed by Y11, we consider a constant hydrogen density of 3000 cm^{-3}. However, when estimating the total $H\beta$ flux we find that it is the double of the observed value (with the previously mentioned parameters), so we add a filling factor and lower the hydrogen density (1000, 1500, 2000 and 2500 were explored). The best fit for the total $H\beta$ flux is found with a filling factor of 0.6 and hydrogen density of 2500 cm^{-3}.

To see if the ionization stage is well reproduced, we compare the observed and modeled ratio of emission lines for the same elements but different ion, like [S III]/[S II] or [O III]/[O II] line ratios. The modeled values are higher than the observed in NGC 6153, so we lower the luminosity. The

Table 3.2: Chemical abundances of the N region in units of 12+log(X/H).

He = 11.00	Al = 6.45	Ti = 4.95
B = 2.70	Si = 7.54	V = 3.93
C = 8.50	P = 5.41	Cr = 5.64
N = 8.58	S = 7.24	Mn = 5.43
O = 8.75	Cl = 5.37	Fe = 6.18
F = 4.56	Ar = 6.46	Co = 4.99
Ne = 8.25	K = 5.03	Ni = 6.22
Na = 6.24	Ca = 6.34	Cu = 4.19
Mg = 7.58	Sc = 3.15	Zn = 4.56

difference can be at least partially attributed to the different value for the distance considered by Y11, of 1.5 kpc (Péquignot et al. 2003), and the smaller value of 1.36 kpc we consider, estimated from Gaia Collaboration (2018). The luminosity is lowered to $9{\times}10^{36}\,erg/s$, and a simultaneous fit of $H\beta$ and ionization stage is achieved.

We include dust in the model with graphite and silicate composition, and a size distribution with slope -3.5 and ten sizes in the $0.005\mu m$ - $0.25\mu m$ range. The dust to gas ratio by mass that leads to a better fit of the IR observations (see sec 3.5.1) is $4.2{\times}10^{-3}$. This value is 2/3 the ISM canonical value in Cloudy.

The electron temperature, density, ionic fractions of H^+, He^+, and He^{++}, and O^+, O^{+2}, and O^{+3}, as a function of depth, are presented in solid lines of fig. 3.3. From the panels of the figure we can see that: there is a fall in the electron density (top-right panel) at a depth near to $6{\times}10^{16}$ cm that coincides with the depth at which the dominant ion for He changes from He^{++} to He^+ (see bottom-left panel). Also that the electron temperature ranges between 13000 and 9000 K (top-left panel). Finally, we can see that the dominant ion in the inner parts of the N component is O^{+3}, and O^{+2} in the outer parts.

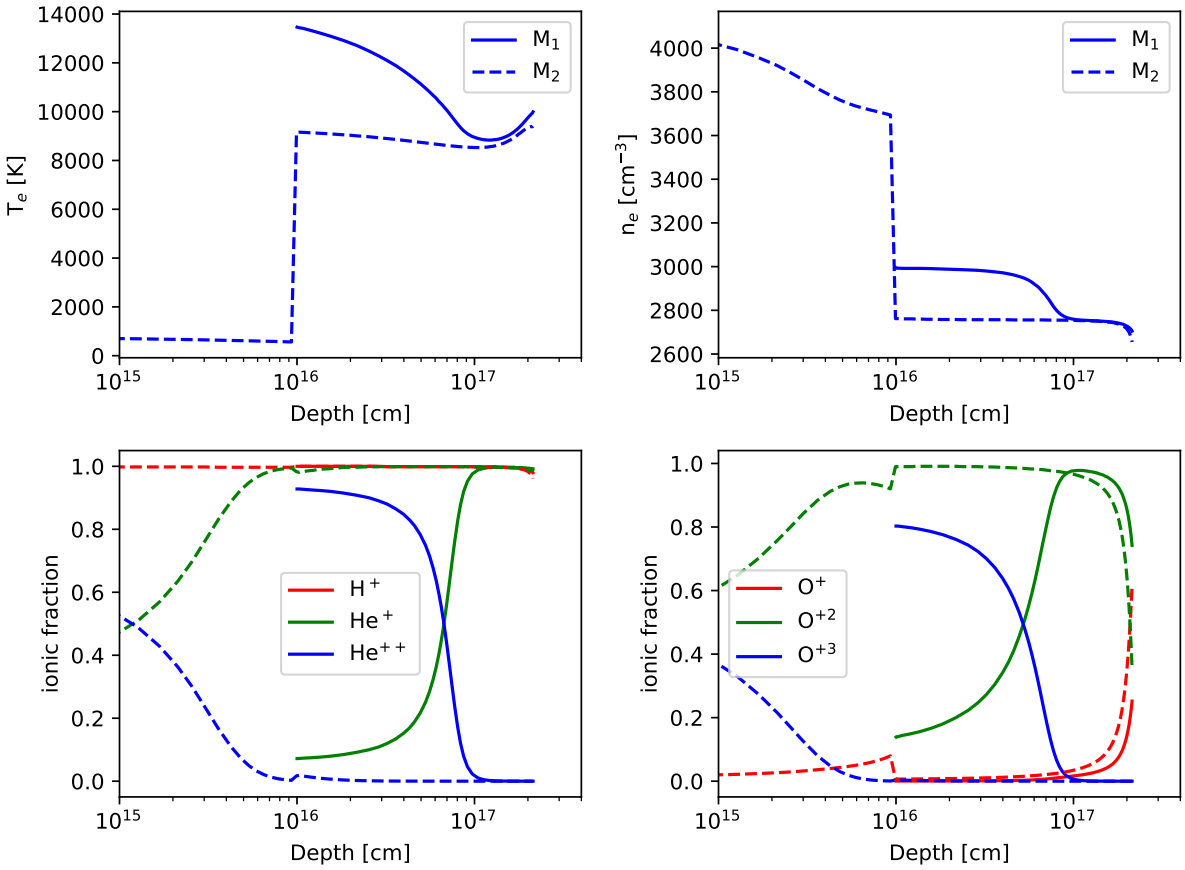

Figure 3.3: Solid line is for model M_1 that represents the N component (sec. 3.3.1) and dashed line is for model M_2 that represents: the MR component with log(ACF) = 2.1 (sec. 3.3.2) and the BC component (sec. 3.3.3). The x-axis runs on Depth, the radius of the model minus the inner radius of the MR component. Top left panel: electron temperature. Top right panel: electron density. Bottom left panel: ionic fraction of H^+, He^+ and He^{++} in red, green and blue, respectively. Bottom right panel: ionic fraction of O^+, O^{+2} and O^{+3} in red, green and blue, respectively.

3.3.2 Metal-rich component

This region is composed of metal-rich clumps placed in the inner parts of the nebula, it is referred as MR component. The radial size of the clumps is a free parameter that we choose to fix at 0.5 arcsec. The inner radius and outer radius in this region are 4.5 arcsec and 5 arcsec, respectively. To the distance of 1.36 kpc, this corresponds to a physical size of 9.2×10^{16} cm and 1×10^{17} cm. Tsamis et al. (2008) used PNe observations obtained with VLT-Flames to set an upper limit of hypothetical metal rich cold structures to ∼1000 AU, corresponding to 1.5×10^{16} cm, about twice the size of the clumps in our models ($8\times10^{1}5$ cm). Variations of these values for the radius are explored and discussed in sec. 3.5.2, to see the effects of our assumptions.

The MR component is computed in a spherical 1D Cloudy model, then combined with the other components to get the modeled nebula (see sec. 3.3.5) the fraction of volume occupied by the MR component is varied, based on the solid angle of the nebula.

The T_{eff}, hydrogen density, and He/H abundance are the same as for the N component. Other density and helium values are explored in sec. 3.5.4. In the two component model for NGC 6153 presented by Tylenda et al. (2003), a similar density for both components gives a better fit of the observations.

The MR and N components are not supposed to be in contact, so no hypothesis for pressure equilibrium is considered. We are here dealing with a model that is built to take into account the differences from a simple one-component chemically homogeneous model, important differences that are needed to reproduce the observed high values of ADF. The complexity of our model resides in the assumption of 2 main components of very different chemical compositions. This description implies the presence of two secondary components (BC and S), but the principal predictions that will be compared to the observations (namely emission line ratios) are mainly obtained from the weighted sum of the emission issued from the total volume of the N and MR components. The reality is certainly more complex than this rather simple description, and some emission also arises from the interface between the different components, in an "inter-component" medium. We then make the implicit hypothesis that the emission line ratios computed in our modeling process, and compared to the observations, are dominated by what comes from the volumes of the 4 components we considered, and that the interfaces are acting as negligible second order effects. The importance of the surface of a region of space, compared to its volume, for a reasonable almost spherical shape (no fractal shape here) is

directly related to its geometrical size: smaller volumes have relatively more surface. Our hypothesis that the high ADF PNe can be modeled neglecting the interfaces between the components (surface effects) implies that the MR regions, or clumps, are not too small. The temporal persistence of these clumps also implies that they are not too small, because their eventual evaporation or dilution timescale also depends on the ratio between their volume and their surface, being their characteristic geometrical size. To our knowledge, no actual instrument has been able to map those MR clumps.

For the chemical abundances of elements heavier than He, different values are explored. They are proportional to the abundances in the N component as follows:

$$\left(\frac{X}{H}\right)_{MR} = \left(\frac{X}{H}\right)_{N} \cdot ACF(X) \tag{3.2}$$

were $ACF(X)$ is the proportional factor named abundance contrast factor. The increase in the abundance is considered equal for all the elements in a given model run.

This MR component does not contain dust, because the dust in the other components with *cts* metallicity (N, BC, S) with a dust to gas ration (D/G) smaller than the canonical value reproduces the observations, and it is even slightly high at shorter wavelengths (see sec. 3.5.1). Given that the MR component is closer to the star, adding dust in this region will increase the emission at the shorter wavelengths (Gómez-Llanos et al. 2018), which is an unwanted outcome. The opposite case of all the dust being concentrated in the MR component is discussed in sec. 3.5.1.

For a ACF(X) = 2.1 dex, the electron temperature, density, and ionic fractions of H, He, and some O ions, are presented in dashed lines of fig. 3.3, as a function of depth. The model that computes the MR component also includes another component (BC, see next section) with *cts* metallicity for R $\geq$ 5 arcsec. The values in fig. 3.3 that correspond to the MR component, have a depth smaller than $10^{16}\,cm$. In the upper-left panel we can see that the electron temperature of the MR component is about 650 K, a very low temperature due to the large amount of metals that are contributing to the cooling of the gas (see sec. 1.1.3). From the upper-right panel we notice that the electron density is about 30% higher than in the N component, since the contribution of the metals in the electron density becomes more important due to their higher abundances. From the bottom-left panel we see that the hydrogen is fully ionized and the He^{+} is the dominant ion in the MR component. Finally, in the lower-right panel we notice that O^{+2} is the dominant ion in the MR component, while for the N component the dominant ion in the inner parts is O^{+3}. The ionization source is the same for both components, but the O/H is 2.1 dex higher in the MR so the amount of photons with energy $h\nu >$

54.9 eV (required to ionize O^{+2}) is not enough in the MR component to make O^{+3} the dominant ion. We see that as we approach the transition zone between the MR and BC components the O^{+2} begins to decrease and the O^{+} starts to increase, possibly indicating that the photons with energies $h\nu > 35$ eV are diminishing. At larger depths ($>10^{16}\,cm$), when the BC component begins and the metallicity is back to the *cts* value, the O^{++} increases again and remains the dominant ion in this component. Also the increase of the electron density that enhances the recombination rate, or the contribution to the opacity from other ions like He^{++}, C^{+3}, N^{+3} can have an effect on the ionization structure. To confirm if the decrease in O^{++} at the end of the MR component is due to the large absorption of photons with $h\nu > 54.9$ eV, we compute the optical depth at the outer radius of the MR component for different values of the ACF. This is shown in fig. 3.4, where dashed vertical lines denote the IP of some important ions. We see that the gas is optically thin at most energies, for ACF < 2.0 dex. For ACF $= 2.0$ dex, the optical depth at 35 eV is very close to 1, and larger than 1 for higher energies, confirming our assumptions. This increase in the optical depth of the MR component (at higher ACF values), will have an effect on the ionization stage of the BC, as it will be discussed later.

In the top panel of fig 3.5 the volume integrated ionic fractions (obtained through PyCloudy facilities) of O^{+}, O^{+2}, and O^{+3} are plotted as a function of the ACF for the MR component. For ACF < 1.4 dex the dominant ion is O^{+3}, for 1.4 dex $\leq$ ACF < 2.6 dex it is O^{+2}, and for ACF ≥ 2.6 dex it is O^{+}.

The outer radius of the MR component is imposed to be 5 arcsec, making this region matter bounded (at least at lower ACF). When the ACF increases the opacity increases and the Strömgren radius decreases, so for the most extreme values of ACF the MR component starts to transition to a radiation bounded region.

3.3.3 Behind clump component

As mentioned in the previous section, in the same run of the model (M_2) that generates the MR component, the behind clump (BC) component is computed in the immediately higher radial values. The chemical abundances and dust composition of the BC component are the same as for the N component. The command *function* of Cloudy is used to consider dust only at radius ≥ 5 arcsec, where the BC component begins. To change the chemical abundances between the MR and BC

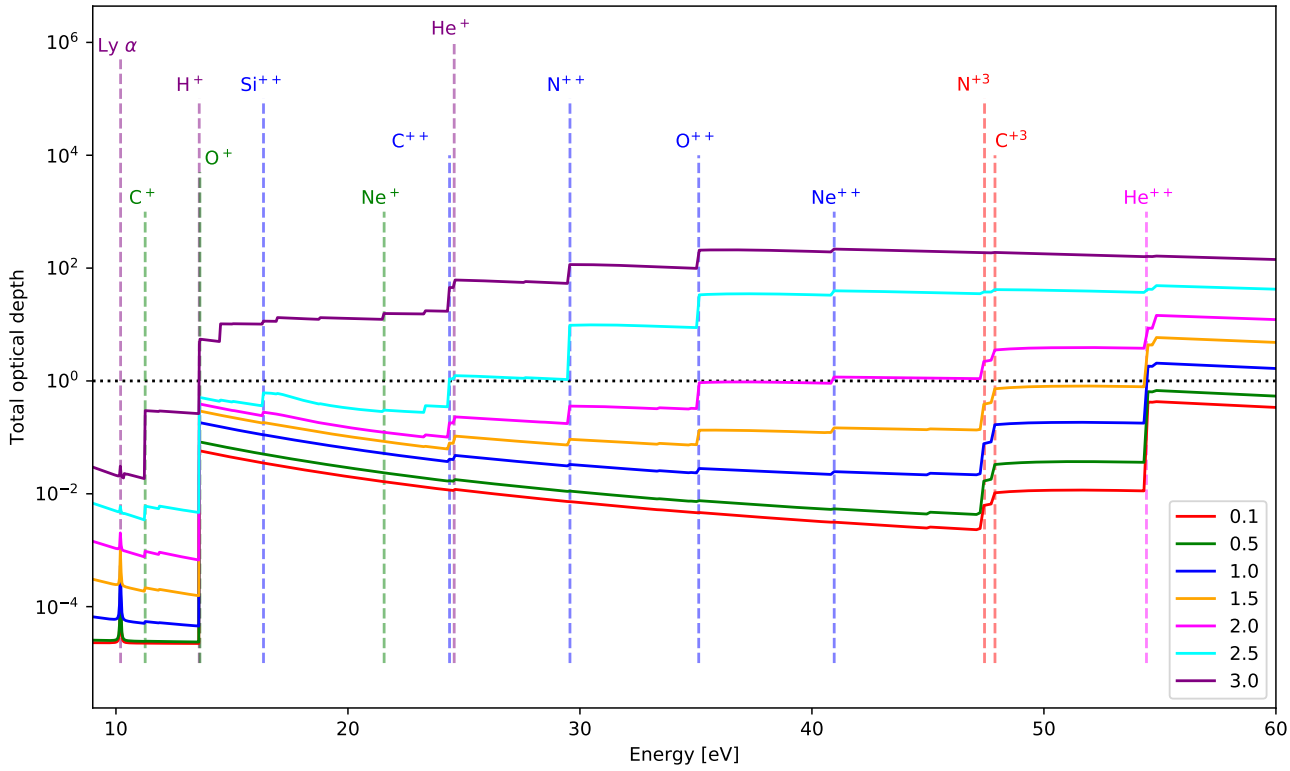

Figure 3.4: Total optical depth as a function of energy in eV. The values are measured at the outer radius of the MR component for ACF(X): 0.1, 0.5, 1.0, 1.5, 2.0, 2.5 and 3.0 dex. The horizontal black dotted line indicates the optical depth equal to 1. The vertical dashed lines denote ionization potentials, for H and He: purple (magenta) represents once (twice) ionized, for metals: the colors green, blue, and red are for once, twice, and tree times ionized, respectively.

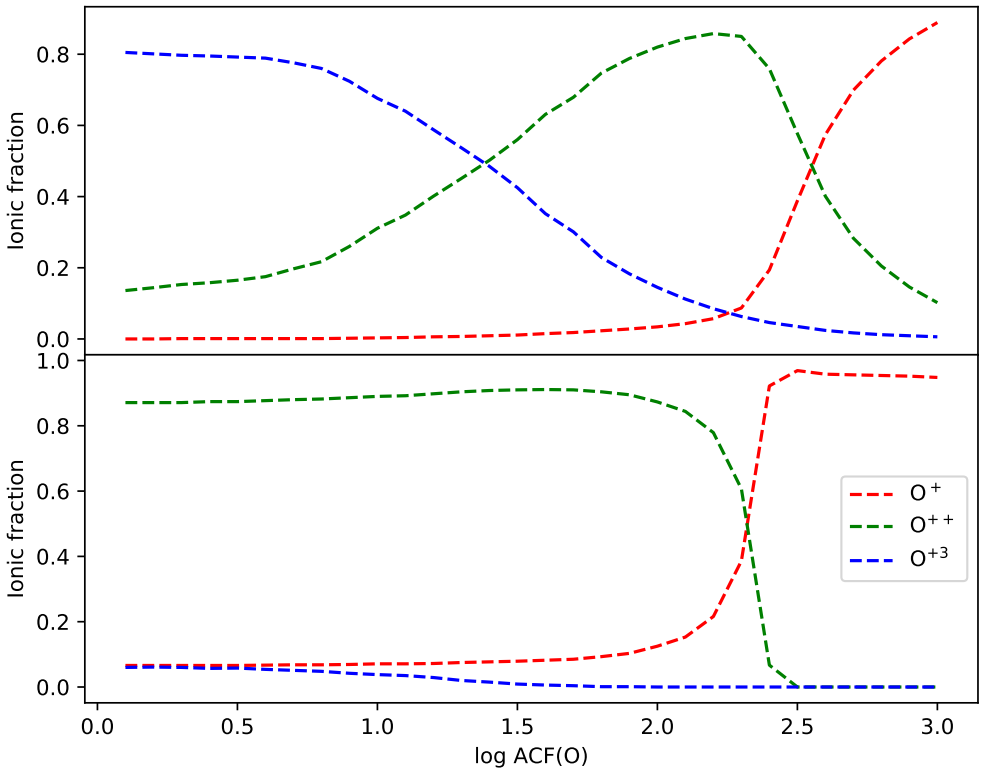

Figure 3.5: Distribution of the ionic fraction integrated over the volume of O^{+}, O^{++}, and O^{+3} in red, green and blue dashed lines, respectively, as a function of the ACF(O) for the MR (BC) component in the top (bottom) panel.

components, a step function is used.

The hydrogen density and inner radius in BC are set equal to those in N. The N component is matter-bounded, with an outer radius of 15 arcsec. The outer radius of the BC is also defined at 15 arcsec, but since there is another gas component in the inner parts (MR component), some of the radiation gets absorbed, increasing as a function of the ACF. To see the effects this has on the outer radius and ionization parameter of the BC component, we plot in orange dots of fig. 3.6 the outer radius and mean ionization parameter as a function of the ACF in the top and bottom panels, respectively. As a reference, the values for the MR and N components, are plotted as green and orange solid lines, respectively. For the MR and N components, the values are basically constant for both outer radius and mean ionization parameter. While for the BC component, the outer radius decreases for ACF > 2.5 dex (due to the radiation absorption by the MR component) transitioning from matter bounded to radiation bounded. The ionization parameter is inversely proportional to the square of the radius of the nebula[§], so the mean ionization parameter[¶] increases with decreasing the outer radius (when the inner radius is kept constant). This behaviour is shown in the bottom panel of the figure for the BC component.

To see which is the dominant oxygen ion in the BC component, we plot in the bottom panel of fig. 3.5 the volume integrated ionic fraction of O^{+}, O^{+2}, and O^{+3} as a function of the ACF(O) for the BC component. We see that O^{+2} is the dominant ion for ACF < 2.3 dex, and that O^{+} dominates for ACF ≥ 2.3 dex. For ACF ≥ 2.5 dex, there is almost no O^{+2} left in the BC region. This will have an important effect on the emission of the lines [O III] $\lambda\,4363, \lambda\,5007$, which are used in the temperature and abundance estimations that will be performed in the following sections.

3.3.4 Shadow component

The MR, BC, and N components are combined in a composite model to simulate a two-metallicities PN (see sec. 3.3.5 and fig. 3.2). In a few cases where the ACF is large (> 2.5 dex), the radial distance of the ionization front in the BC component is smaller than for the N component (see fig. 3.6). If we consider that there is still gas in the radial direction between r_{out}^{BC} and r_{out}^{N}, there will be a region

[§]ionization parameter: $U = \dfrac{Q_0}{4\pi\, r^2\, n_{\rm e}\, c}$

[¶]mean ionization parameter: $< U >= \dfrac{\int U dV}{V}$

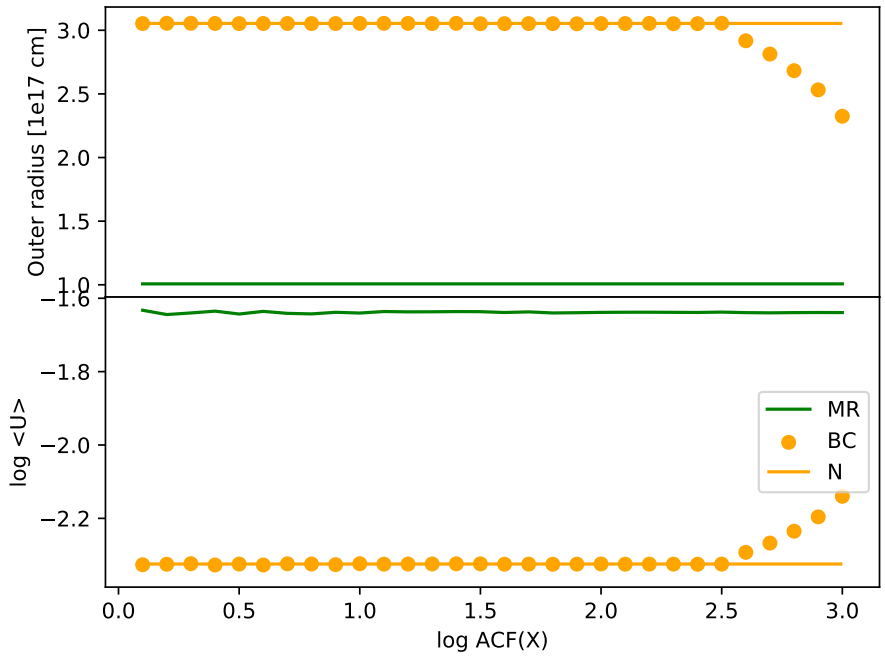

Figure 3.6: Outer radius and mean ionization parameter of the BC, MR and N components as a function of the ACF(X).

of neutral gas that can be ionized tangentially by the diffuse radiation (Lyman recombination) of the N component. We will call this the region shadow (S). A 2D schematic example of this shadow is shown in fig. 3.7, where the red is for MR component, cyan for the BC component, blue for the N component, and dark blue for the S component. The hν black arrows represent the direction of the diffuse radiation coming from the N component that will ionize the S component. The region of transition between the BC and S component is marked with an arrow (BC recombination front).

This shadow has been modeled in a single CLOUDY run (model M_3), to get a representative idea of the contribution of this region. The chemical abundances and dust in M_3 are the same as in the Ncomponent. Given that the shadow is not ionized directly from the star, instead of a blackbody, the SED in this model is given by the diffuse nebular continuum of the N component at a radius that is half the nebular size. The luminosity is given by the integral of the incident radiation field in the N component from the minimum wavelength up to 912 Å.

The radial direction in the M_1 model of the shadow corresponds to the tangential direction in fig. 3.7, same as the directions of the arrows $h\nu$ of the figure. The upper limit of the tangential size of the shadow (a in fig. 3.7) is constrained to a value small enough so there is no neutral tube on the inner parts of the shadow region.

The electron temperature in the S component is approximately constant at 6300 K. The N temperature at the same radius (≈9000 K) is 30% higher than in the S component. There should be a small rise in the electron density of the S component to get pressure equilibrium with the N component, but given the way the S model is independently constructed this is not taken into account.

3.3.5 Combined bi-abundance model

To get the emission of the simulated two metallicities PN, we combine the N, MR, BC, and S components (the shadow is included when ACF is very high) in a spherical shape, computed in the M_1, M_2, and M_3 models. The fraction of volume occupied by each region is defined by the covering factor, which is the fraction of solid angle of each component over the total solid angle ($\Omega_{total} = 4\pi$).

To get the intensity of a line, the weighted sum of the intensity for each component is done as follows:

$$I_\lambda = I_{\lambda,N}\left(\frac{\Omega_N}{4\pi}\right) + I_{\lambda,MR}\left(\frac{\Omega_{MR}}{4\pi}\right) + I_{\lambda,BC}\left(\frac{\Omega_{BC}}{4\pi}\right) + I_{\lambda,S}\left(\frac{\Omega_S}{4\pi}\right) \tag{3.3}$$

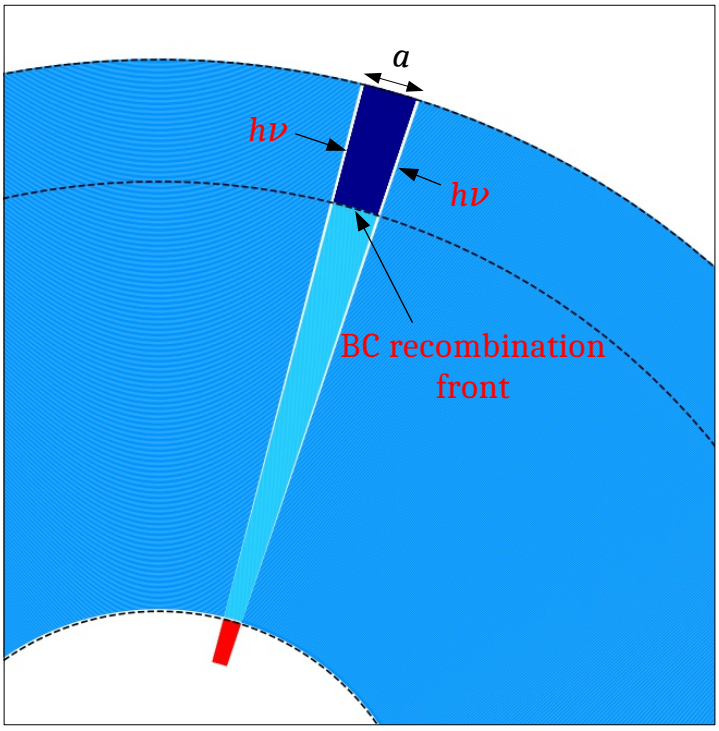

Figure 3.7: Scheme characterizing the parameters of the S component. Colors represent the same regions as in figure 3.2. The outer part of the S region has an arc length of a, the $h\nu$ arrows represent the direction of the diffuse ionizing photons coming from the N component to ionize the S region.

where $I_{\lambda,X}$ is the intensity at the wavelength λ of the component X, and $\Omega_X/(4\pi)$ its corresponding covering factor. For the S component, the intensity $I_{\lambda,S}$ already considers the shadow thickness (which is a function of the ACF). For the way the components are combined in a spherical morphology (like shown in fig. 3.2), the covering factor of the MR, BC and S are equivalent. We are mainly interested in the volume contribution of the MR component, so in the following when we talk about the covering factor we will be referring to that of the MR component (that is the same than for BC and S), and it will be simply denoted by $\Omega/(4\pi)$. In such a notation, the eq. 3.3 becomes (see fig. 3.2):

$$I_\lambda = I_{\lambda,N}\left(1-\frac{\Omega}{4\pi}\right) + I_{\lambda,MR}\left(\frac{\Omega}{4\pi}\right) + I_{\lambda,BC}\left(\frac{\Omega}{4\pi}\right) + I_{\lambda,S}\left(\frac{\Omega}{4\pi}\right) \tag{3.4}$$

For the MR (and external BC and S) component, it can be considered a single clump with $\Omega/(4\pi)$ or n clumps with $\Omega/(4\pi\, n)$. To exclude the possibility of having a neutral tube on the inner parts of the S component (which can occur for large values of the shadow tangential size a), we consider n clumps such that the shadow tangential size a meets that condition. We are mainly interested in exploring the effect that changes in the metallicity (ACF) and covering factor ($\Omega/(4\pi)$) have on the line emissions. A grid of bi-abundance models is performed, with ACF varying from 0.1 to 3.0 dex (step of 0.1 dex) and with $\Omega/(4\pi)$ varying from 0.01 to 0.5.

3.3.6 Reference object: PN NGC 6153

To constrain the input parameters of the models and compare the results with observed values, we use the observations of NGC 6153, which is a bright PN at a distance of 1.36 kpc (Gaia Collaboration 2018). It has an angular size of 32" x 30" in the near-IR (Skrutskie et al. 2006). The observations are taken from Liu et al. (2001a), who used the 1.52 m ESO telescope with the B&C spectrograph and a 3.5 arcmin long and 2 arcsec wide slit. The spatial sampling was 1.63 arcsec per pixel. The observations cover both minor axes of the nebula, with the slit positioned at a PA of 122.8° and centered on the central star, and across the nebula by scanning with the slit oriented north-south. Medium resolution spectra were obtained (FWHM = 1.5Å) in the spectral range: $\lambda\,3040 - \lambda\,4990$ for the minor axis and $\lambda\,4005 - \lambda\,4990$ across the nebula. For the spectral range near to $\lambda\,3500 - \lambda\,7400$ a lower resolution (FWHM = 4.5Å) was obtained for both the minor axis and across the nebula. The data was deredened with a Howarth (1983) extinction curve with a c($H\beta$) = 1.3 and R_V = 3.1. With these observations, an ADF(O^{++}) = 9.2 was estimated by Liu et al. (2000).

Table 3.3: Atomic data selected from PyNeb that are used in the determination of physical parameters and chemical abundances.

Collisionally excited lines		
Ion	Transition probabilities	Collision strength
N^{+}	Froese Fischer & Tachiev (2004)	Tayal (2011)
O^{+}	Froese Fischer & Tachiev (2004)	Kisielius et al. (2009)
S^{+}	Podobedova et al. (2009)	Tayal & Zatsarinny (2010)
O^{++}	Froese Fischer & Tachiev (2004)[a]	Storey et al. (2014)
Cl^{++}	Kaufman & Sugar (1986)[b]	Butler & Zeippen (1989)
Ar^{3+}	Mendoza & Zeippen (1982)	Ramsbottom & Bell (1997)
Recombination lines		
Ion	Recombination coefficients	Case
H^{+}	Storey & Hummer (1995)[c]	B
He^{+}	Smits (1996)	B
He^{++}	Storey & Hummer (1995)	B
O^{++}	Storey et al. (2017)	B

[a] Storey & Zeippen (2000) for transitions 4-2 and 4-3.

[b] Mendoza (1983) for transition 4-3.

[c] Extrapolation for low T_e (< 500 K).

3.4 Plasma diagnostics

The emission lines from the bi-abundance model, estimated from eq. 3.4, are used here to determine physical conditions and chemical abundances following the same procedure as for observed objects.

The electron temperature and density and ionic abundances are estimated with PyNeb. The atomic data used for such determinations are listed in table 3.3. For HI, the data of Storey & Hummer (1995) were extrapolated when electron temperatures were lower than 500K.

3.4.1 Diagnostics with CELs

We use the line ratios [O III] λ 4363/λ 5007 and [Cl III] λ 5538/λ 5518, to simultaneously determine the electron temperature and density with the getCrossTemDen method of the Diagnostics class of PyNeb. This method requires the line intensity ratios of both ions (O^{++} and Cl^{++}), which are estimated for each value of ACF and $\Omega/(4\pi)$ explored, from eq. 3.4. The results of the physical determinations are shown in fig. 3.8, where the x-axis represents the ACF, the y-axis $\Omega/(4\pi)$ and the color bar in the upper (lower) panel denotes the estimated electron temperature (density). We see that the changes in electron temperature and density are about 400 K and 50 cm^{-3}, respectively, for the entire ACF-$\Omega/4\pi$ plane. The fact that the changes in temperature and density are not large is an expected result, since the MR component will not have a large contribution to the CELs due to its low temperature. Almost independently of the value of $\Omega/(4\pi)$, for ACF values going from 0.1 to 2.3 dex, the electron temperature slowly decreases, however at 2.4 dex there is an abrupt increase on the temperature. The turn on the direction of the electron temperature is caused by the change in the ionic fraction O^{++}/O of the BC component at 2.3 dex (see bottom panel of fig. 3.5). The intensity of the [O III] λ 4363 line in the MR component has a contribution due to recombination that affects the temperature estimation, since the recombination is included in the Cloudy models but the temperature determination with PyNeb only considers the population of levels by collision (see sec. 3.6, for a larger discussion on this subject).

3.4.2 Electron temperature from the Balmer jump

Another way to estimate the electron temperature of the gas is with the ratio of the hydrogen Balmer jump to a Balmer line (Peimbert 1967). We will call this Balmer jump temperature T(BJ). From the recently implemented `Continuum` class of PyNeb (Morisset et al. 2020), the T(BJ) can be estimated. For this, the parameters needed are: (1) the continuum before and after the jump (in erg s^{-1} cm^{-3} Å^{-1}), we choose the wavelengths 3643 Å and 3861 Å, respectively, (2) the intensity of a Balmer line, we use H 11 (in erg s^{-1} cm^{-3}), (3) the electron density, for which we use the one estimated from the line ratio [Cl III] λ 5538/λ 5518 in the previous section, and (4) He^+/H^+ and He^{++}/H^+. Since the helium abundances are dependent on the electron temperature (and density), we use an iterative process to simultaneously obtain the T(BJ) and the He^+/H^+ and He^{++}/H^+ abundances. The `getIonAbundance` method of PyNeb is used to determine the helium ionic abundances, with

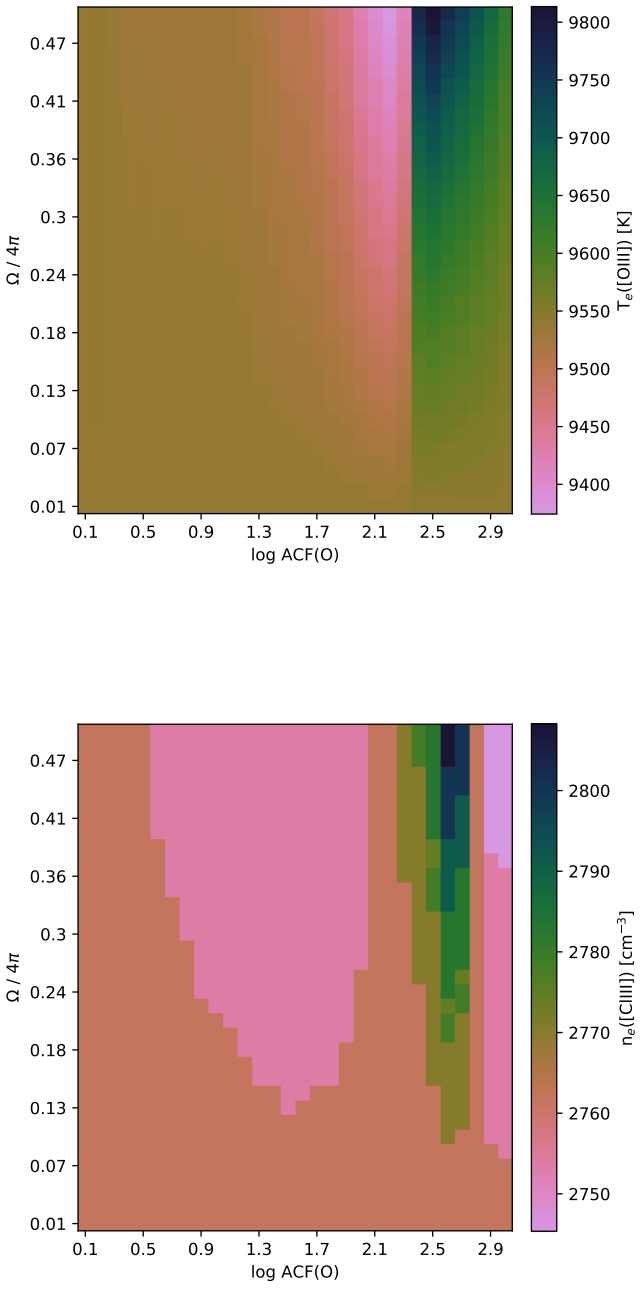

Figure 3.8: Top (bottom) panel: the color represents the electronic temperature (density) estimation for the bi-abundance models (see sec. 3.3.5). The x-axis represents the variations in the ACF for oxygen (see eq. 3.2) and goes from 0.1 to 3.0 dex. The y-axis represents the covering factor of: the metal-rich clumps, the gas behind the clumps and the shadow, in the range of 0.01 to 0.50. Diagnostics are made with the sensitive line ratios: [O III] λ 4363/λ 5007 and [Cl III] λ 5538/λ 5518. The contribution due to the recombination in the intensity of [O III] λ 4363 is taken into account. Line intensities of the bi-abundance models are obtained using eq. 3.4.

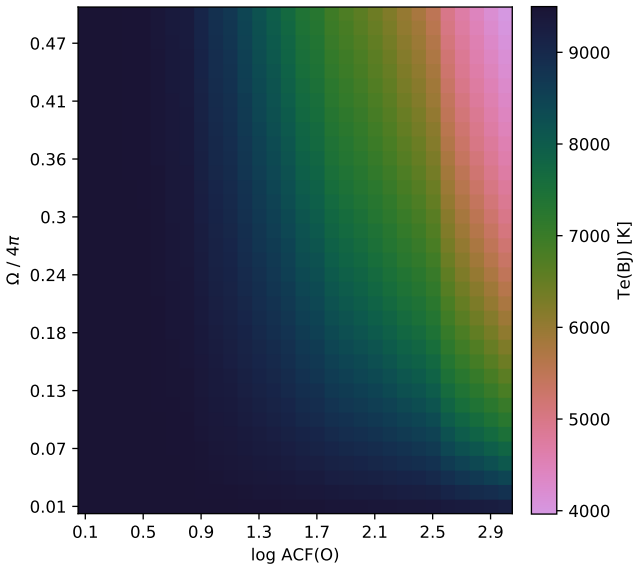

Figure 3.9: Same axis as figure 3.8. The color represents the Balmer jump temperature determination for the bi-abundance models.

the emission lines He I 4471, 5876, and 6678Å for He^+, and He II 4686 Å for He^{++}, all normalized to Hβ. For the ACF-$\Omega/4\pi$ map, T(BJ) is shown in fig. 3.9. We notice that unlike the temperature estimated from CELs of O^{++} (top panel of fig. 2.4), the changes in the Balmer jump temperature are large, ranging from 4000 to 9600 K. The temperature is almost constant for lower values of ACF and $\Omega/4\pi$ with a value of about 9,500 K, while for higher values of ACF or $\Omega/4\pi$ the temperature decreases, reaching its minimum at $\sim$ 4,200 K for the highest value of ACF and $\Omega/4\pi$ explored.

3.4.3 O^{++}/H^+ ratio from CELs

We estimate the O^{++}/H^+ ratio for the ACF-Ω map with the [O III] λ 5007 CEL in two ways: (1) taking the T([O III]) for both O^{++} and H^+, and (2) taking T([O III]) for O^{++} and T(BJ) for H^+. In fig. 3.10 we show the first determination. The second determination is very similar to the first one, except for the models with high ACF and high Ω (top-right corner of fig. 3.10), for these models the first determination is larger than the second one, the largest difference being 0.3 dex. This is because at high ACF and high Ω the T(BJ) is lower (see fig. 3.9), and the emissivity of H^+ increases. We notice a 0.3 dex decrease of O^{++}/H^+ at high Ω and ACF larger than 2.3 dex. This is due to the

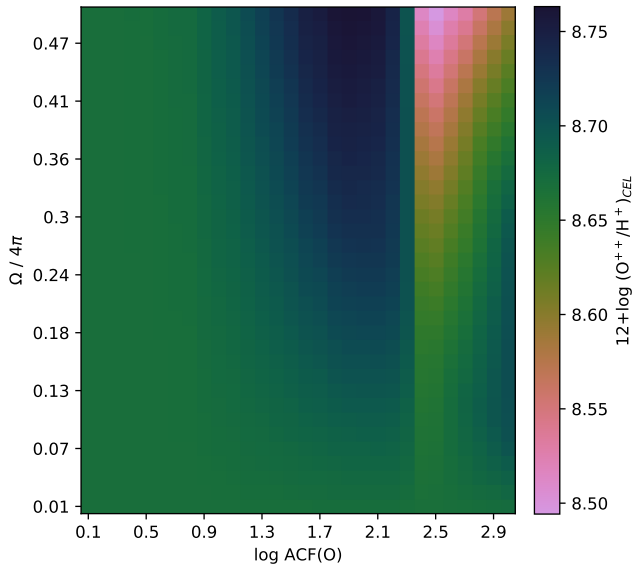

Figure 3.10: Same axis as figure 3.8. The color represents the O^{++}/H^{+} ionic abundance estimation with CELs for the bi-abundance models, using the [O III] temperature for O^{++} (shown in top panel of fig. 3.8), and the Balmer jump temperature (shown in fig. 3.9) for H^{+}.

abrupt decrease of O^{++}/O from the *BC* region (see bottom panel of fig. 3.5). In this high ACF regime (> 2.3 dex), at constant ACF the contribution of the *BC* region decreases when Ω decreases. On the other hand, at constant Ω the outer radius of the *BC* region decreases when the ACF increases (see top panel of fig. 3.6). In both cases the contribution in volume of the *BC* region to the total O^{++}/H^{+} is smaller. Since there is less (if any) O^{++} in this region (at high ACF) the total O^{++}/H^{+} increases again.

The value of 12 + log O/H used in the *cts* components (*N*, *BC*, and *S*) is 8.75. The value obtained from the CELs is slightly lower than this value, because of the ionic fraction O^{++}/O being lower than one. The ionic abundance of O^{++}/H^{+}, is obtained by integrating over the volume of the nebula the contribution of the *N*, *BC*, and *S* regions (no contribution from *MR* is taken into account, as this region does not emit [O III] λ 5007), and the value is close to both empirical determinations, being slightly closer for the T(BJ) estimation.

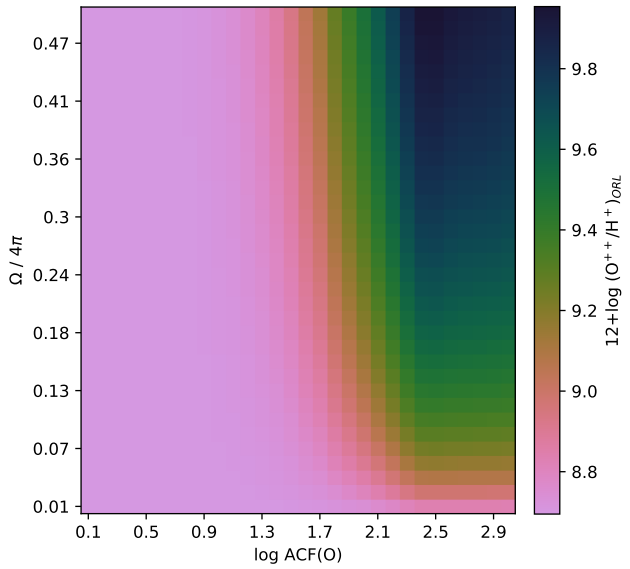

Figure 3.11: Same axis as figure 3.8. The color represents the O^{++}/H^{+} ionic abundance estimation with RLs for the bi-abundance models, using the Te(BJ) (shown in fig. 3.9).

3.4.4 O^{++}/H^{+} ratio from RLs

We determine the O^{++}/H^{+} ratio of the ACF-Ω grid making use of the O II λ 4649.13/$H\beta$ ratio, T(BJ) and the n_e calculated from CELs. Given that the dependence of O II RLs to the electronic temperature is small, we use the T(BJ) estimated in sec. 3.4.2. The O^{++}/H^{+} ratios obtained are shown in fig. 3.11. The same calculation was made using the temperature from [O III] λ 4363/λ 5007, and the results were similar. We see in fig. 3.11 changes of 1 order of magnitude from the low ACF-low Ω corner to the high ACF-high Ω opposite corner. At ACF larger than 1 dex, the contribution of the MR region becomes important given the low temperature of the region, favoring the emission from RLs.

The determination of O^{++}/H^{+} from RLs is expected to be the representative one in the MR region. We see that this is far from being the case at high ACFs, the highest value obtained for 12 + log(O^{++}/H^{+}) being 9.9 (at $\Omega/4\pi = 0.5$ and ACF(O) = 2.4 dex) while for the MR region it reaches 10.8. This is mainly due to the low contribution to the Hβ emission from the MR component (see sec. 3.4.6).

3.4.5 Comparing ACF(O^{++}) with ADF(O^{++})

The ADF(O^{++}) has been determined using O^{++} abundances determined from CELs and RLs presented in the two previous sections. The result is shown in fig. 3.12. This can be compared to the ACF(O) running on the x-axis. For log ACF(O) > 0.7 the ADF(O^{++}) is smaller than the ACF(O) in the ACF-Ω plane, for the upper right corner the ADF(O^{++}) is 50 times smaller. For all the models of the MR component, the ionic fraction O^{++}/O is always higher than 0.06, so even though we are comparing the ADF(O^{++}) to the ACF(O), this difference can not be completely attributed to the O^{++}/O ratio. The O/H ratio determined from CELs is actually closer to the input values in the *cts* regions. The discrepancy comes from the RLs determination that does not match the "real" value. The main issue of this determination is not the temperature but rather the estimation of the Hβ proportion coming from the O II line emitting region (MR component) as described in the next section.

In fig. 3.13, we compare the difference between the ADF(O^{++}) and the ACF(O^{++}), defined by the ratio of O^{++}/H^{+} integrated over the MR region and O^{++}/H^{+} integrated over the three *cts* regions. This can be seen as the measure of the error one makes when determining the ADF, the ACF being the "true" value of the ionic abundance difference. Whatever the value of Ω, the log(ACF(O)) around 0.8 corresponds to a good determination of the ADF (white solid line in fig. 3.13 indicates log(ADF(O^{++})) = log(ACF(O^{++})). For lower values of the ACF(O), the ADF(O^{++}) overestimates the value of ACF(O^{++}) (by up to 0.7 dex). This corresponds to situations where the contribution to O II coming from the *cts* regions actually dominates the total emission of the O II lines. For values of ACF(O) greater than 0.8 dex, the O II emission mainly comes from the MR region and the ADF(O^{++}) underestimates the true value given by the ACF(O^{++}) by a factor up to $\sim$100 (dark solid line in fig. 3.13).

3.4.6 Contribution of MR to total emission

In figs. 3.14 and 3.15 we show the contribution of some recombination lines (namely for Hβ and the V1 multiplet of O II) emitted by the MR region relative to the total emission. The Hβ emission is mainly coming from the *cts* components, as the *mr* contribution is never higher than 9%. On the other hand, the O II lines are well representative of the MR region when this one is strongly H-poor

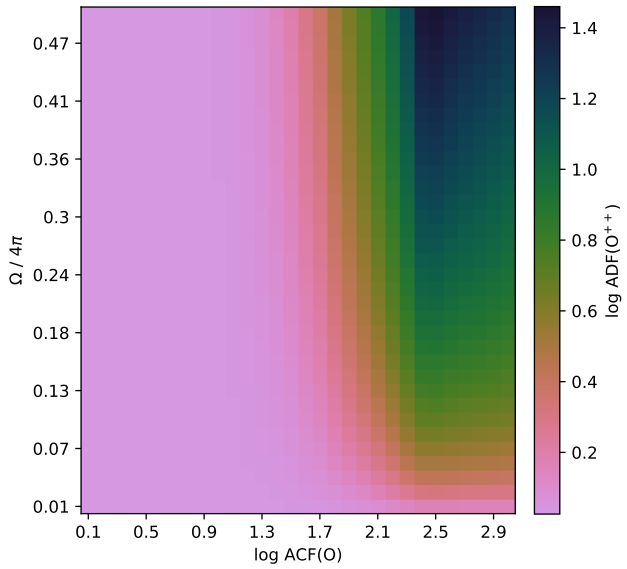

Figure 3.12: Same axis as figure 3.8. The color represents log(ADF(O^{++})) determined for the bi-abundance models.

(ACF(O) > 1.5 dex). The apparent incapacity of the O II/Hβ line ratio to correctly predict the ACF of the nebula (see previous sections) is actually mainly due to the impossibility to only take into account the Hβ emitted by the MR region.

3.5 Fitting the models to observations

The two main observables related to the AD problem are the value of the ADF and Δ T the difference T([O III]) - T(BJ). We determine these parameters for NGC 6153 (with the same method as for our models), namely ADF(O^{++}) = 8.2 (using T(BJ)) and $\Delta T = 3025$ K (using the observations presented in Liu et al. 2000, for the whole nebula), and use them to define an area in the ACF-Ω plane where the models fit these values. This area is shown in fig. 3.16, where the blue (green) color band shows where the models fit ADF(O^{++}) (ΔT resp.) within $\pm$15%. Another way to perform a similar determination is by plotting the observables predicted by the models, as in fig. 3.17. The color code corresponds to the values of ACF (right panel) and $\Omega/4\pi$ (left panel). The diamond corresponds to the observations for NGC 6153. Using a box of $\pm$15% around the observed values, we can extract the models and

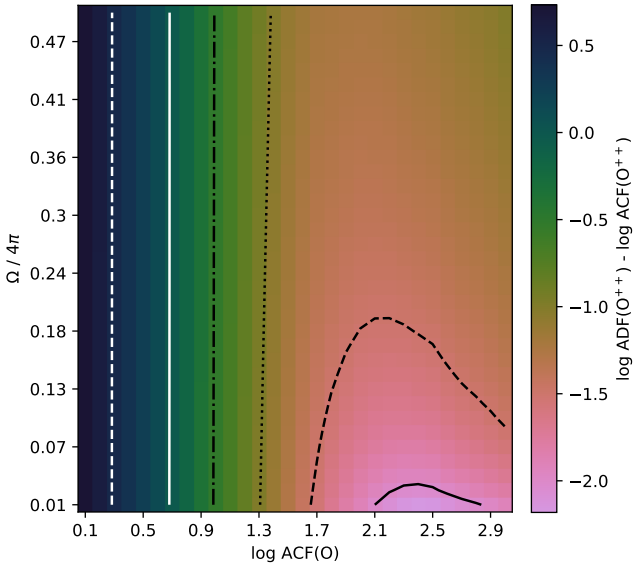

Figure 3.13: Same axis as figure 3.8. The color represents the difference between log(ADF(O^{++})) determined for the bi-abundance models and log(ACF(O^{++})) (actual difference in O^{++} of the MR and the N, BC and S components). White dashed (solid) is for log ADF(O^{++}) - log ACF(O^{++}) equal to 0.5 (0.0) and black dash-dotted, dotted, dashed and solid lines are for: -0.5, -1.0, -1.5, -2.0, respectively.

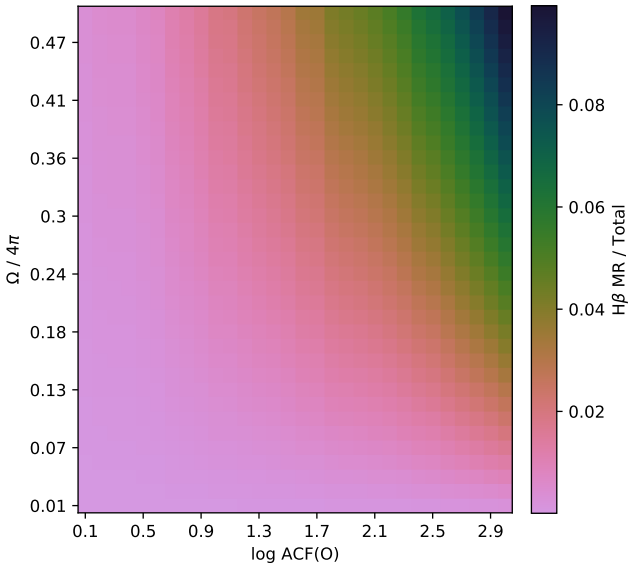

Figure 3.14: Same axis as figure 3.8. The color represents the fraction of the Hβ from the MR to the total emission for the bi-abundance models.

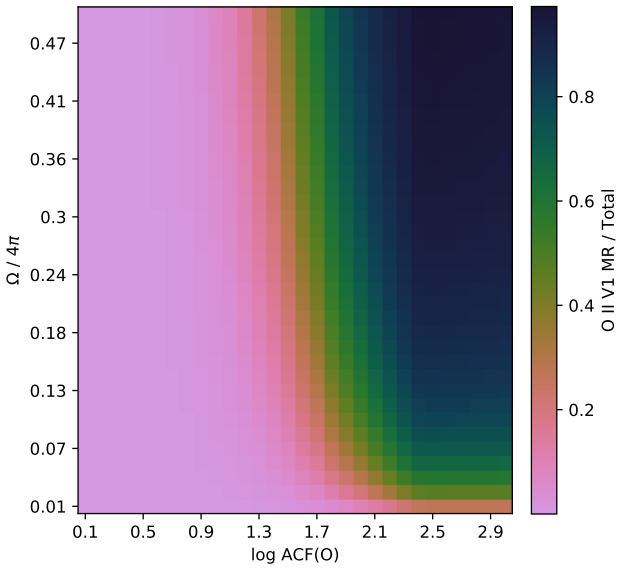

Figure 3.15: Same axis as figure 3.8. The color represents the fraction of the V1 multiplet of O II from the MR to the total emission for the bi-abundance models.

exhibit the values of ACF-Ω combinations that reproduce the observations. This is done in fig. 3.18. Two families of solutions appear around [ACF(O), $\Omega/4\pi$] = [2.1, 0.50] and [2.7, 0.18]. The best solutions correspond to S_1: a lower ACF but high volume for the MR region, and S_2: a higher ACF and smaller volume.

The characteristics of these two solutions are summarized in table 3.4, where T_e, n_e, the ionic fractions of H^+, O^+, O^{++} and O^{+3} and the fractions of volume and mass are given for each one of the 4 components. The electron temperature of the N region is close to 9500 K, while the BC and S components have a slightly lower temperature. The MR region is found to be as cold as 500-600 K. The high value of n_e found in the MR region is due to the contribution of metals to the free electrons. The ionic fractions indicates that the two solutions are very different in the MR - BC - S regions: the S_1 solution almost does not have S region, and the MR and BC regions are mainly O^{++}, while the S_2 solution exhibits a S component and where the MR and BC regions are well recombined to O^+. In both cases, the mass or volume fraction of the MR region relative to the whole nebula is rather small.

One interesting result is that despite the fact that both solutions differs by a factor of ~ 4 in the O/H abundance, the mass of oxygen embedded in the MR region only differs by a factor of ~ 1.5. This indicates that the MR oxygen mass is more robust against the degeneracy than the solutions for ACF(O) and Ω, each one acting in opposite direction. We then determine the O mass in the metal-rich region in NGC 6153 to be 36%-48% of the total one in the nebula, this in a volume that is less than 1%.

We use the solutions S_1 and S_2 to show in fig. 3.19 the contribution coming from each of the 4 regions (in different colors) to the total emission considering a set of 28 representative emission lines. An extensive list of emission lines with the intensity emitted by each region, for both solutions, is given in table 3.5.

We see in fig. 3.19 that the contribution of Hβ coming from the MR region is very small. This is the key problem in the determination of the true metallicity of the MR region, translated in the difference between the ADF (observed) and ACF (real). The important contribution of the MR region coming from the metal recombination lines is clearly seen, as well as from the IR lines. The contribution of the BC and S regions are different in the two solutions.

From the table 3.5 we can see that the total intensities of some lines (last column) change between

Table 3.4: Physical parameters for the four components, for the solutions S_1 and S_2 (this latest in parenthesis).

	N	*MR*	*BC*	*S*
$<T_e>$ [K]	9536 (9536)	629 (527)	8906 (7252)	7117 (7117)
$<n_e>$ [cm^{-3}]	2770 (2770)	3817 (5728)	2738 (2610)	2056 (2056)
12+log(O/H)	8.75 (8.75)	10.85 (11.45)	8.75 (8.75)	8.75 (8.75)
$\Omega/4\pi$*	0.50 (0.80)	0.50 (0.20)	0.50 (0.20)	0.50 (0.20)
H^+/H	0.99 (0.99)	1.00 (1.00)	0.99 (0.96)	0.74 (0.74)
O^+/O	0.06 (0.06)	0.04 (0.70)	0.15 (0.96)	0.46 (0.46)
O^{++}/O	0.86 (0.86)	0.84 (0.28)	0.84 (0.00)	0.26 (0.26)
O^{+3}/O	0.07 (0.07)	0.11 (0.02)	0.00 (0.00)	0.00 (0.00)
O mass (10^{-4}) [$M_\odot$]	6.6 (10.5)	7.5 (12.3)	6.6 (2.0)	0.0 (1.0)
Volume [10^{50}cm^{-3}]	345.1 (554.2)	3.1 (1.3)	345.0 (105.0)	0.5 (51.3)
% mass	49.3 (76.7)	1.4 (1.7)	49.3 (14.5)	0.1 (7.1)

* Fraction of solid angle for each component.

the 2 solutions: the C II (N II) RLs increase by a factor of ∼2.8 (1.7), while the Ne II ones decrease by ∼ 25% between the S_1 and the S_2 solutions. This is mainly due to a change in the ionization of the *MR* region. For the same reason we see a difference in the emission of the IR lines of [N II] and [Ne II]. The other IR lines are from higher charged ions, less affected by the ionization changes in the *MR* regions. The O II RLs are not changing, by construction of our solutions based on fitting the observed ADF(O^{++}). The optical CELs are mainly unchanged between the two solutions.

We use a simplistic relation in the way metals are enhanced in the *MR* region (same ACF for all the metals). The real situation may certainly be more complex and these differences in the C II and N II emission between the two solutions can not be used to derive properties related to the oxygen abundance like ACF(O). Nevertheless, the predicted intensities of C II, O II, and N II in both models are close to the values given by Yuan et al. (2011). This could be seen as an indication that the C:N:O relative abundances used in *MR* region are adequate.

Table 3.5: Line intensities emitted by the four components (N, MR, BC, and S) and the total emission of our modeled bi-abundance nebula, for the S_1 and S_2 solutions (this latest in parenthesis). Values are normalized to Hβ.

* Line intensities obtained using PyNeb (see eq. 3.4).

** The collisional contribution of this line is taken from Cloudy, the recombination contribution is obtained adding the radiative and dielectronic recombination from Pequignot et al. (1991) and Nussbaumer & Storey (1984), respectively (see sec. 3.6) .

Line	N	MR	BC	S	Total
C II 1335.0 Å*	4.8e-3 (7.4e-3)	5.6e-2 (1.9e-1)	5.6e-3 (2.7e-4)	6.3e-8 (8.8e-4)	6.7e-2 (2.e-1)
[N III] 1746.82 Å	2.8e-3 (4.4e-3)	9.9e-8 (9.7e-8)	1.6e-3 (2.9e-8)	—- (3.e-6)	4.5e-3 (4.4e-3)
[N III] 1748.65 Å	5.9e-3 (9.1e-3)	2.2e-6 (2.0e-6)	3.3e-3 (6.e-8)	—- (6.3e-6)	9.2e-3 (9.1e-3)
[N III] 1749.67 Å	3.4e-2 (5.2e-2)	3.9e-6 (3.5e-6)	1.9e-2 (3.5e-7)	—- (3.6e-5)	5.3e-2 (5.2e-2)
[N III] 1750.0 Å	6.8e-2 (1.1e-1)	9.3e-6 (8.5e-6)	3.9e-2 (7.e-7)	—- (7.2e-5)	1.1e-1 (1.1e-1)
[N III] 1752.16 Å	2.e-2 (3.0e-2)	6.7e-7 (6.5e-7)	1.1e-2 (2.e-7)	—- (2.1e-5)	3.1e-2 (3.0e-2)
[N III] 1753.99 Å	6.1e-3 (9.5e-3)	2.4e-6 (2.2e-6)	3.5e-3 (6.2e-8)	—- (6.5e-6)	9.6e-3 (9.5e-3)
C II 1761.0 Å*	1.1e-2 (1.7e-2)	1.2e-1 (3.9e-1)	1.3e-2 (6.1e-4)	1.4e-7 (2.0e-3)	1.4e-1 (4.1e-1)
C III] 1909.0 Å	2.7e-1 (4.2e-1)	2.5e-1 (7.5e-2)	1.7e-1 (7.4e-4)	7.1e-8 (1.0e-3)	6.9e-1 (4.9e-1)
C II 2837.0 Å*	1.8e-3 (2.8e-3)	2.1e-2 (7.1e-2)	2.1e-3 (1.0e-4)	2.4e-8 (3.3e-4)	2.5e-2 (7.4e-2)
Ne II 3218.19 Å*	3.1e-4 (4.8e-4)	4.7e-3 (3.3e-3)	3.2e-4 (—-)	—- (1.2e-5)	5.3e-3 (3.8e-3)
Ne II 3244.09 Å*	2.1e-4 (3.3e-4)	3.2e-3 (2.2e-3)	2.2e-4 (—-)	—- (8.3e-6)	3.6e-3 (2.6e-3)
Ne II 3334.83 Å*	5.0e-4 (7.7e-4)	7.1e-3 (5.e-3)	5.1e-4 (—-)	—- (1.9e-5)	8.1e-3 (5.8e-3)
Ne II 3355.01 Å*	2.6e-4 (4.0e-4)	3.7e-3 (2.6e-3)	2.7e-4 (—-)	—- (1.0e-5)	4.2e-3 (3.0e-3)
Ne II 3360.59 Å*	1.0e-4 (1.6e-4)	1.5e-3 (1.0e-3)	1.1e-4 (—-)	—- (4.e-6)	1.7e-3 (1.2e-3)
Ne II 3367.21 Å*	2.4e-4 (3.7e-4)	3.6e-3 (2.5e-3)	2.4e-4 (—-)	—- (9.3e-6)	4.1e-3 (2.9e-3)
Ne II 3388.41 Å*	1.6e-4 (2.5e-4)	2.5e-3 (1.7e-3)	1.7e-4 (—-)	—- (6.5e-6)	2.8e-3 (2.0e-3)
Ne II 3694.21 Å*	2.5e-4 (3.8e-4)	3.2e-3 (2.2e-3)	2.5e-4 (—-)	—- (9.5e-6)	3.7e-3 (2.6e-3)
Ne II 3709.62 Å*	9.8e-5 (1.5e-4)	1.2e-3 (8.7e-4)	1.0e-4 (—-)	—- (3.7e-6)	1.4e-3 (1.0e-3)
[O II] 3726.03 Å	2.2e-1 (3.3e-1)	—- (—-)	4.3e-1 (1.3e-1)	4.7e-6 (6.6e-2)	6.5e-1 (5.3e-1)
[O II] 3728.81 Å	1.3e-1 (2.0e-1)	—- (—-)	2.6e-1 (8.0e-2)	2.7e-6 (3.8e-2)	3.9e-1 (3.2e-1)
H I 3770.63 Å	1.9e-2 (2.9e-2)	1.7e-3 (1.1e-3)	1.9e-2 (4.4e-3)	3.7e-7 (5.3e-3)	4.e-2 (4.e-2)
Ne II 3777.13 Å*	9.7e-5 (1.5e-4)	1.2e-3 (8.6e-4)	9.9e-5 (—-)	—- (3.7e-6)	1.4e-3 (1.0e-3)
O II 3856.13 Å*	1.2e-5 (1.9e-5)	2.5e-4 (2.1e-4)	1.2e-5 (—-)	—- (1.5e-6)	2.7e-4 (2.3e-4)

Table 3.5: Continues

Line	N	MR	BC	S	Total
[Ne III] 3868.76 Å	4.6e-1 (7.1e-1)	1.8e-4 (7.7e-5)	3.6e-1 (—-)	1.7e-7 (2.4e-3)	8.3e-1 (7.2e-1)
Ne III 3868.8 Å*	5.7e-1 (8.8e-1)	—- (—-)	4.5e-1 (—-)	2.1e-7 (3.e-3)	1.0e+0 (8.8e-1)
O II 3882.19 Å*	6.9e-5 (1.1e-4)	1.3e-3 (1.1e-3)	6.9e-5 (—-)	—- (8.3e-6)	1.5e-3 (1.2e-3)
He I 3888.63 Å	5.2e-2 (8.0e-2)	6.7e-3 (5.4e-3)	5.9e-2 (3.7e-3)	1.0e-6 (1.4e-2)	1.2e-1 (1.0e-1)
O II 3907.45 Å*	3.5e-5 (5.5e-5)	5.7e-4 (4.6e-4)	3.5e-5 (—-)	—- (4.1e-6)	6.4e-4 (5.1e-4)
Ne III 3967.5 Å*	1.7e-1 (2.6e-1)	—- (—-)	1.3e-1 (—-)	6.3e-8 (8.9e-4)	3.0e-1 (2.6e-1)
N II 4041.0 Å	4.7e-4 (7.3e-4)	9.7e-3 (1.7e-2)	5.4e-4 (1.4e-7)	—- (5.e-5)	1.1e-2 (1.8e-2)
N II 4041.31 Å*	1.8e-4 (2.8e-4)	5.1e-3 (9.2e-3)	2.1e-4 (5.3e-8)	—- (1.9e-5)	5.5e-3 (9.5e-3)
[S II] 4068.6 Å	1.3e-2 (2.0e-2)	1.3e-6 (1.0e-5)	1.8e-2 (4.9e-3)	3.9e-7 (5.5e-3)	3.1e-2 (3.0e-2)
O II 4069.88 Å*	4.8e-4 (7.5e-4)	7.2e-3 (5.8e-3)	4.7e-4 (—-)	—- (5.5e-5)	8.2e-3 (6.6e-3)
O II 4072.15 Å*	6.e-4 (9.3e-4)	9.7e-3 (7.9e-3)	5.9e-4 (—-)	—- (7.e-5)	1.1e-2 (8.9e-3)
[S II] 4076.35 Å	4.0e-3 (6.3e-3)	1.9e-7 (1.6e-6)	5.5e-3 (1.5e-3)	1.2e-7 (1.7e-3)	9.5e-3 (9.5e-3)
O II 4078.84 Å*	1.3e-4 (2.e-4)	1.9e-3 (1.5e-3)	1.2e-4 (—-)	—- (1.4e-5)	2.2e-3 (1.7e-3)
O II 4085.11 Å*	1.4e-4 (2.1e-4)	2.1e-3 (1.7e-3)	1.3e-4 (—-)	—- (1.6e-5)	2.3e-3 (1.9e-3)
O II 4087.15 Å*	9.9e-5 (1.5e-4)	2.1e-3 (1.7e-3)	9.9e-5 (—-)	—- (1.2e-5)	2.3e-3 (1.9e-3)
O II 4089.29 Å*	1.9e-4 (3.e-4)	5.6e-3 (4.8e-3)	1.9e-4 (—-)	—- (2.5e-5)	6.0e-3 (5.1e-3)
O II 4092.93 Å*	8.2e-5 (1.3e-4)	1.3e-3 (1.1e-3)	8.1e-5 (—-)	—- (9.5e-6)	1.5e-3 (1.2e-3)
O II 4103.0 Å*	2.4e-5 (3.7e-5)	4.8e-4 (4.1e-4)	2.4e-5 (—-)	—- (2.9e-6)	5.3e-4 (4.5e-4)
O II 4104.99 Å*	1.0e-4 (1.6e-4)	2.2e-3 (1.8e-3)	1.0e-4 (—-)	—- (1.2e-5)	2.4e-3 (2.0e-3)
O II 4110.79 Å*	5.1e-5 (7.8e-5)	1.0e-3 (8.7e-4)	5.0e-5 (—-)	—- (6.1e-6)	1.1e-3 (9.5e-4)
O II 4119.22 Å*	1.8e-4 (2.8e-4)	3.5e-3 (2.9e-3)	1.8e-4 (—-)	—- (2.2e-5)	3.9e-3 (3.2e-3)
O II 4120.28 Å*	1.7e-5 (2.7e-5)	3.1e-4 (2.6e-4)	1.7e-5 (—-)	—- (2.0e-6)	3.5e-4 (2.9e-4)
O II 4120.55 Å*	4.e-5 (6.2e-5)	8.5e-4 (7.2e-4)	3.9e-5 (—-)	—- (4.8e-6)	9.3e-4 (7.8e-4)
O II 4121.46 Å*	7.5e-5 (1.2e-4)	1.3e-3 (1.1e-3)	7.4e-5 (—-)	—- (8.8e-6)	1.5e-3 (1.2e-3)
O II 4132.8 Å*	1.6e-4 (2.5e-4)	2.7e-3 (2.2e-3)	1.6e-4 (—-)	—- (1.9e-5)	3.1e-3 (2.5e-3)
O II 4140.7 Å*	6.0e-6 (9.3e-6)	1.0e-4 (8.2e-5)	5.9e-6 (—-)	—- (7.0e-7)	1.1e-4 (9.2e-5)
O II 4153.3 Å*	2.6e-4 (4.e-4)	4.1e-3 (3.3e-3)	2.5e-4 (—-)	—- (3.e-5)	4.6e-3 (3.7e-3)
O II 4156.53 Å*	3.2e-5 (4.9e-5)	5.3e-4 (4.3e-4)	3.2e-5 (—-)	—- (3.7e-6)	6.e-4 (4.9e-4)
O II 4169.22 Å*	7.4e-5 (1.1e-4)	1.2e-3 (9.6e-4)	7.3e-5 (—-)	—- (8.5e-6)	1.3e-3 (1.1e-3)
C III 4187.0 Å	1.3e-4 (2.0e-4)	2.9e-3 (8.5e-4)	1.1e-5 (—-)	—- (3.1e-8)	3.e-3 (1.1e-3)
O II 4189.79 Å*	2.0e-4 (3.2e-4)	7.5e-5 (6.9e-5)	2.e-4 (—-)	—- (2.1e-5)	4.8e-4 (4.1e-4)

Table 3.5: Continues

Line	N	MR	BC	S	Total
C II 4267.0 Å	1.3e-3 (2.e-3)	2.7e-2 (9.4e-2)	1.5e-3 (7.8e-5)	1.9e-8 (2.6e-4)	3.0e-2 (9.7e-2)
O II 4317.14 Å*	1.4e-4 (2.2e-4)	2.3e-3 (1.9e-3)	1.4e-4 (—-)	—- (1.6e-5)	2.6e-3 (2.1e-3)
O II 4319.63 Å*	8.2e-5 (1.3e-4)	1.3e-3 (1.1e-3)	8.0e-5 (—-)	—- (9.3e-6)	1.5e-3 (1.2e-3)
O II 4325.76 Å*	3.2e-5 (4.9e-5)	5.1e-4 (4.2e-4)	3.1e-5 (—-)	—- (3.6e-6)	5.7e-4 (4.7e-4)
O II 4336.86 Å*	5.9e-5 (9.1e-5)	9.4e-4 (7.8e-4)	5.8e-5 (—-)	—- (6.7e-6)	1.1e-3 (8.7e-4)
H I 4340.46 Å	2.2e-1 (3.4e-1)	2.0e-2 (5.9e-3)	2.3e-1 (5.2e-2)	4.4e-6 (6.2e-2)	4.7e-1 (4.6e-1)
O II 4345.56 Å*	1.8e-4 (2.7e-4)	2.8e-3 (2.3e-3)	1.7e-4 (—-)	—- (2.0e-5)	3.2e-3 (2.6e-3)
O II 4349.43 Å*	2.3e-4 (3.5e-4)	3.7e-3 (3.1e-3)	2.2e-4 (—-)	—- (2.6e-5)	4.2e-3 (3.5e-3)
[O III] 4363.0 Å**	3.2e-2 (4.9e-2)	2.7e-3 (1.0e-3)	1.9e-2 (—-)	—- (1.2e-4)	5.4e-2 (5.0e-2)
O II 4366.89 Å*	1.5e-4 (2.3e-4)	2.4e-3 (2.e-3)	1.5e-4 (—-)	—- (1.7e-5)	2.7e-3 (2.2e-3)
[N III] 4379.0 Å	7.2e-4 (1.1e-3)	2.1e-2 (6.8e-3)	9.e-5 (—-)	—- (1.6e-7)	2.2e-2 (7.9e-3)
O II 4414.9 Å*	1.2e-4 (1.8e-4)	1.5e-3 (1.2e-3)	1.1e-4 (—-)	—- (1.2e-5)	1.7e-3 (1.4e-3)
O II 4416.97 Å*	1.1e-4 (1.7e-4)	1.1e-3 (9.0e-4)	1.1e-4 (—-)	—- (1.1e-5)	1.3e-3 (1.1e-3)
He I 4471.49 Å	2.2e-2 (3.4e-2)	3.5e-3 (2.8e-3)	2.5e-2 (1.7e-3)	4.8e-7 (6.8e-3)	5.e-2 (4.5e-2)
O II 4590.97 Å*	2.1e-4 (3.2e-4)	1.2e-4 (1.1e-4)	2.0e-4 (—-)	—- (2.1e-5)	5.3e-4 (4.5e-4)
N II 4607.16 Å*	7.2e-5 (1.1e-4)	9.2e-4 (1.7e-3)	8.1e-5 (1.9e-8)	—- (6.5e-6)	1.1e-3 (1.8e-3)
N II 4613.87 Å*	4.6e-5 (7.1e-5)	5.8e-4 (1.1e-3)	5.1e-5 (1.2e-8)	—- (4.1e-6)	6.8e-4 (1.1e-3)
N II 4621.39 Å*	7.7e-5 (1.2e-4)	9.4e-4 (1.7e-3)	8.6e-5 (2.e-8)	—- (6.9e-6)	1.1e-3 (1.8e-3)
N II 4630.54 Å*	2.8e-4 (4.3e-4)	3.8e-3 (6.9e-3)	3.1e-4 (7.3e-8)	—- (2.5e-5)	4.4e-3 (7.3e-3)
O II 4638.86 Å*	3.2e-4 (4.9e-4)	4.3e-3 (3.5e-3)	3.1e-4 (—-)	—- (3.5e-5)	4.9e-3 (4.0e-3)
O II 4641.81 Å*	6.4e-4 (9.8e-4)	9.2e-3 (7.5e-3)	6.2e-4 (—-)	—- (7.2e-5)	1.0e-2 (8.6e-3)
N II 4643.09 Å*	9.9e-5 (1.5e-4)	1.3e-3 (2.3e-3)	1.1e-4 (2.6e-8)	—- (8.9e-6)	1.5e-3 (2.4e-3)
O II 4649.13 Å*	7.6e-4 (1.2e-3)	1.3e-2 (1.1e-2)	7.5e-4 (—-)	—- (8.9e-5)	1.5e-2 (1.3e-2)
C III 4650.25 Å	1.8e-4 (2.8e-4)	7.7e-5 (2.9e-5)	7.4e-7 (—-)	—- (2.e-6)	2.6e-4 (3.1e-4)
O II 4650.84 Å*	3.3e-4 (5.2e-4)	4.6e-3 (3.7e-3)	3.3e-4 (—-)	—- (3.7e-5)	5.3e-3 (4.3e-3)
O II 4661.63 Å*	3.5e-4 (5.5e-4)	4.8e-3 (3.9e-3)	3.5e-4 (—-)	—- (3.9e-5)	5.5e-3 (4.5e-3)
O II 4673.73 Å*	5.8e-5 (9.1e-5)	8.1e-4 (6.5e-4)	5.7e-5 (—-)	—- (6.5e-6)	9.2e-4 (7.5e-4)
O II 4676.23 Å*	2.2e-4 (3.4e-4)	3.2e-3 (2.6e-3)	2.2e-4 (—-)	—- (2.5e-5)	3.6e-3 (3.e-3)
He II 4685.64 Å	5.3e-2 (8.1e-2)	1.5e-2 (1.2e-3)	8.4e-5 (—-)	—- (1.5e-6)	6.8e-2 (8.3e-2)
O II 4696.35 Å*	2.6e-5 (4.1e-5)	3.6e-4 (2.9e-4)	2.6e-5 (—-)	—- (2.9e-6)	4.1e-4 (3.4e-4)
O II 4699.22 Å*	1.6e-5 (2.5e-5)	3.e-4 (2.4e-4)	1.6e-5 (—-)	—- (1.9e-6)	3.3e-4 (2.7e-4)

Table 3.5: Continues

Line	N	MR	BC	S	Total
O II 4705.35 Å*	1.7e-5 (2.6e-5)	3.7e-4 (3.1e-4)	1.7e-5 (—-)	—- (2.0e-6)	4.0e-4 (3.4e-4)
[Ar IV] 4711.26 Å	1.5e-2 (2.3e-2)	—- (—-)	5.5e-3 (—-)	—- (2.7e-5)	2.0e-2 (2.3e-2)
[Ar IV] 4740.12 Å	1.1e-2 (1.7e-2)	—- (—-)	4.1e-3 (—-)	—- (2.e-5)	1.5e-2 (1.8e-2)
N II 4779.72 Å*	5.1e-5 (7.9e-5)	8.3e-4 (1.5e-3)	5.8e-5 (1.4e-8)	—- (4.9e-6)	9.4e-4 (1.6e-3)
N II 4788.13 Å*	6.9e-5 (1.1e-4)	1.2e-3 (2.1e-3)	7.8e-5 (1.9e-8)	—- (6.7e-6)	1.3e-3 (2.2e-3)
N II 4803.29 Å*	1.3e-4 (2.0e-4)	2.3e-3 (4.2e-3)	1.5e-4 (3.7e-8)	—- (1.3e-5)	2.6e-3 (4.4e-3)
H I 4861.33 Å	4.7e-1 (7.2e-1)	4.8e-2 (3.1e-2)	4.9e-1 (1.1e-1)	9.5e-6 (1.3e-1)	1.0e+0 (1.0e+0)
O II 4890.86 Å*	2.6e-5 (4.e-5)	4.6e-4 (3.8e-4)	2.5e-5 (—-)	—- (3.0e-6)	5.1e-4 (4.2e-4)
O II 4924.53 Å*	1.3e-4 (2.1e-4)	2.1e-3 (1.7e-3)	1.3e-4 (—-)	—- (1.5e-5)	2.4e-3 (1.9e-3)
O II 4943.0 Å*	8.5e-6 (1.3e-5)	2.e-4 (1.6e-4)	8.4e-6 (—-)	—- (1.0e-6)	2.1e-4 (1.8e-4)
[O III] 4958.91 Å	1.8e+0 (2.8e+0)	9.6e-4 (3.9e-4)	1.4e+0 (—-)	2.7e-6 (3.8e-2)	3.3e+0 (2.8e+0)
[O III] 5006.84 Å	5.4e+0 (8.4e+0)	2.9e-3 (1.2e-3)	4.3e+0 (—-)	8.0e-6 (1.1e-1)	9.7e+0 (8.5e+0)
[Ar III] 5191.82 Å	6.5e-4 (1.0e-3)	—- (—-)	6.2e-4 (9.e-6)	—- (2.0e-5)	1.3e-3 (1.0e-3)
[N I] 5197.9 Å	4.0e-4 (6.3e-4)	1.8e-6 (1.2e-5)	1.6e-3 (8.6e-4)	8.9e-8 (1.3e-3)	2.0e-3 (2.7e-3)
[N I] 5200.26 Å	2.8e-4 (4.3e-4)	2.6e-7 (3.9e-6)	1.1e-3 (6.7e-4)	6.5e-8 (9.1e-4)	1.4e-3 (2.0e-3)
[Cl III] 5517.71 Å	4.4e-3 (6.8e-3)	—- (—-)	4.8e-3 (3.6e-4)	2.1e-8 (2.9e-4)	9.2e-3 (7.5e-3)
[Cl III] 5537.87 Å	5.0e-3 (7.8e-3)	—- (—-)	5.5e-3 (4.1e-4)	2.4e-8 (3.4e-4)	1.0e-2 (8.5e-3)
N II 5666.63 Å*	2.6e-4 (4.0e-4)	3.7e-3 (6.7e-3)	2.9e-4 (6.9e-8)	—- (2.4e-5)	4.3e-3 (7.1e-3)
N II 5676.02 Å*	1.3e-4 (2.0e-4)	1.7e-3 (3.1e-3)	1.5e-4 (3.4e-8)	—- (1.2e-5)	2.0e-3 (3.3e-3)
N II 5679.0 Å	4.4e-4 (6.8e-4)	5.3e-3 (9.4e-3)	4.9e-4 (1.2e-7)	—- (4.1e-5)	6.2e-3 (1.0e-2)
N II 5679.56 Å*	4.7e-4 (7.2e-4)	7.7e-3 (1.4e-2)	5.2e-4 (1.3e-7)	—- (4.4e-5)	8.7e-3 (1.5e-2)
N II 5686.21 Å*	7.7e-5 (1.2e-4)	1.0e-3 (1.8e-3)	8.7e-5 (2.0e-8)	—- (7.0e-6)	1.2e-3 (2.e-3)
N II 5710.77 Å*	9.4e-5 (1.5e-4)	1.3e-3 (2.4e-3)	1.1e-4 (2.5e-8)	—- (8.7e-6)	1.5e-3 (2.5e-3)
[N II] 5755.0 Å	9.3e-3 (1.4e-2)	2.5e-3 (4.2e-3)	1.6e-2 (4.2e-3)	1.6e-7 (2.2e-3)	2.8e-2 (2.5e-2)
He I 5875.64 Å	6.3e-2 (9.7e-2)	1.0e-2 (8.3e-3)	7.2e-2 (5.e-3)	1.4e-6 (2.e-2)	1.4e-1 (1.3e-1)
N II 5927.81 Å*	5.3e-5 (8.1e-5)	8.5e-4 (1.5e-3)	6.e-5 (1.4e-8)	—- (5.1e-6)	9.6e-4 (1.6e-3)
N II 5931.78 Å*	9.4e-5 (1.4e-4)	1.6e-3 (2.8e-3)	1.1e-4 (2.6e-8)	—- (9.1e-6)	1.8e-3 (3.e-3)
N II 5941.65 Å*	1.8e-4 (2.8e-4)	3.2e-3 (5.8e-3)	2.1e-4 (5.1e-8)	—- (1.8e-5)	3.6e-3 (6.1e-3)
N II 5952.39 Å*	2.8e-5 (4.3e-5)	4.7e-4 (8.4e-4)	3.1e-5 (—-)	—- (2.7e-6)	5.3e-4 (8.8e-4)
[O I] 6300.3 Å	1.5e-3 (2.4e-3)	—- (3.7e-7)	6.7e-3 (2.e-3)	1.3e-7 (1.9e-3)	8.2e-3 (6.2e-3)
[S III] 6312.06 Å	1.7e-2 (2.6e-2)	3.9e-7 (1.7e-6)	1.6e-2 (9.0e-4)	3.5e-8 (5.e-4)	3.3e-2 (2.8e-2)

Table 3.5: Continues

Line	N	MR	BC	S	Total
[N II] 6548.05 Å	2.0e-1 (3.1e-1)	2.0e-5 (5.3e-5)	4.1e-1 (2.5e-1)	1.2e-5 (1.7e-1)	6.1e-1 (7.2e-1)
H I 6562.81 Å	1.3e+0 (2.1e+0)	1.8e-1 (5.0e-2)	1.4e+0 (3.3e-1)	2.8e-5 (4.e-1)	2.9e+0 (2.8e+0)
C II 6580.0 Å	1.1e-4 (1.8e-4)	7.6e-4 (2.5e-3)	1.3e-4 (5.6e-6)	—- (1.8e-5)	1.0e-3 (2.7e-3)
[N II] 6583.45 Å	5.9e-1 (9.2e-1)	6.0e-5 (1.6e-4)	1.2e+0 (7.3e-1)	3.5e-5 (4.9e-1)	1.8e+0 (2.1e+0)
He I 6678.15 Å	1.8e-2 (2.7e-2)	3.e-3 (2.4e-3)	2.0e-2 (1.4e-3)	4.0e-7 (5.6e-3)	4.1e-2 (3.7e-2)
[S II] 6716.44 Å	4.0e-2 (6.2e-2)	2.3e-6 (1.2e-5)	5.8e-2 (2.5e-2)	2.1e-6 (2.9e-2)	9.8e-2 (1.2e-1)
[S II] 6730.82 Å	5.8e-2 (8.9e-2)	3.9e-6 (2.1e-5)	8.3e-2 (3.5e-2)	3.1e-6 (4.3e-2)	1.4e-1 (1.7e-1)
He I 7065.22 Å	1.5e-2 (2.3e-2)	1.3e-3 (1.1e-3)	1.6e-2 (8.5e-4)	2.2e-7 (3.1e-3)	3.2e-2 (2.8e-2)
[Ar III] 7135.79 Å	9.1e-2 (1.4e-1)	—- (—-)	1.0e-1 (3.6e-3)	7.6e-7 (1.1e-2)	1.9e-1 (1.6e-1)
C II 7231.0 Å*	1.4e-3 (2.2e-3)	2.2e-2 (7.6e-2)	1.6e-3 (8.1e-5)	1.9e-8 (2.7e-4)	2.5e-2 (7.8e-2)
[O II] 7332.0 Å	9.1e-3 (1.4e-2)	2.5e-3 (2.1e-3)	1.6e-2 (2.6e-3)	8.3e-8 (1.2e-3)	2.8e-2 (2.e-2)
[S III] 9068.62 Å	3.0e-1 (4.7e-1)	1.2e-6 (4.0e-6)	3.3e-1 (3.9e-2)	2.0e-6 (2.9e-2)	6.3e-1 (5.3e-1)
[S III] 9530.62 Å	7.6e-1 (1.2e+0)	3.1e-6 (1.0e-5)	8.2e-1 (9.7e-2)	5.1e-6 (7.2e-2)	1.6e+0 (1.3e+0)
[C I] 9850.26 Å	4.9e-4 (7.5e-4)	—- (4.8e-8)	8.7e-4 (4.e-4)	1.3e-7 (1.9e-3)	1.4e-3 (3.0e-3)
He I 10830.3 Å	3.6e-1 (5.6e-1)	3.1e-2 (2.9e-2)	3.9e-1 (2.0e-2)	5.1e-6 (7.2e-2)	7.9e-1 (6.8e-1)
[Ar III] 9.0 μm	8.8e-2 (1.4e-1)	4.4e-2 (1.1e-1)	1.1e-1 (6.7e-3)	1.8e-6 (2.5e-2)	2.4e-1 (2.8e-1)
[S IV] 10.5 μm	9.7e-1 (1.5e+0)	8.2e-1 (2.6e-1)	5.5e-1 (—-)	2.6e-7 (3.7e-3)	2.3e+0 (1.8e+0)
[N II] 12.2 μm	2.5e-3 (3.9e-3)	7.5e-4 (1.8e-2)	5.6e-3 (4.5e-3)	3.7e-7 (5.3e-3)	8.9e-3 (3.1e-2)
[Ne II] 12.8 μm	2.2e-2 (3.4e-2)	4.4e-2 (8.6e-1)	6.3e-2 (1.2e-1)	9.0e-6 (1.3e-1)	1.3e-1 (1.1e+0)
[Ne III] 15.6 μm	8.3e-1 (1.3e+0)	1.1e+0 (7.4e-1)	8.3e-1 (—-)	1.9e-6 (2.7e-2)	2.8e+0 (2.1e+0)
[S III] 18.7 μm	3.7e-1 (5.7e-1)	2.9e-1 (5.5e-1)	4.3e-1 (7.5e-2)	4.9e-6 (6.9e-2)	1.1e+0 (1.3e+0)
[Ar III] 21.8 μm	5.6e-3 (8.7e-3)	8.8e-4 (1.7e-3)	6.9e-3 (4.1e-4)	1.1e-7 (1.5e-3)	1.3e-2 (1.2e-2)
[O IV] 25.9 μm	5.e-1 (7.7e-1)	7.7e-1 (2.2e-1)	2.9e-4 (—-)	—- (1.3e-8)	1.3e+0 (9.9e-1)
[S III] 33.5 μm	1.5e-1 (2.3e-1)	1.4e-1 (2.5e-1)	1.7e-1 (2.5e-2)	1.9e-6 (2.7e-2)	4.6e-1 (5.3e-1)
[Ne III] 36.0 μm	7.4e-2 (1.1e-1)	5.2e-2 (3.3e-2)	7.4e-2 (—-)	1.6e-7 (2.3e-3)	2.e-1 (1.5e-1)
[O III] 51.8 μm	7.9e-1 (1.2e+0)	6.e-1 (2.7e-1)	5.9e-1 (—-)	5.e-6 (7.0e-2)	2.e+0 (1.6e+0)
[N III] 57.3 μm	3.5e-1 (5.3e-1)	2.9e-1 (2.1e-1)	3.1e-1 (6.5e-5)	1.7e-6 (2.5e-2)	9.5e-1 (7.6e-1)
[O III] 88.3 μm	1.7e-1 (2.6e-1)	1.2e-1 (4.9e-2)	1.1e-1 (—-)	1.0e-6 (1.4e-2)	4.0e-1 (3.2e-1)

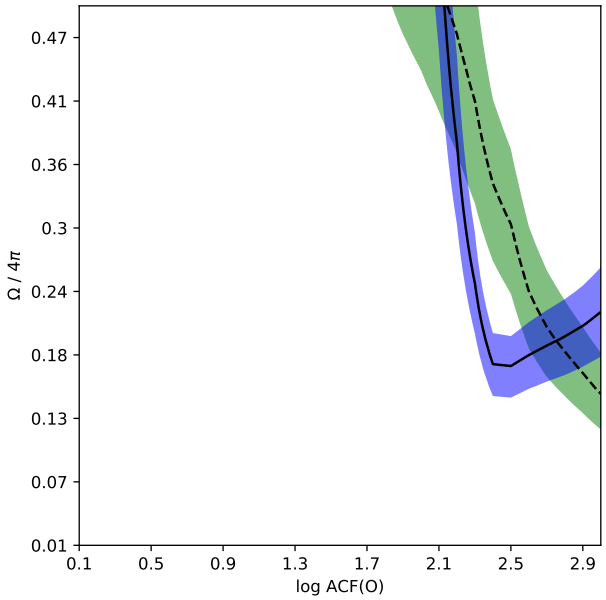

Figure 3.16: Same axis as figure 3.8. The solid black line represents the bi-abundance models where the estimation of ΔT = T([O III]) - T(BJ) is equal to 3025 K (which is the ΔT for NGC 6153 we estimate based on the observations from Liu et al. 2000), the blue region is for ±15% this value. Similarly, the dashed black line is for the bi-abundance models with ADF(O^{++}) equal to 8.2 (which is the value we estimate for NGC 6153 from the observations of Liu et al. 2000), the green region is for ±15% this value.

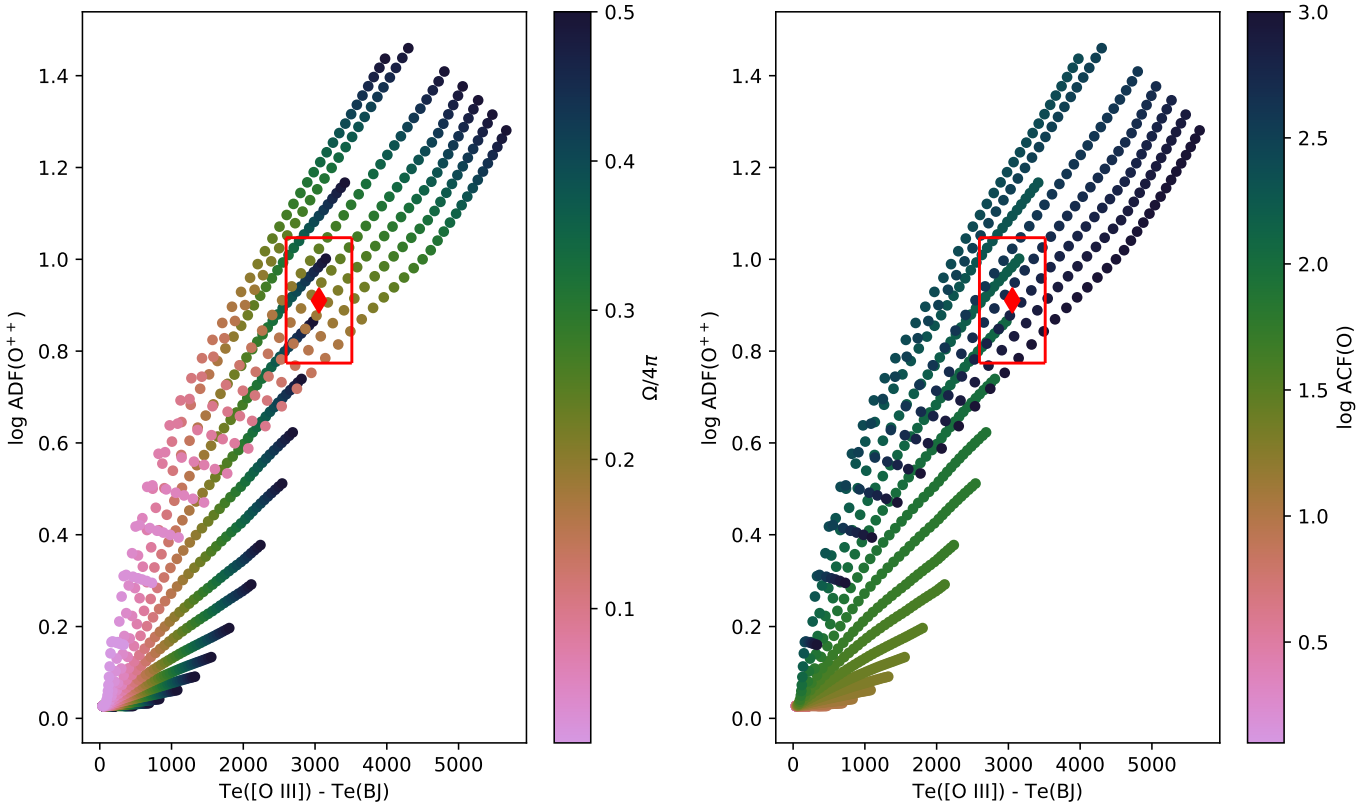

Figure 3.17: The x-axis shows the difference in temperature estimated with: [O III] λ 4363/λ 5007 and the Balmer jump. The y-axis shows the log(ADF(O^{++})) estimated for the bi-abundance models. The red diamond represents the value for the PN NGC 6153 taken from Liu et al. (2000) (for the minor axis in the case of Te(BJ) and for the whole nebula in the case of Te([O III]) and ADF(O^{++})). The red square represents the region selected for the models that are closer to the observed value in NGC 6153. Left panel: color represents the normalized solid angle of the metal-rich clumps (and the gas behind the clumps and the corresponding shadow), in the range of 0.01 to 0.50. Right panel: color represents the variations in the ACF(O) (see eq. 3.2) and goes from 0.1 to 3.0 dex for the bi-abundance models.

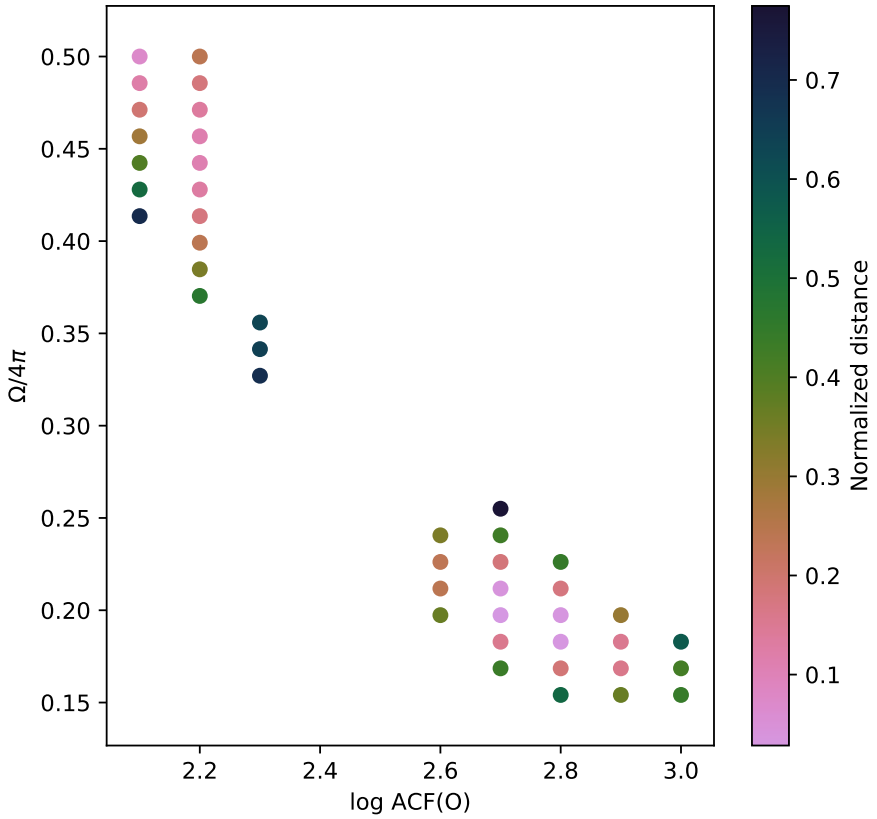

Figure 3.18: Selected models from inside the red square of figure 3.17. The color represents the distance to the observed value shown as a red diamond in fig 3.17. The distance ($\sqrt{(x/x_0)^2 + (y/y_0)^2}$, where x = T([O III]) - T(BJ), y = ADF(O^{++})) is normalized through x_0 and y_0 so the distance from the centre of the square to a corner is 1.

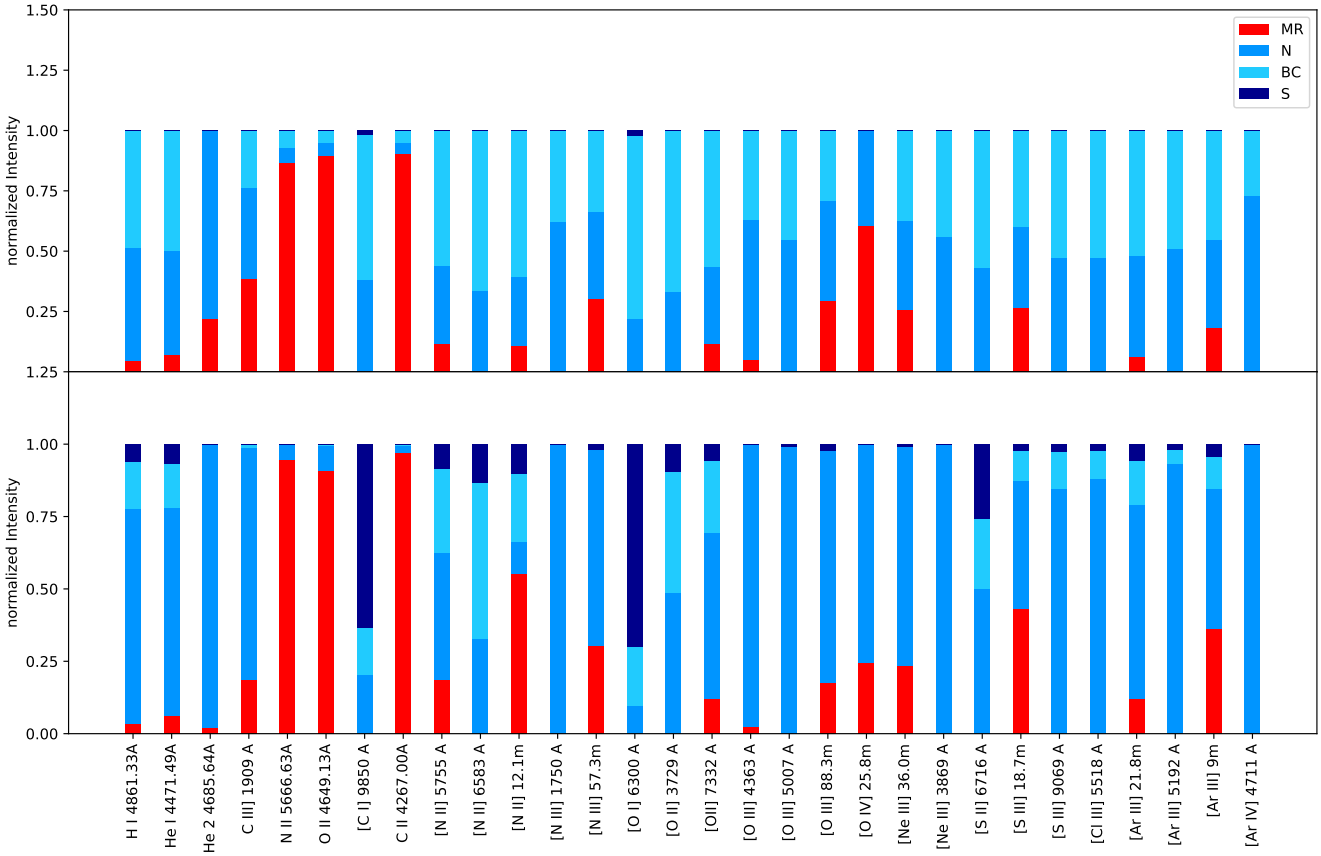

Figure 3.19: Normalized intensity of RLs and CELs showing the contribution of the four components of the bi-abundance models (see sec. 3.3.5). In the labels for the emission lines, 'A' stands for Å, and 'm' for μm. Top panel represents the S_1 solution (log ACF(O) = 2.1, and $\Omega/4\pi = 0.50$), and bottom panel the S_2 solution (log ACF(O) = 2.7, and $\Omega/4\pi = 0.18$). The two solutions are selected from the two families of solutions shown in figure 3.18.

3.5.1 Dust

In table 3.6, we compare the IR emission predicted in the two solutions of the models with the values observed by Helou & Walker (1988) for NGC 6153 in the 4 IRAS bands at 12, 25, 60 and 100 μm. We can see that in both solutions the IR emission from the model is very close to the observed emission. For the S_1, the IR band fluxes are well reproduced. For the S_2, the model gives values higher than the observed fluxes at 12, 25, and 60 μm, and a good fit for 100 μm. The emission at the shorter wavelengths bands is already higher than what is observed. Adding dust to the MR component will increase the emission in this range. Thus there is no evidence of the presence of dust in the MR region, thus we do not include dust in this MR component. This result agrees with what Ercolano et al. (2003b) found for the polar knots of Abell 30, but is in contradiction with what Borkowski et al. (1994) found in the case of the equatorial H-poor ring of the same object. The interpretation of this lack of dust in the metal rich region, in terms of creation and destruction of dust, is not explored in this work, nonetheless, the extreme opposite case where all the dust is in the MR component is discussed here. In Richer et al. (2019) it is mentioned that way to notice if there is a large amount of dust in the metal-rich component is to search for an enhanced extinction in H I and He I towards that component, in the case of PN NGC 7009 they found no enhanced extinction for the additional plasma component (mainly responsible of O II lines) and imply the additional component has a small amount of dust.

The creation and destruction of dust in the MR component is unknown, and due to the lack of spatially resolved IR observations, we cannot constrain the radial distribution of dust. We have assumed that no dust is in the MR component, and all the dust necessary to reproduce the IRAS observations is located in the *cts* components. Here we explore the opposite case where the dust is only present in the MR component, although the reality may be an intermediate solution between both hypotheses. We generate grids of models including dust composed of graphite and silicate grains of only two sizes: 1 μm and 0.01μm, we search for the D/G values that have the closest fit to the IRAS observations. We define the D/G for each model to be proportional to the O/H of the MR component. We follow the same procedure searching for solutions that reproduce ΔT and the ACF(O^{++}), like in the figures 3.17 and 3.18. In these models, at some point when the ACF increases the dust becomes optically thick (ACF $>$ 2.7 dex) and the gas behind the clumps is no longer ionized by the star, becoming a shadow ionized by the Lyman continuum radiation from the N component. The solution at "lower" ACF and higher $\Omega/4\pi$ is lost, and only one solution with ACF = 2.7 dex and $\Omega/4\pi = 0.27$, marginally reproduces simultaneously ΔT and ADF(O^{++}). For this solution the IR emission at 12, 25, 60 and 100 μm is 10.2, 44.6, 134.8 and 71.4 Jy, close to the observed values (see tab. 3.6) and the D/G by mass is 1.04, which is considerably higher than the canonical value in the ISM of

Table 3.6: Emission from IRAS bands for PN NGC 6153 (Helou & Walker 1988) and the two solutions S_1 and S_2 in Jansky units.

Wavelength	Observations	S_1	S_2
12 μm	6.9	7.2	10.3
25 μm	52.1	72.8	107.0
60 μm	120.0	127.7	173.6
100 μm	52.1	40.3	52.0

6.3×10^{-3}. The abundances of the elements trapped in the dust (in log, by number) are: C = -1.21, O = -0.4, Mg = Si = Fe = -1.0. These abundances in dusty phase are even higher than the corresponding abundances in the gaseous phase for Mg, Si and Fe, for O is roughly the same amount and for C is about 30% of the gaseous phase. A more detailed modeling of the distribution of dust could be of interest as further work, but additional observations are needed to constrain the free parameters.

3.5.2 Density and size of the MR component

The models described in the previous sections were computed focusing on the changes of the metallicity and the volume contribution of the MR components (to study their effects on the AD). In these models the density, the distance to the star and the radial size of the MR component, were fixed to certain values (based on the observations of surface brightness presented in Y11).

The electron density of the MR region is hard to constrain with observations: recombination lines (the only ones emitted by this cold region) have quite low dependency on the density. There is no indication that a pressure equilibrium must exist between the warm and the cold regions, as they are not supposed to be in contact. We adopted then the same hydrogen density as for the *cts* regions. Increasing for example the density of the MR region would increase its optical depth, decreasing its global ionization and possibly leading to a vanishing of the BC region, replaced by a pure shadow region.

The effect of changing the radial size of the MR region, decreasing for example its inner radius, would lead to a very similar effect: increasing its optical depth.

In both cases, the global emission of the MR region, for a given Ω, will increase. To recover the same ADF and ΔT, a lower ACF will be needed for a given Ω.

We performed test cases to explore the effect of changing the hydrogen density and the inner radius of the MR component. In a first test, we explore the density range from $1{\times}10^3$ cm^{-3} to $4{\times}10^3$ cm^{-3}. At lower densities the models fitting the observed ADF(O^{++}) and ΔT, as shown in fig. 3.17, have higher Ω eventually reaching impossible values higher than 1. On the other hand, at higher densities no solution is found that reproduces simultaneously the ADF(O^{++}) and ΔT.

The other test varying the inner radius between 4.3 arcsec and 4.7 arcsec, leads to a similar behaviour. A smaller inner radius needs a smaller Ω to fit the two observables.

These tests show that the main result obtained in the previous section is still valid when changing some of the parameters we fixed *a priori* in our grid of models: the ACF (the real metal enhancement of the rich region) is higher than the ADF determined from observations.

From the exploration of this grid, we determine the mass of oxygen embedded in the metal rich clumps to be between 25% and 60% of the total mass of oxygen in the nebula.

Another limitation of our study is the description of the BC and S regions. The very simplistic model presented here assumes a very sharp separation between the N region and what is happening behind the MR region. Some observations exhibit cometary tails (see e.g. O'Dell et al. 2005, in the Helix nebula) that are very aligned in the direction of the central star. On the other side, the image of NGC 6153 does not show clear evidences of this kind of structure.

3.5.3 Ionization correction factor for the MR region

The results presented in this work are about the ADF(O^{++}). If one is interested in the ADF(O), an Ionization Correction Factor (ICF) needs to be applied. Even in the case of a low ionization nebula where only O^+ and O^{++} are present, these ionic abundances are determined from the [O II] and [O III] lines that are mainly emitted by the *cts* regions. For the MR region where only O^{++} is observed through the O II lines, the ICF(O^{++}) needs to be used. Observations of oxygen recombination lines at other ionization stages are necessary to estimate the total oxygen abundance based upon recombination lines. In many cases, when these observations are not available, the ICF(O^{++}) derived from forbidden lines is used. In the two metallicities scenario, this can lead to larger errors in the determination of the total oxygen abundance based upon recombination lines. From table 3.4, we see that the ICF(O^{++}) - which is O/O^{++} - is almost the same for the N, MR and BC regions in the S_1 solution (between 1.1 and 1.2). But in the case of the S_2 solution, the ICF(O^{++}) for the *cts* regions is close to 1.1, while the ICF(O^{++}) that needs to be applied to O^{++} in the MR region is 3.6.

If the density of the MR region, or its radial size, is changed, the ionization of the region will change, as well as the ICF(O^{++}).

The He II 4686 emission is classically used to determine the ICF(O^{++}) taking into account the presence of O^{+3} (Delgado-Inglada et al. 2014a). But we see that, in the case of the S_1 solution, 20% of the intensity of this line comes from the MR region and should be removed before computing the ICF.

So, for abundance discrepancies that are due to multiple plasma components, the total abundances can be very uncertain when the ADF is large.

3.5.4 He in MR component

The material that is supposed to be responsible for the observed high ADF (> 10) in some PNe has unusual properties, very different from the standard ISM. It is very hard to observe as it is blended with "normal" PN gas in the observations. It mainly emits metal RLs, and partially the H I lines. The contribution from this component to the total He RLs is almost negligible (as well as in the case of H I lines), and barely distinguishable from the "normal" component emission. The exact He abundance in this MR component is then very hard to determine. On the other hand, the fact that this component is cold points to a small heating and strong cooling.

We also explore an extreme case where the MR region is only H-poor and where helium is enhanced in the same way as the metals. We found that no solution can be determined in the ADF(O^{++}) vs ΔT observable space, as shown in fig. 3.20. A value of T([O III]) - Te(BJ) as high as the observed one can be obtained, but no high value for the ADF(O^{++}) can be reached (the maximum reached by the models is 5, while the observation is 8) . This is mainly due to the fact that the MR region does not emit anymore the O II recombination lines: in the inner part of the MR region, where He is ionized (once or twice), the electron temperature is rather high due to the heating from He ionizations (around 5,000K) and the recombination of O^{++} is strongly reduced. In the outer part of the MR region, He is recombined and does not heat anymore the gas, there is no photons anymore to ionize O^{+} into O^{++}, and no O II RLs can be produced. Nevertheless this cold region emits some continuum, leading to a low value for Te(BJ) and finally to the observed value of T([O III]) - Te(BJ).

To find how much the He/H abundance can increase in the MR component, we computed other sets of models where the He abundances is only enhanced by a fraction of the metal enhancement. We found that the maximal value for He/H that still leads to a marginal S_3 solution that reproduces the observed ADF(O^{++}) and ΔT is: He/H = 6.3 (no solution is found for He/H higher than 6.3). The solution we obtain

in this case corresponds to log(ACF) = 2.1 and $\Omega/4\pi = 0.5$. The corresponding plot is shown in fig. 3.21. Intensities of He lines for this S_3 solution are presented in table 3.7, as well as those obtained in the S_1 and S_2 solutions presented in sec. 3.5 and the observation from Yuan et al. (2011). We can see that for this high He content solution, the predictions of the He I lines are more or less 4 times higher than for the S_1 and S_2 solutions and are above the observed values. Regarding the He II line, this S_3 solution is closer to the observation than the S_1 or S_2 values. In table 3.8 we present the physical parameters and ionic fractions for the S_3 solution. We see that the oxygen mass of the MR component in the S_3 solution is 35% of the total oxygen mass. We also notice that in the S_3 solution the electronic temperature (density) in the MR region is about 4.5 (3.5) times higher than for the S_1 and S_2 solutions. We can conclude that He/H in the MR region is not well constrained by the model, being between 0.1 and 6, whereas the enhancement in metals is of order of 125 for the S_3 solution. This result is similar to that of Yuan et al. (2011), where the He abundance is less enhanced than metals in their metal rich region (He/H (MR/NR) $\simeq$ 5, while O/H (MR/NR) $\simeq$ 80, from their Tab. 2.). We should also keep in mind that the ionizing SED used in our models is a simple Planck function, adopting a more detailed atmosphere model being out of the scope of this work.

On the other hand, in the case of the model of Abell 30 presented by Ercolano et al. (2003b), the He/H abundance reaches a value as high as 40, while O/H$\simeq$1. Here we obtain lower values for O/H (between 0.07 and 0.35) and for He/H (lower than 6.3). Therefore, the process leading to the H-poor components in these two object seems to be different.

Finally, considering the abundances determined in some novae shells (nova event is not excluded by Wesson et al. (2018) as a proxy for a scenario to these H-poor clumps), one can see that the strong enhancement determined for the CNO elements is not associated to an equivalent enhancement in helium (see e.g. Morisset & Pequignot 1996). The conclusion of this section is that the ACF(He) is distinct from the ACFs of the metals, and needs a special and dedicated treatment.

3.6 Paper 2: recombination contribution to auroral lines

In this section we present the paper titled: "The impact of strong recombination on temperature determination in planetary nebulae", published by Gómez-Llanos et al. (2020) in the Monthly Notices of Royal Astronomical Society.

For the models described in sec. 3.3, the recombination contribution to the auroral lines for [N II] λ 5755 is taken from Cloudy based on the calculations by Nussbaumer & Storey (1984), for [O II] λ 7332 from Cloudy based on Liu et al. (2001a), and for [O III] λ 4363 from Cloudy (version 17.02) using Pequignot et al. (1991)

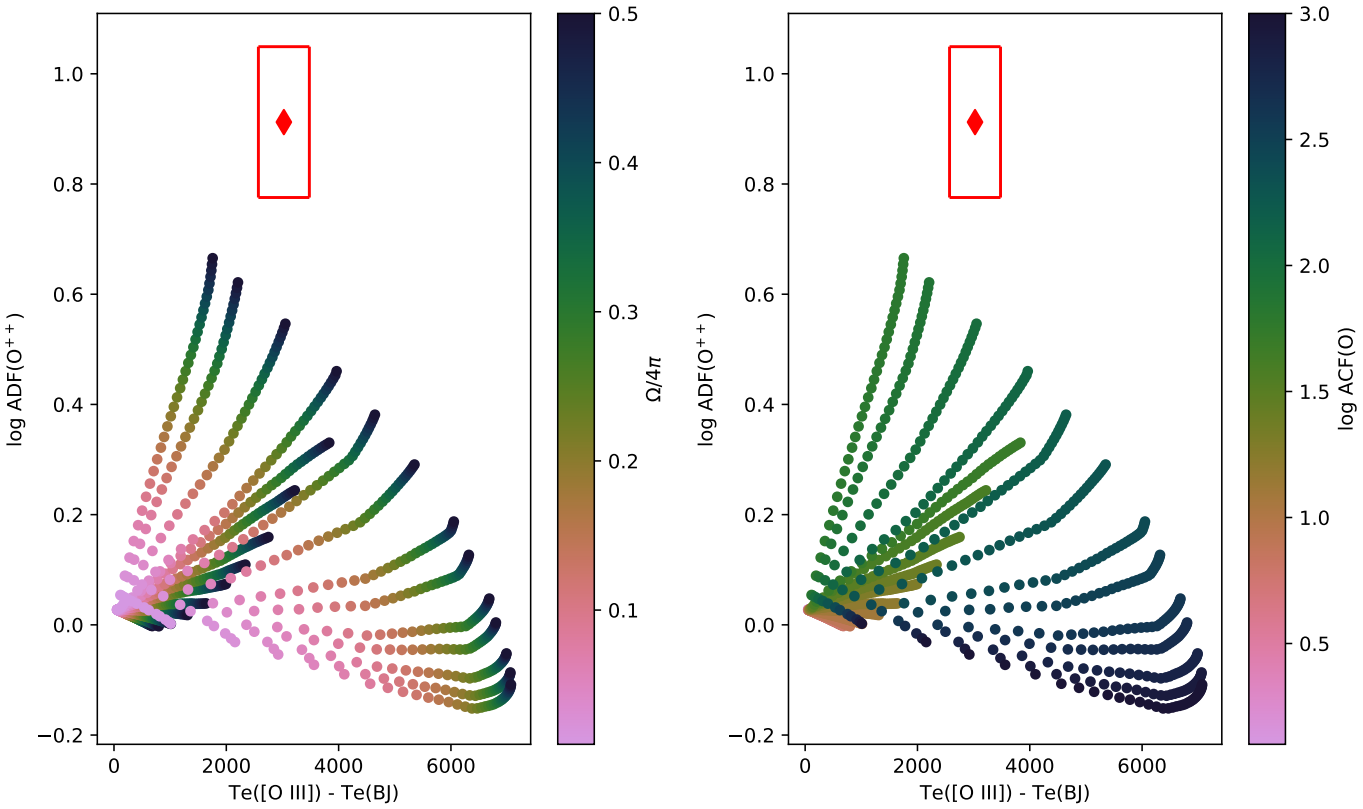

Figure 3.20: Relation between ADF(O^{++}) and T([O III]) - Te(BJ) for a sample of models where the helium in the MR component is enhanced in the same way as the metals.

Table 3.7: Emission line intensities of He lines for the solution S3 with He/H = 6.3, log ACF = 2.1, and $\Omega/4\pi = 0.5$. The observations for PN NGC 6153 from Yuan et al. (2011) and the line intensities obtained in the S1 and S2 solutions.

Line	S1	S2	S3	Observation
He I 4471.49	5.0e-02	4.5e-02	1.9e-01	6.5e-02
He I 5875.64	1.4e-01	1.3e-01	5.7e-01	1.9e-01
He I 6678.15	4.1e-02	3.7e-02	1.6e-01	4.8e-02
He I 7065.22	3.2e-02	2.8e-02	8.4e-02	4.3e-02
He II 4685.64	6.8e-02	8.2e-02	1.0e-01	1.3e-01

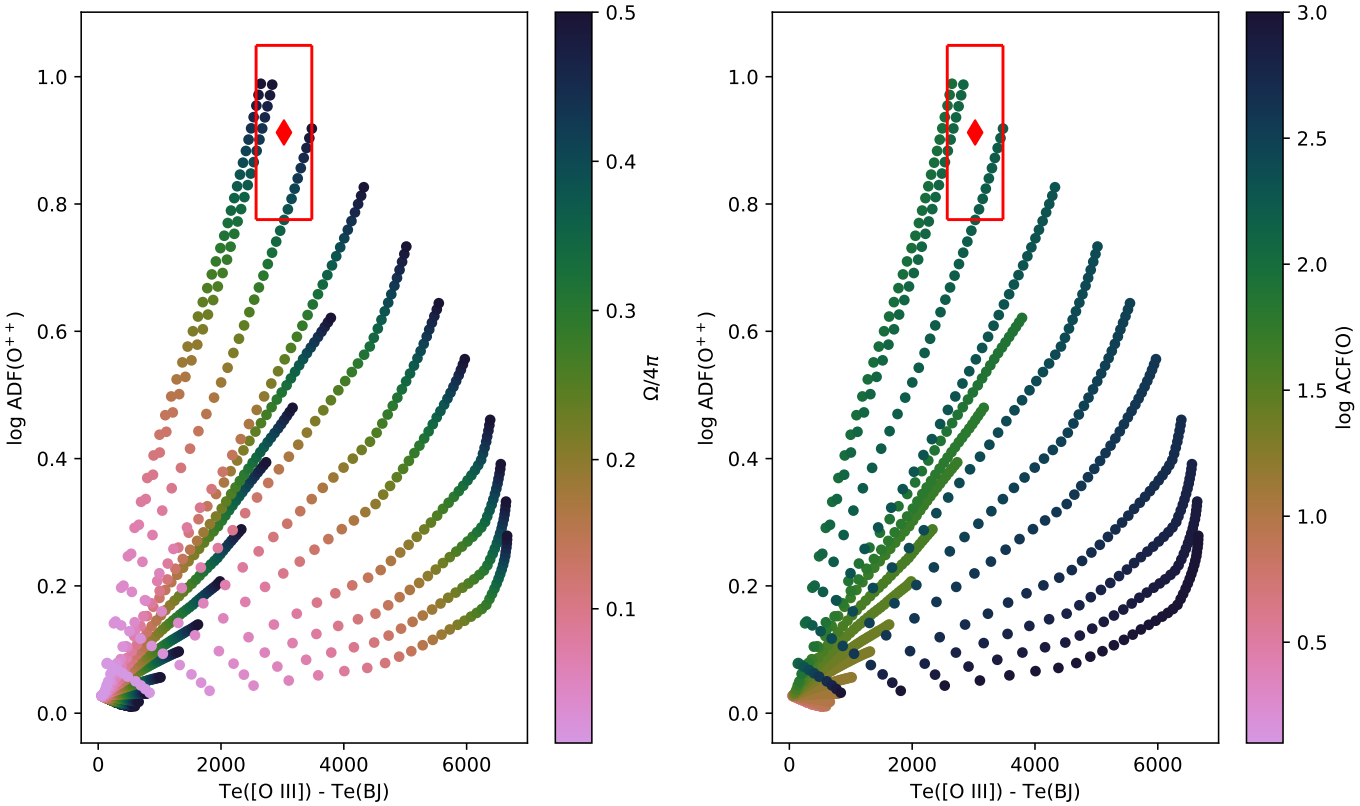

Figure 3.21: Relation between ADF(O^{++}) and T([O III]) - Te(BJ) for a sample of models where the helium in the MR component is enhanced following this relation: He/H_{MR} = He/H_N x 0.5 (1 + ACF(O)).

Table 3.8: Physical parameters for the four components, for the solution S_3.

	N	MR	BC	S
$<T_e>$ [K]	9653	2826	6913	6539
$<n_e>$ [cm^{-3}]	2767	15570	2412	2670
12+log(O/H)	8.75	10.85	8.75	8.75
$\Omega/4\pi$*	0.50	0.50	0.50	0.50
H^+/H	0.99	1.00	0.96	0.97
O^+/O	0.08	0.36	0.96	0.66
O^{++}/O	0.85	0.64	0.00	0.31
O^{+3}/O	0.07	0.01	0.00	0.00
O mass (10^{-4}) [$M_\odot$]	6.6	7.5	5.8	1.2
Volume [10^{50}cm^{-3}]	345	3.2	306.3	64.2
% mass	44.2	8.3	39.3	8.2

* Fraction of solid angle for each component.

and Nussbaumer & Storey (1984). We see in fig. 3.19 that the contribution of the MR component to the intensity of the auroral lines [N II] λ 5755 and [O II] λ 7332 emission is not negligible. This is due to the recombination of N^{++} and O^{++}, favored by the low temperature of the MR region. In the grid we explored, the most important contributions reach 1/3 of the total auroral emission, for a model with an ADF(O^{++}) of ∼30. In case of more extreme ADFs, the recombination contribution may even be dominant. In case of higher excitation nebula the recombination of [O III] λ 4363 may become significant. This is in total agreement with observations of NGC 6778 from Jones et al. (2016) and García-Rojas et al. (2016) who found the spatial location of the [O III] λ 4363 emission coincides with the O^{++} recombination lines and not with the [O III] λ 5007 emission. This effect can be amplified when the observation is obtained in the direction of the metal rich region rather than for the whole nebula, which is the case in high spatial resolution observations. Without taking the recombination contribution into account, one can determine a gradient of temperature increasing toward the central part of the nebula, where the MR regions are located. On the contrary, the increase of [O III] λ 4363 emission is actually related to a very strong decrease of the electron temperature! We explore the recombination contribution to [O III] λ 4363 in the paper by Gómez-Llanos et al. (2020) that is presented below. In this work, we use observations of two PNe: Abell 46 and NGC 6778, with an estimated ADF(O^{++}) of 120 and 18, respectively. To estimate the recombination contribution to the [O III] λ 4363 line, we remove the collisional contribution, assuming it follows the same radial distribution

than the emission line [O III] λ 4959. We find that the contribution of recombination to the total [O III] λ 4363 emission, can be up to 70% and 40%, in Abell 46 and NGC 6778, respectively.

Monthly Notices
of the
ROYAL ASTRONOMICAL SOCIETY

MNRAS **498,** L82–L86 (2020)
Advance Access publication 2020 July 21

doi:10.1093/mnrasl/slaa131

The impact of strong recombination on temperature determination in planetary nebulae

V. Gómez-Llanos [1]★ C. Morisset,[1]★ J. García-Rojas [2,3]★ D. Jones [3] R. Wesson,[4] R. L. M. Corradi[3,5] and H. M. J. Boffin [6]

[1]*Instituto de Astronomia (IA), Universidad Nacional Autónoma de México, Apdo. postal 106, C.P. 22800 Ensenada, Baja California, México*
[2]*Instituto de Astrofísica de Canarias, E-38200 La Laguna, Tenerife, Spain*
[3]*Departamento de Astrofísica, Universidad de La Laguna, E-38206 La Laguna, Tenerife, Spain*
[4]*Department of Physics and Astronomy, University College London, Gower St, London WC1E 6BT, UK*
[5]*GRANTECAN, Cuesta de San José s/n, E-38712 Breña Baja, La Palma, Spain*
[6]*European Southern Observatory, Karl-Schwarzschild-Str 2, D-85748 Garching bei Muenchen, Germany*

Accepted 2020 July 6. Received 2020 June 25; in original form 2020 June 5

ABSTRACT

The long-standing difference in chemical abundances determined from optical recombination lines and collisionally excited lines raises questions about our understanding of atomic physics, as well as the assumptions made when determining physical conditions and chemical abundances in astrophysical nebulae. Here, we study the recombination contribution of [O III] 4363 and the validity of the line ratio [O III] 4363/4959 as a temperature diagnostic in planetary nebulae with a high abundance discrepancy. We derive a fit for the recombination coefficient of [O III] 4363 that takes into account the radiative and dielectronic recombinations, for electron temperatures from 200 to 30 000 K. We estimate the recombination contribution of [O III] 4363 for the planetary nebulae Abell 46 and NGC 6778 by subtracting the collisional contribution from the total observed flux. We find that the spatial distribution for the estimated recombination contribution in [O III] 4363 follows that of the O II 4649 recombination line, both peaking in the central regions of the nebula, especially in the case of Abell 46 that has a much higher abundance discrepancy. The estimated recombination contribution reaches up to 70 and 40 per cent of the total [O III] 4363 observed flux, for Abell 46 and NGC 6778, respectively.

Key words: atomic data – stars: AGB and post-AGB – ISM: abundances – planetary nebulae: individual: Abell 46, NGC 6778.

1 INTRODUCTION

When measuring chemical abundances from faint heavy-element optical recombination lines (ORLs), it is found that they are always greater than those measured from the much brighter collisionally excited lines (CELs). Being known for more than 70 yr, this *abundance discrepancy problem* is probably the most important challenge to our understanding of the physics of photoionized nebulae (see García-Rojas et al. 2019, and references therein). Several scenarios have been proposed to resolve the issue, the two most popular being (i) the existence of temperature fluctuations within a chemically homogeneous plasma (Peimbert 1967; Torres-Peimbert, Peimbert & Daltabuit 1980) and (ii) the presence of cold, metal-rich gaseous clumps in the nebula, which are very efficiently cooled by the heavy elements (Liu et al. 2000).

However, neither of these scenarios seems appropriate to universally explain the complete range of abundance discrepancy factors (ADFs, i.e. the ratio between the abundances determined from ORLs and CELs) observed in both H II regions and planetary nebulae (PNe; see Wesson et al. 2018).[1] Moreover, the mechanisms producing, and allowing for the survival of, temperature fluctuations in a photoionized plasma are still under debate (Peimbert, Peimbert & Delgado-Inglada 2017), while the same is true for the physical origin of the metal-rich component (Stasińska et al. 2007; Corradi et al. 2015). Nevertheless, some observational evidence of the existence of two or more gaseous phases in PNe has been found by several authors in recent years (Wesson, Liu & Barlow 2003; Liu et al. 2006; Wesson et al. 2008; Richer et al. 2013, 2017; Peña et al. 2017).

In particular, PNe with ADFs >10 have proven to be very interesting objects, as their extreme ADFs seem to be linked with the evolution of a central close-binary system that has experienced a common envelope phase (Liu et al. 2006; Corradi et al. 2015; García-Rojas et al. 2016; Jones et al. 2016; Wesson et al. 2018), even if the nature of the relationship is still a mystery. Detailed analysis of the physical conditions and chemical abundances of a few objects has led several authors to suggest that the ionized gas comprises two different phases: an H-rich phase, which is dominated by hydrogen and helium recombination lines and CELs from heavy elements (O, N, Ne, Ar, etc.), alongside a much colder, H-poor phase with strong emission in

★ E-mail: vgomez@astro.unam.mx (VG-L); chris.morisset@gmail.com (CM); jogarcia@iac.es (JG-R)

[1]An updated data base on the ADFs measured in H II regions and PNe by Wesson, R. can be found at https://www.nebulousresearch.org/adfs/

the ORLs of heavy elements (C, N, O, Ne) and almost no CEL emission (Liu et al. 2000; Wesson, Liu & Barlow 2005; Corradi et al. 2015; Wesson et al. 2018). Under this hypothesis, accurately determining the physical conditions (electron temperature, T_e, and electron density, n_e) from different CEL and ORL diagnostics is crucial to properly determine the chemical abundances in each phase. However, having two gas-phase components with different chemical contents in an ionized gas complicates the computation of physical conditions and chemical abundances from an observational point of view.

A first estimate of how the presence of multiple gas components could affect the determination of physical conditions and chemical abundances in the main nebular shell was made by Liu et al. (2000), who computed new recombination coefficients for the T_e-sensitive [N II] λ5754 and [O II] λλ 7320+30 auroral lines and found that recombination excitation was important in exciting these lines and that ignoring it would lead to an overestimated T_e. These authors also proposed a fit to the contribution of radiative recombination (RR) to the widely used [O III] λ4363 auroral line, valid for $T_e > 8000$ K.

In this letter, we want to explore the classical [O III] λ4363/λ4959 T_e diagnostic, which can be strongly contaminated by recombination in extreme ADF PNe and therefore is no longer suitable for the measurement of T_e. In this work, we try to determine the contribution of the recombination to the [O III] λ4363 line, for the PNe NGC 6778 and Abell 46. In Section 2, we briefly describe the observational data used in this paper; in Section 3, we present new calculations to compute the recombination contribution to the [O III] λ4363 CEL emissivity; in Section 4, we estimate the recombination contribution from an observational point of view; and finally, in Section 5, we discuss our results.

2 OBSERVATIONS

We have used long-slit, intermediate-resolution spectra taken by our group of the extreme ADF PNe NGC 6778 (with FORS2-VLT 8.2 m; see Jones et al. 2016, ADF ∼ 18) and Abell 46 (with ISIS-WHT 4.2 m; see Corradi et al. 2015, ADF ∼ 120), respectively. The FORS2 observations covered the wavelength range of 3600–5000 Å with an average spectral resolution of 1.5 Å. The ISIS observations covered the wavelength range of 3610–5050 Å with a spectral resolution of 0.8 Å. For additional details on the observations and data reduction, we refer the reader to the original references.

For each long slit, we split the 2D spectrum into several spatial bins along the slit – 2.5 and 0.5 arcsec wide for Abell 46 and NGC 6778, respectively – which provides enough signal to noise for the faintest lines of interest to be measured. The fluxes of the [O III] λ4363 and λ4959 CELs and the O II λλ4649+50 ORL are obtained by automatically fitting Gaussian profiles to each line (for the ORL line, a double Gaussian is used to take into account the two members of the multiplet at 4649.13 and 4650.25 Å; we ignore the contribution of C III λ4650.25 because other lines of the same multiplet such as C III λ4647.42 have not been reported in the literature spectra of either object; Corradi et al. 2015; Jones et al. 2016). The uncertainties are determined in each spatial bin through a quadratic mean of the difference between the Gaussian fit and the signal.

In Fig. 1, we show examples of the line fitting process for the two PNe considered in this paper (upper panels for Abell 46 and lower panels for NGC 6778).

3 THE LIMITS IN COMPUTING [O III] λ4363 INTENSITY

To compute the [O III] λ4363 emission, we first consider the contribution from the radiative de-excitation of the O^{2+} ion following an excitation of the level $^1S_0$ by collision with a free electron of the plasma. This is obtained using PYNEB (Luridiana, Morisset & Shaw 2015) version 1.1.10, based on collision strengths by Storey, Sochi & Badnell (2014) and transition probabilities by Froese Fischer & Tachiev (2004).

We also have to carefully take into account the RR computed by the fit from Pequignot, Petitjean & Boisson (1991) and the dielectronic recombination (DR) from Nussbaumer & Storey (1984).

A fit for the total recombination contribution is given by Liu et al. (2000) as

$$\frac{I(4363)}{I(\mathrm{H}\beta)} = 12.4 \times t^{0.59} \times \frac{\mathrm{O}^{3+}}{\mathrm{H}^{+}}. \quad (1)$$

This line ratio [O III] λ4363/H β leads to a recombination coefficient of the single [O III] λ4363 line close to

$$\alpha_{4363}[\mathrm{cm}^3\ \mathrm{s}^{-1}] \simeq 3.3 \times 10^{-13} \times t^{-0.21}, \quad (2)$$

where $t = T_e/10^4$ K and considering $\alpha_{\mathrm{H}\beta} \simeq 2.94 \times 10^{-14} \times t^{-0.80}$ cm^3 s^{-1}.

This fit has been obtained when the DR has a considerable effect on the total recombination. This occurs for T_e between 8000 and 20 000 K. For $T_e < 5000$ K, the DR is negligible compared to the RR and the dependence on T_e does not follow the fit by Liu et al. (2000) anymore. We computed a new fit that reproduces the sum RR + DR within 3 per cent from 200 to 30 000 K:

$$\alpha_{4363} \simeq 2.63 \times 10^{-13} \times t^{-0.6} + 1.4 \times 10^{-13} \times \mathrm{e}^{-0.8/t}. \quad (3)$$

This fit is used in the multipurpose photoionization code CLOUDY (Ferland et al. 2017) since v17.02. In Fig. 2, we can see the variation of recombination coefficients with T_e for the RR and DR computed from Pequignot et al. (1991) and Nussbaumer & Storey (1984), respectively, as well as the fit by Liu et al. (2000) and our fit from equation (3). Note that the recombination computed in CLOUDY until v17.02 is rather overestimated as it uses Burgess & Seaton (1960) upper limits (purple line in Fig. 2).

It is important to notice here that, in general, no simple fit to the line ratio [O III] λ4363/H β (like the one obtained by Liu et al. 2000; see equation 1) can be obtained, as the regions where the recombination lines [O III] λ4363 and H β are produced can be very different, especially in terms of temperature, densities, and volume. The complete relation is

$$\frac{I(4363)}{I(\beta)} = \frac{\int_V E_{4363}\ \alpha_{4363}(T)\ n(\mathrm{O}^{3+})\ n(\mathrm{e})\ \mathrm{d}V}{\int_V E_\beta\ \alpha_\beta(T)\ n(\mathrm{H}^{+})\ n(\mathrm{e})\ \mathrm{d}V}, \quad (4)$$

where E_λ is the energy of the corresponding emission line and $n(X)$ is the density (by number) of the ion X responsible for the line emission (namely O^{3+} and H^+ in this case).

4 TESTING BIMETALLICITY HYPOTHESIS

In the following, we explore the case where the nebula is made of two regions of very different abundances. Then, the H β line is mainly emitted by the close-to-solar metallicity region 1 and the [O III] λ4363 recombination line is mainly emitted by a cold, metal-rich region 2; equation (4) leads to

$$\frac{I(4363)}{I(\beta)} = \frac{E_{4363}\ \alpha_{4363}(T_2)\ n(\mathrm{O}^{3+})_2\ n(\mathrm{e})_2\ V_2}{E_\beta\ \alpha_\beta(T_1)\ n(\mathrm{H}^{+})_1\ n(\mathrm{e})_1\ V_1}, \quad (5)$$

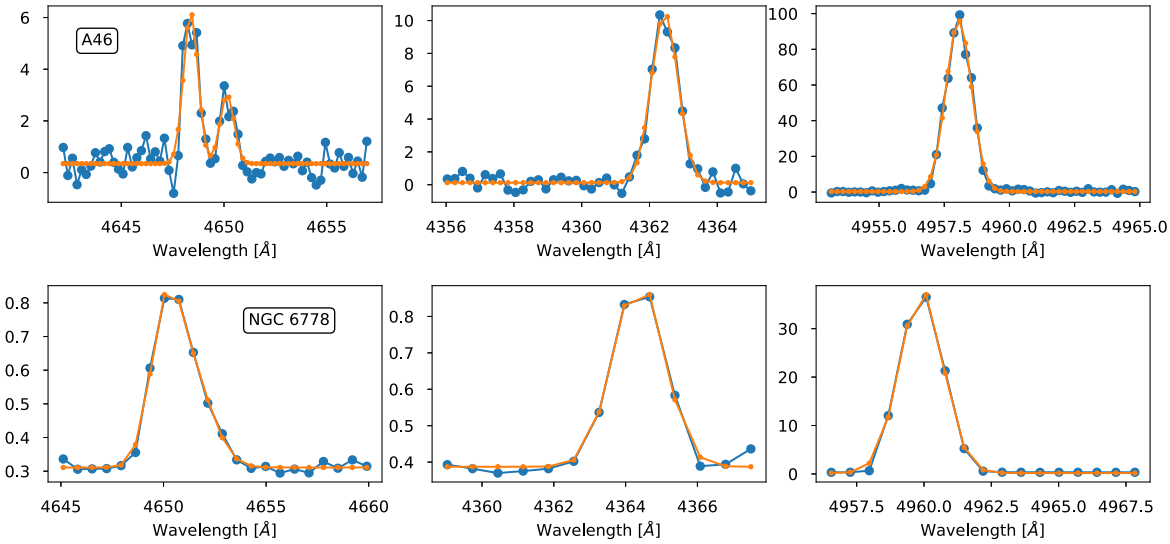

Figure 1. Examples of the fit to the emission lines. Upper panels for A46 and lower panels for NGC 6778. From left to right, the fits are for the O II λλ4649+50, the [O III] λ4363, and the [O III] λ4959 emission lines. Line fluxes are in arbitrary units.

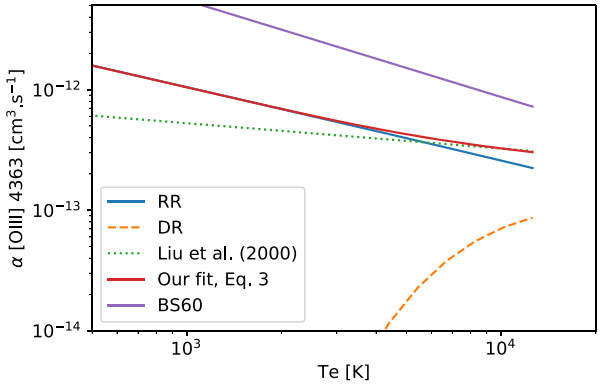

Figure 2. Recombination coefficients of [O III] λ4363: RR computed by Pequignot et al. (1991) (blue line), DR by Nussbaumer & Storey (1984) (orange dashed line), the value obtained by the formula from Liu et al. (2000) (equation 1, green dot line), and our fit to RR + DR (equation 3, red dot–dashed line). The actual value of RR + DR is not shown, as it is not distinguishable from our fit. The BS60 values from Burgess & Seaton (1960) upper limits used in CLOUDY are also shown in purple.

where the subscripts 1 and 2 indicate a mean value over the regions 1 and 2, respectively.[2]

Therefore, if T_1 and T_2 are very different, the simplification of the temperature-dependent power terms in the recombination coefficients of the two lines cannot be applied, nor do the n_e ratio $n(e)_1/n(e)_2$ and the volume ratio V_1/V_2 cancel. These ratios cancel only if the same region of the nebula is considered to emit both lines. The abundance ratio O^{3+}/H^+ only appears in a final relation if the implicit hydrogen densities $n(H)_1$ and $n(H)_2$ are the same.

[2]In the general situation, both lines are emitted by both regions and the line intensities are obtained by summing contributions from regions 1 and 2, leading to an even more complex equation for the line ratio:

$$\frac{I(4363)}{I(\beta)} = \frac{E_{4363}\ [I(4363)_1 + I(4363)_2]}{E_\beta\ [I(\beta)_1 + I(\beta)_2]}, \quad (6)$$

where $I(\lambda)_i = \alpha_\lambda(T_i)\, n(X)_i\, n(e)_i\, V_i$.

Gómez-Llanos & Morisset (2020) explored a case where an ADF(O^{2+}) ∼ 8, determined from observations of NGC 6153, can be reproduced by models in which the actual abundance ratio between the two components (termed the abundance contrast factor or ACF) is as high as 600. In their annex, they even show that an ACF of 1000 could lead to an apparent ADF of 1!

As derived from equations (5) and (6), it is very difficult to determine the contribution to the emission of the [O III] λ4363 that comes from the recombination in cases where the gas has two phases of different metallicities, with the metal recombination contribution mainly coming from the H-poor region. Estimating the parameters (e.g. T_e and n_e) of both regions needed in equation (5) is very hard, as for most objects the observed morphology does not allow to separate the emission coming from each region.

We have seen that, from a theoretical standpoint, it is almost impossible to correctly determine the contribution to the emission of the [O III] λ4363 line that originates from recombination. We can nevertheless attempt to obtain this contribution on an observational basis. In the following, we try to determine the recombination contribution by removing the contribution of the collisionally excited emission to the total emission.

Several authors have found that the spatial distribution of the [O III] λ4363 emission is very similar to that of the O II λ4649 one, but very different from the [O III] λ5007, 4959 lines (Corradi et al. 2015; García-Rojas et al. 2016; Jones et al. 2016; Wesson et al. 2018). The observed behaviour is consistent with an increasing temperature towards the central parts of the PN, which is at odds with the fact that O II ORL emission also peaks at the centre of the nebula, indicating that the cold, H-poor gas is located close to the central star (García-Rojas et al. 2016).

Adopting an n_e of 10^3 cm^{-3}, we estimate (using PYNEB, version 1.1.10) the spatial distribution of T_e in Abell 46 and NGC 6778 from the line ratio [O III] λ4363/4959. This is shown in blue in the top left and right panels of Fig. 4, respectively. In Abell 46, we can see a noticeable increase of the temperature estimation towards the centre of the object. In the left-hand and middle panels of Fig. 3, we show MUSE emission-line maps of the T_e-sensitive [S III] λ6312 and [S III] λ9068 CELs in NGC 6778 (García-Rojas, Boffin, Wesson et al., in preparation), and in the right-hand

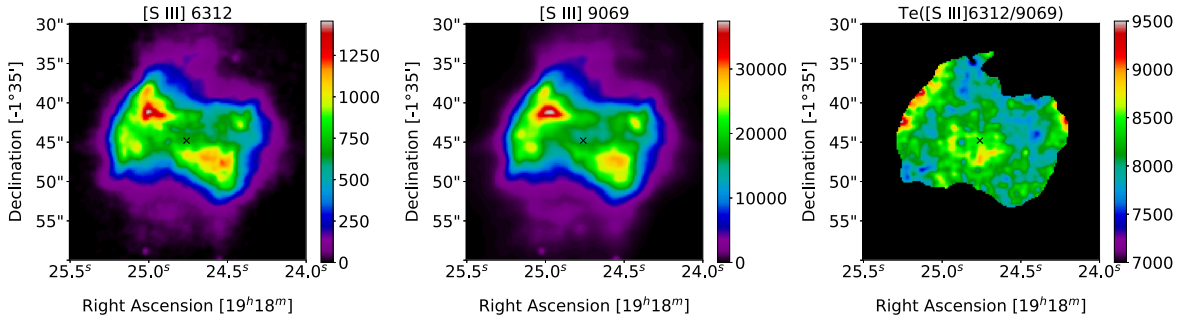

Figure 3. Left-hand and middle panels: MUSE emission line dereddened maps of the T_e-sensitive [S III] λ6312 and [S III] λ9068 CELs for NGC 6778, showing a very similar spatial distribution. The raw maps have been convolved with a Gaussian kernel with $\sigma = 1.5$ pixels. The '×' marks the position of the central star in both maps. The colour bar shows the flux in units of 10^{-20} erg s^{-1} cm^{-2} Å^{-1}. Right-hand panel: T_e([S III]) map computed with PYNEB from the extinction-corrected [S III] λ6312/λ9068 line ratio (a cut is made for intensities lower than 10 per cent of the peak emission in [S III] λ6312). The average T_e weighted by the flux of the λ6312 line is ∼8150 K.

panel, we show the T_e map obtained from the ratio of both lines, assuming a constant density $n_e \sim 1000$ cm^{-3}. The T_e map shows a roughly constant T_e distribution, with an average T_e, weighted by the [S III] λ6312 flux of ∼8150 K, implying that S^{3+} recombination emission is not significantly enhanced. This is consistent with previous studies, which suggested that the phenomenon of highly enhanced recombination-line emission is restricted to second-row elements (Barlow et al. 2003; Wesson et al. 2018). Following this observational evidence and the bimetallicity hypothesis, we adopt a constant T_e (red solid line in top panels of Fig. 4) for the close-to-solar region in Abell 46 and NGC 6778 of 10 000 and 8000 K (see above), respectively. The spatial distribution of the observed [O III] λ4363 line is plotted in orange in the middle panels of Fig. 4 for Abell 46 (left) and NGC 6778 (right). To obtain the collisional contribution of [O III] λ4363, we divide the observed emission of the line [O III] λ4959 by the theoretical line ratio [O III] λλ4959/4363 at the adopted constant temperature.[3] The result is shown in green in the middle panels of Fig. 4. We then subtract this collisional contribution to the total observed flux of [O III] λ4363 (orange line) to get the possible recombination contribution of λ4363 from O^{3+} (red line). For comparison, we also show the spatial distribution of O II λ4649 ORL (blue line) multiplied by a normalization factor. We can see that the residual spatial profile of [O III] λ4363 (red line) resembles that of the O II λ4649 ORL, indicating that the emissivity of the line is dominated by the recombination contribution. In the lower panels of Fig. 4, we show the spatial distribution of the recombination contribution to the total [O III] λ4363, which reaches up to 70 and 50 per cent of the total emission for Abell 46 (left) and NGC 6778 (right), respectively.

The recombination contribution to the [O III] λ4363 line may also be estimated using O^{3+} ORLs. Using Pequignot et al. (1991) via PYNEB, one can, for example, deduce I([O III] λ4363)/I(O III λ3762+) increasing from 0.35 to 0.55 (0.45 to 0.7) when T_e increases from 1000 to 20 000 K in case B (case A). Jones et al. (2016) report I(O III λ3760) = 0.61 (Hβ = 100) for NGC 6778. One can estimate the intensity of the whole V2 multiplet I(O III λ3762+) to be ≃1.00, leading to a prediction of I([O III] λ4363) from recombination to be of the order of 0.4–0.5. This is between 20 and 25 per cent of the observed I([O III] λ4363) = 2.07, close to what we obtain for the same PN (see Fig. 4).

[3]This is obtained with PYNEB, from the ratio of emissivities $\varepsilon(4959)/\varepsilon(4363)$ using the adopted temperature of 8000 and 10 000 K for NGC 6778 and Abell 46, respectively, and a density of 10^3 cm^{-3}. The corresponding ratios are 117 and 51.

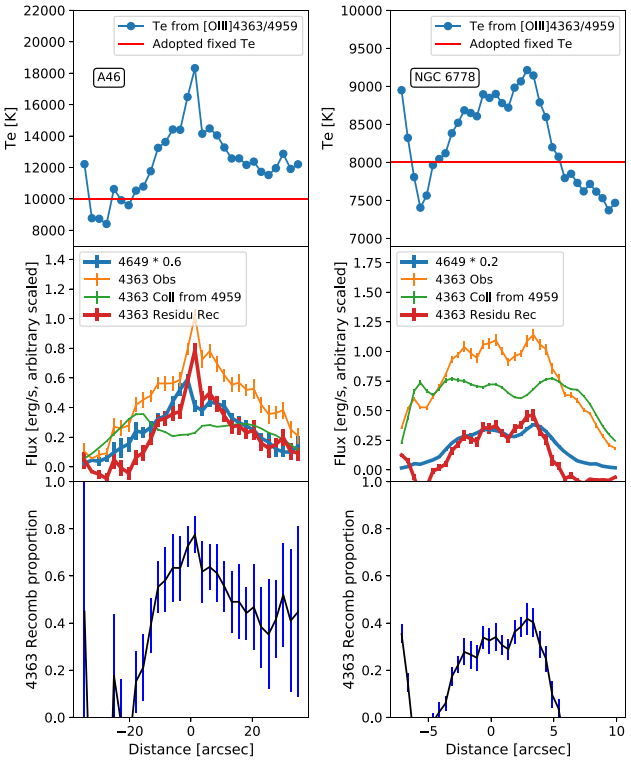

Figure 4. Top panels: T_e estimated from [O III] λ4363/λ4959 ratio. The red line represents the adopted T_e. Middle panels: Spatial distribution of observed [O III] λ4363 (orange), the expected profile of [O III] λ4363 emitted by collision assuming the fixed T_e from the upper panels and the profile of [O III] λ4959 (green), the residuals from subtracting the expected collisional [O III] λ4363 profiles from the observed one (red), and for comparison the O II λ4649 profile multiplied by a scale factor (blue). Lower panels: Relative contribution of recombination to the [O III] λ4363 line.

5 DISCUSSION

In this paper, we explored the very crude hypothesis that the T_e of the close-to-solar abundance gas in the central part of the nebula is the same as in the main nebula (the red line showing the adopted value in Fig. 4). This may not be the case. If one wants to increase

the precision in the determination of the [O III] λ4363 recombination contribution, one needs to make a detailed photoionization model of the object. This requires a good atmosphere model for the ionizing source in order to correctly reproduce the heating of the nebula. One also may need to take into account the presence of dust and its properties, to accurately compute the balance between the heating and the cooling in the inner part of the nebula. This is totally out of the scope of the simple 'proof of concept' presented in this letter.

One can also question the precision of the atomic data involved in the different parts of the emission calculus, especially the RR at low temperature. Although the DR seems to vanish at low temperature (Fig. 2), it has recently been pointed out that the effect of 'exotic' atomic processes like *Rydberg enhanced recombination* (RER) could be very important in these regimes. RER could thus have an impact on the predicted ionization balance and, hence, on the derived ionic abundances (Nemer et al. 2019), changing $n(O^{3+})$ in equation 5. The residual obtained in Section 4 and associated with the O^{+} recombination can also include a contribution from RER, as such an exact computation of the RER-based emission will be important in understanding the entirety of the [O III] λ4363 emission.

Regarding observations, it is becoming increasingly clear that for a complete understanding of this problem, a combination of detailed photoionization models with deep IFU observations might improve the situation. In the case of extreme ADF PNe, where two different plasma components coexist, the Balmer and Paschen jumps might not be indicative of any real gas temperature, as they are only a weighted mean of two very different phases of gas. Similarly, the recombination lines (e.g. O II or H I) are not telling us the value of the ionic abundance ratio O^{2+}/H^{+}, as it is impossible to determine what fraction of H^{+} actually comes from the cold region. The exact weight of the H-poor zone can only be constrained through detailed photoionization models. From the comparison of theoretical models with observations, one can obtain the physical properties (T_e, n_e, mass, and abundances) of the two plasma components that reproduce the observed spectra. However, a detailed treatment of the physics has revealed that the ADF might be only a rough estimate of this discrepancy and is unlikely to provide 'real' information on the ORL/CEL abundance ratios (see Gómez-Llanos & Morisset 2020).

ACKNOWLEDGEMENTS

The authors thank the referee for their comments. This paper is based on observations made with ESO Telescopes at the Paranal Observatory under programme IDs 093.D-0038 and 097.D-0241, and on observations made with the *William Herschel Telescope* operated on the island of La Palma by the Isaac Newton Group of Telescopes in the Spanish Observatorio del Roque de los Muchachos of the Instituto de Astrofísica de Canarias. VG-L and CM acknowledge support from projects Consejo Nacional de Ciencia y Tecnología/CB2015 – 254132 and Universidad Nacional Autónoma de México/Programa de Apoyo a Proyectos de Investigación e Innovación Tecnológica – IN101220. JG-R acknowledges support from an Advanced Fellowship from the Severo Ochoa excellence program (SEV-2015-0548). JG-R, DJ, and RC acknowledge support from the State Research Agency (AEI) of the Spanish Ministry of Science, Innovation and Universities (MCIU) and the European Regional Development Fund (FEDER) under grant AYA2017-83383-P.

DATA AVAILABILITY

The original data used in the paper are available under request to the authors.

REFERENCES

Barlow M. J., Liu X. W., Péquignot D., Storey P. J., Tsamis Y. G., Morisset C., 2003, in Kwok S., Dopita M., Sutherland R., eds, Proceedings of the 209th Symposium of the International Astronomical Union held at Canberra, Australia, 19-23 November, 2001, Planetary Nebulae: Their Evolution and Role in the Universep. 373
Burgess A., Seaton M. J., 1960, MNRAS, 120, 121
Corradi R. L. M., García-Rojas J., Jones D., Rodríguez-Gil P., 2015, ApJ, 803, 99
Ferland G. J. et al., 2017, Rev. Mex. Astron. Astrofis., 53, 385
Froese Fischer C., Tachiev G., 2004, At. Data Nucl. Data Tables, 87, 1
García-Rojas J., Corradi R. L. M., Monteiro H., Jones D., Rodríguez-Gil P., Cabrera-Lavers A., 2016, ApJ, 824, L27
García-Rojas J., Wesson R., Boffin H. M. J., Jones D., Corradi R. L. M., Esteban C., Rodríguez-Gil P., 2019, AAA Workshop Ser., 11, 33
Gómez-Llanos V., Morisset C., 2020, MNRAS,
Jones D., Wesson R., García-Rojas J., Corradi R. L. M., Boffin H. M. J., 2016, MNRAS, 455, 3263
Liu X.-W., Storey P. J., Barlow M. J., Danziger I. J., Cohen M., Bryce M., 2000, MNRAS, 312, 585
Liu X. W., Barlow M. J., Zhang Y., Bastin R. J., Storey P. J., 2006, MNRAS, 368, 1959
Luridiana V., Morisset C., Shaw R. A., 2015, A&A, 573, A42
Nemer A. et al., 2019, ApJ, 887, L9
Nussbaumer H., Storey P. J., 1984, A&AS, 56, 293
Peimbert M., 1967, ApJ, 150, 825
Peimbert M., Peimbert A., Delgado-Inglada G., 2017, PASP, 129, 082001
Peña M., Ruiz-Escobedo F., Rechy-García J. S., García-Rojas J., 2017, MNRAS, 472, 1182
Pequignot D., Petitjean P., Boisson C., 1991, A&A, 251, 680
Richer M. G., Georgiev L., Arrieta A., Torres-Peimbert S., 2013, ApJ, 773, 133
Richer M. G., Suárez G., López J. A., García Díaz M. T., 2017, AJ, 153, 140
Stasińska G., Tenorio-Tagle G., Rodríguez M., Henney W. J., 2007, A&A, 471, 193
Storey P. J., Sochi T., Badnell N. R., 2014, MNRAS, 441, 3028
Torres-Peimbert S., Peimbert M., Daltabuit E., 1980, ApJ, 238, 133
Wesson R., Liu X. W., Barlow M. J., 2003, MNRAS, 340, 253
Wesson R., Liu X. W., Barlow M. J., 2005, MNRAS, 362, 424
Wesson R., Barlow M. J., Liu X. W., Storey P. J., Ercolano B., De Marco O., 2008, MNRAS, 383, 1639
Wesson R., Jones D., García-Rojas J., Boffin H. M. J., Corradi R. L. M., 2018, MNRAS, 480, 4589

This paper has been typeset from a TEX/LATEX file prepared by the author.

Chapter 4

Spatially resolved H II regions

The multi-component approach discussed in sec. 2.3, and applied to PNe in chapter 3, can also be used to address other astrophysical objects. In this chapter we present a work (in progress) that combines 1D models of H II regions to create pseudo-3D models (see Morisset 2013; Gesicki et al. 2016). The aim is to model the behaviour of spatially resolved observations of the galaxy NGC 628 obtained by the SIGNALS survey (Rousseau-Nepton et al. 2018, 2019) and study star forming regions in galaxies. According to the results, it could be expanded to the other galaxies observed by the SIGNALS survey. By building original grids of complex photoionization models of H II regions with 3D photoionization modeling techniques, the parameters of the H II regions: ionization parameter, morphology of the gas, density structure, and chemical composition, will be estimated. The main hypothesis of the research is that photoionization models can give a realistic representation of the observed extragalactic H II regions and that the large amount of resolved data obtained by the SIGNALS survey, when compared to theoretical models, can break the reported degeneracy in the metallicity determination and/or improve the estimation of other parameters of the gas, as the ionization parameter.

4.1 Theoretical framework

The direct method (see sec. 2.1) relies on the observation of temperature-sensitive emission line ratios, implying faint auroral lines (e.g. [O III] λ 4363). This kind of lines are not always observable in extragalactic objects. In such cases, the so-called strong-line method (SLM), that only requires measurements of bright emission lines, is used to estimate the metallicity. The SLM is calibrated with theoretical models or metallicity determinations obtained with the direct method. This is a statistical method, applied to sets

of observations that need to be similar to the ones used to calibrate the SLM. Some issues with SLM are: (i) there is a large dispersion in the metallicity calibrators presented by different authors, (ii) in some cases different metallicities can be obtained for the same observed line ratios; a criterion needs to be defined to choose which value is adopted, and (iii) the calibrators based on the direct method and on theoretical models do not agree.

On the other hand, the emission lines observed in galaxies can result from different excitation sources: emissions from young hot stars (H II regions), from evolved low mass stars, or from Active Galactic Nuclei (AGN), and even shocks. Baldwin et al. (1981) proposed a method to classify the main excitation mechanism in extragalactic objects. The method combines emission line ratios of high and low ionization degrees like [O III] λ 5007/Hβ and [N II] λ 6584/Hα. The observed line ratios are plotted in a diagram (BPT diagram) and the source is classified according to its position in the diagram. Some of the emission lines used in the BPT diagrams are also used in the strong line method to determine chemical composition of distant objects.

4.2 Observations with Integral Field Spectroscopy

In the last decade, observations using Integral Field Spectrograph (IFS) have improved the study of the radial properties of galaxies, such as the star formation rate (SFR), emission line ratios, and chemical abundances. IFS are instruments that allow us to obtain observations with spectral and spatial resolution in extended objects. Each pixel (also called spaxel) observed with an IFS corresponds to a single spectrum. Surveys like CALIFA (Sánchez et al. 2012), SAMI (Croom et al. 2012), MaNGA (Bundy et al. 2015), and AMUSING++ (Galbany et al. 2016) have studied the radial properties of a large number of galaxies at different redshifts using IFS observations. The survey data is plotted in BPT diagrams to classify the ionization sources of the gas in the different regions of galaxies. The physical spatial resolution in these surveys varies from 0.3-2.5 kpc (Sánchez 2020) while the typical sizes of H II regions (1-100 pc) are below these resolution values.

The SIGNALS (Star formation, Ionized Gas, and Nebular Abundances) survey is an ongoing project to study massive star formation and H II regions in a sample of local galaxies. The observations are being performed with the imaging Fourier transform spectrograph SITELLE (Spectro-Imageur à Transformée de Fourier pour l'Étude en Long et en Large des raies d'Émission) at the Canada-France-Hawaii Telescope (CFHT). The spatial resolution obtained with SITELLE (2-40 pc) is higher and the field of view (11'x11') is larger than for other observations using IFS, allowing a unique deeper study of the spatial properties of a large sample of star forming regions with various properties. At the end of the survey, there will be a sample of about 50,000 H II regions observed in three filters: SN1 (363-386 nm), SN2 (482-513 nm), and

SN3 (647-685 nm) at a spectral resolution of 1000, 1000, and 5000 respectively. The emission lines measured from these three filters are: [O II] λ 3727, Hβ (λ 4861), [O III] λ 4959, λ 5007, [N II] λ 6548, λ 6584, Hα (λ 6563), He I λ 6678, and [S II] λ 6716, λ 6731. They include many of the strong lines used in the BPT diagrams to determine abundances from SLM. Nevertheless, the SLM being calibrated on global regions, can not be used to determine abundances of spatially resolved regions. New methods need to be developped.

4.3 Modeling astrophysical nebulae

Photoionization models simulate the ionization and thermal conditions of plasma, as well as the radiative transfer of an ionizing source toward a nebula. Cloudy (Ferland et al. 2017) is one of the most complete codes that can be used to simulate photoionized gas (see sec. 2.2.1) such as H II regions. In photoionization models, one needs to specify: the radiation field of the ionization source and the properties of the gas. The ionization source for H II regions can be a few young hot stars, or one or more massive clusters of stars of different stellar ages. The python library PyCloudy (see sec. 2.2.2) manages the Cloudy inputs and outputs and allows us to generate models and grids of models with python scripts. The photoionization code Cloudy generates 1D models, PyCloudy allows us to combine several 1D models to generate a pseudo-3D model that can be projected in 2D to be compared with spatially resolved observations.

4.4 Computing spatially resolved models to reproduce resolved observations

The proposed research includes a large sample of H II regions observed by the SIGNALS survey at resolutions that are not reached by any other surveys. To take the maximum advantage of the unique resolution of the SITELLE observations, new and original models need to be performed: the *ad hoc* grid of 2D photoionization models that will be developed during this project will help exploit the unique and large sample of data of this survey. From the obtained detailed models, we will be able to access most of the information that is lost when the regions can not be resolved. This will strongly increase our knowledge on interaction between the stars and the interstellar medium, the gas properties in relation with the star formation processes, and therefore extend our understanding on the formation and evolution of galaxies.

We will use spatially resolved observations of the entire galaxy NGC 628 with SITELLE at the CFHT (Rousseau-Nepton et al. 2018). In the figures 4.1, 4.2, and 4.3 we plot: the BPT-SII, BPT-NII diagrams and

distribution of the spaxels for: the distance from the emission peak, the distribution of Hα, some emission line ratios ([O III] λ 5007/Hβ, [S II] λ 6716+/Hα, [N II] λ 6584/Hα), and a RGB color plot (Red: [S II]/Hα, Green: [O III]/Hβ and Blue channel: [N II]/Hα), for eight representative H II regions. The method for selecting the H II regions and its spatial limits are defined in Rousseau-Nepton et al. (2018). From the spatially resolved BPT diagrams in the figures 4.1, 4.2, and 4.3, we see a general trend with higher [O III]/Hβ and lower [S II]/Hα or [N II]/Hα closer to the central emission peak. And a conical shape where [O III]/Hβ and [S II]/Hα or [N II]/Hα increase, at larger distances. This is more evident for the BPT-SII diagram, although at larger distances from the emission peak there is a bigger dispersion.

The top-left panel of fig. 4.4 shows a BPT diagram of the spatially resolved emission line ratios [O III] λ 5007/Hβ versus ([S II] λ 6716 + λ 6731)/Hα of the 25 brightest H II regions in NGC 628 (similar to fig. 25 in Rousseau-Nepton et al. (2018)). We can see several clouds of points, each point corresponding to a spaxel of an individual H II region. For each cloud of points, the color represents the distance outwards from the central peak of their Hα emission. We notice a cone shape in the distribution of the points in each cloud. In the original BPT diagram, a single point usually represents an entire H II region or a combination of several H II regions observed in a single aperture. This is not the case for the SIGNALS data, where numerous spaxels have been obtained for each H II region, making this detailed study possible. The aim of this work is to investigate the additional information that can be obtained from the shape, extension, and orientation of these spatially resolved data by generating grids of 3D models to be compared with the observations. To compare with the H II regions plotted in top-left panel of fig. 4.4, we show two examples of H II region photoionziation models: one with spherical (M_S) symmetry and other with ellipsoidal (M_E) shape (that is generated combining several 1D models using the `C3D` class of PyCloudy, see Morisset 2014). The 2D projection of the Hα surface brightness is plotted in fig. 4.5 for both models. The SED of the central star (defined by the bursts: age of $10^{6.4}$ years, metallicity of 0.004 solar, and rate of ionizing photons of $10^{50.81}$ s^{-1}), which is the same in M_S and M_E models, as well as the solar chemical abundances, canonical dust and filling factor of 0.01. What changes between the M_S and M_E models are the hydrogen density and inner radius (as a function of θ), with central values of 100 cm^{-3} and 8×10^{19} cm, respectively. The M_S model have the same hydrogen density and inner radius for all the azimuthal angles (0 to 2π), while for the M_E model these two parameters are multiplied by an ellipticity factor:

$$\varepsilon = \frac{a * b}{\sqrt{(b \cdot \sin(\theta))^2 + (a \cdot \cos(\theta))^2}} \tag{4.1}$$

with a = 3 and b = 1.

We get the initial set of parameters for the M_S and M_E models, by first: integrating the emission of ([S II] λ 6716 + λ 6731)/Hα and [O III] λ 5007/Hβ for each of the 25 brightest H II regions in NGC 628. Then

by searching in the BOND project (Vale Asari et al. 2016) of the Mexican Million Models database (3MdB* Morisset et al. 2015) the models with values for [S II]/Hα and [O III]/Hβ that were closer to the observed integrated values. In the top right panel of fig. 4.4 we plot the integrated value of the BPT diagram for the spherical model with a red diamond , and the same observational data of NGC 628 than in the top-left panel in gray. In the bottom-left panel is plotted the 2D projection of the spherical model for the BPT diagram, the color-bar represents the distance from the center of the region. It can be seen from that plot that a 2D projection of a spherical model returns a single line in the BPT diagram, so this conic shape observed in the spatially resolved H II regions of NGC 628 can not be reproduced with a model of spherical symmetry. On the bottom-right panel of the figure, is plotted the 2D projection of the BPT diagram for the ellipsoidal model. Although these results are preliminary the difference in the shape on the BPT diagram can be noticed between the spherical and ellipsoidal models. By generating grids of this composite non-spherical models, the properties of the clouds of points will be parameterized and correlated with the properties of the modeled nebulae. Machine learning techniques to study the behavior of the large model and observational database can be applied.

The proposed research has never been done until now, combining the unique quality of the SIGNALS observations and the capacities of pseudo-3D modeling with PyCloudy. Possible extensions of the project are considered as future work, as the exploration of the effect of summing individual H II regions in a single observation - degrading the resolution of the SIGNALS data - in order to simulate observations of galaxies at large distances and to improve the analysis of their H II regions.

*https://sites.google.com/site/mexicanmillionmodels/

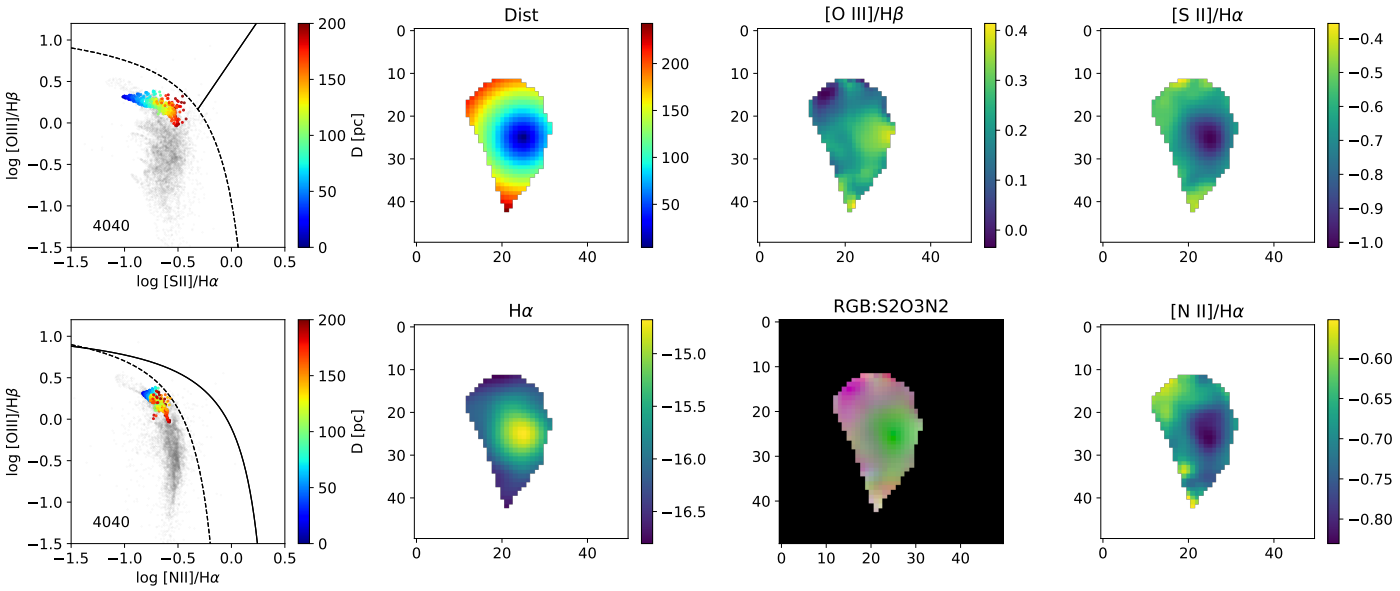

Figure 4.1: Illustrations of the observational properties of a single region (here region 4040). Top row, from left to right: Distribution of the spaxels in the BPT-SII diagram, colored by the distance to the peak of the emission (D[kpc]); spatial distribution of the distance to the peak in kpc, the x and y axis are running on 50 pixels around the peak locus; spatial distribution of log [O III]/Hβ; spatial distribution of log [S II]/Hα. Bottom row, from left to right: Distribution of the spaxels in the BPT-NII diagram, colored by the distance to the peak of the emission (D[kpc]); spatial distribution of the Hα emission (in logarithmic scale); RGB color plot with Red: [S II]/Hα, Green: [O III]/Hβ and Blue channel: [N II]/Hα; spatial distribution of the log [N II]/Hα line ratio.

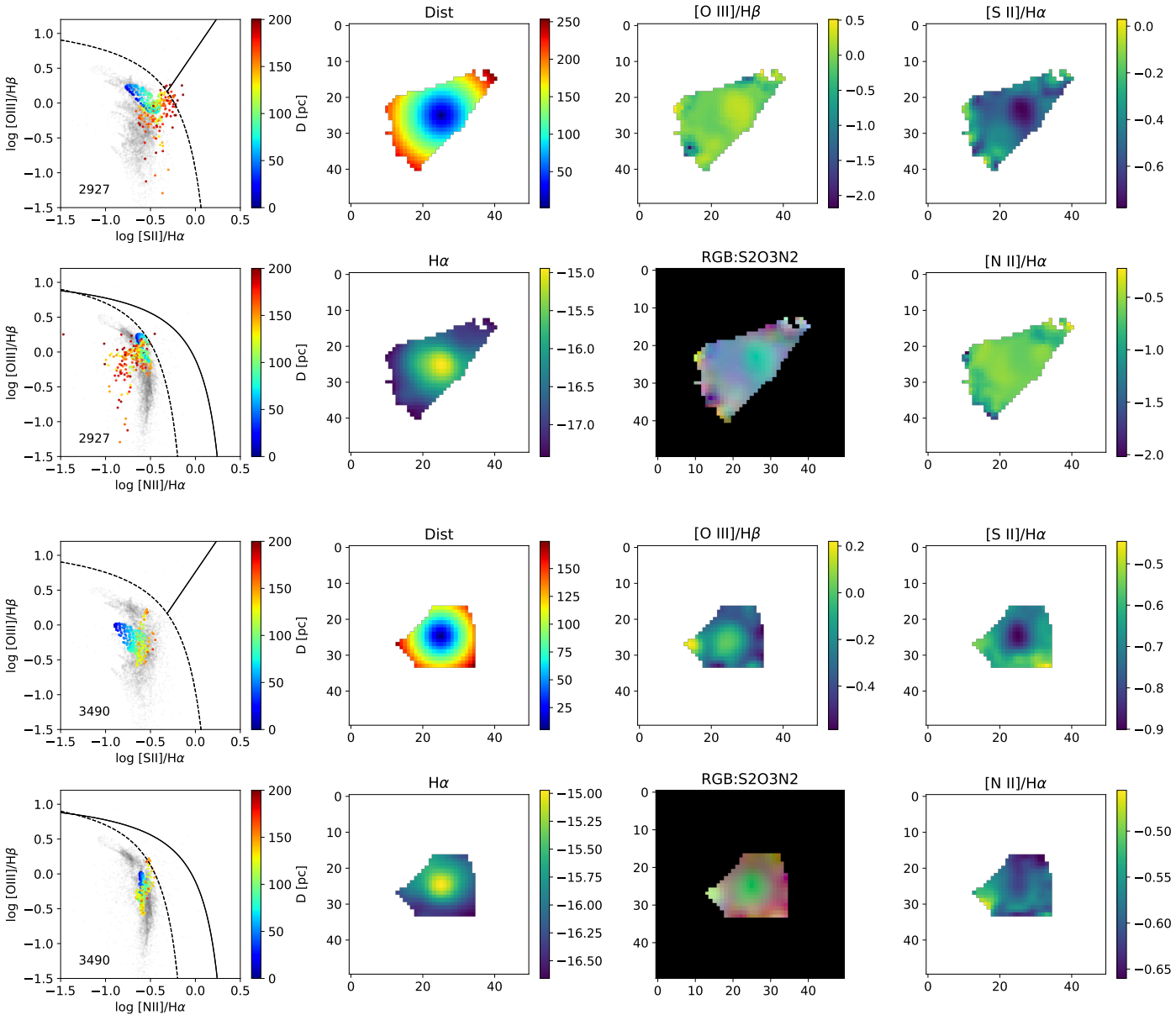

Figure 4.2: Same as Fig. 4.1 for region 2927, 3490, from top to bottom.

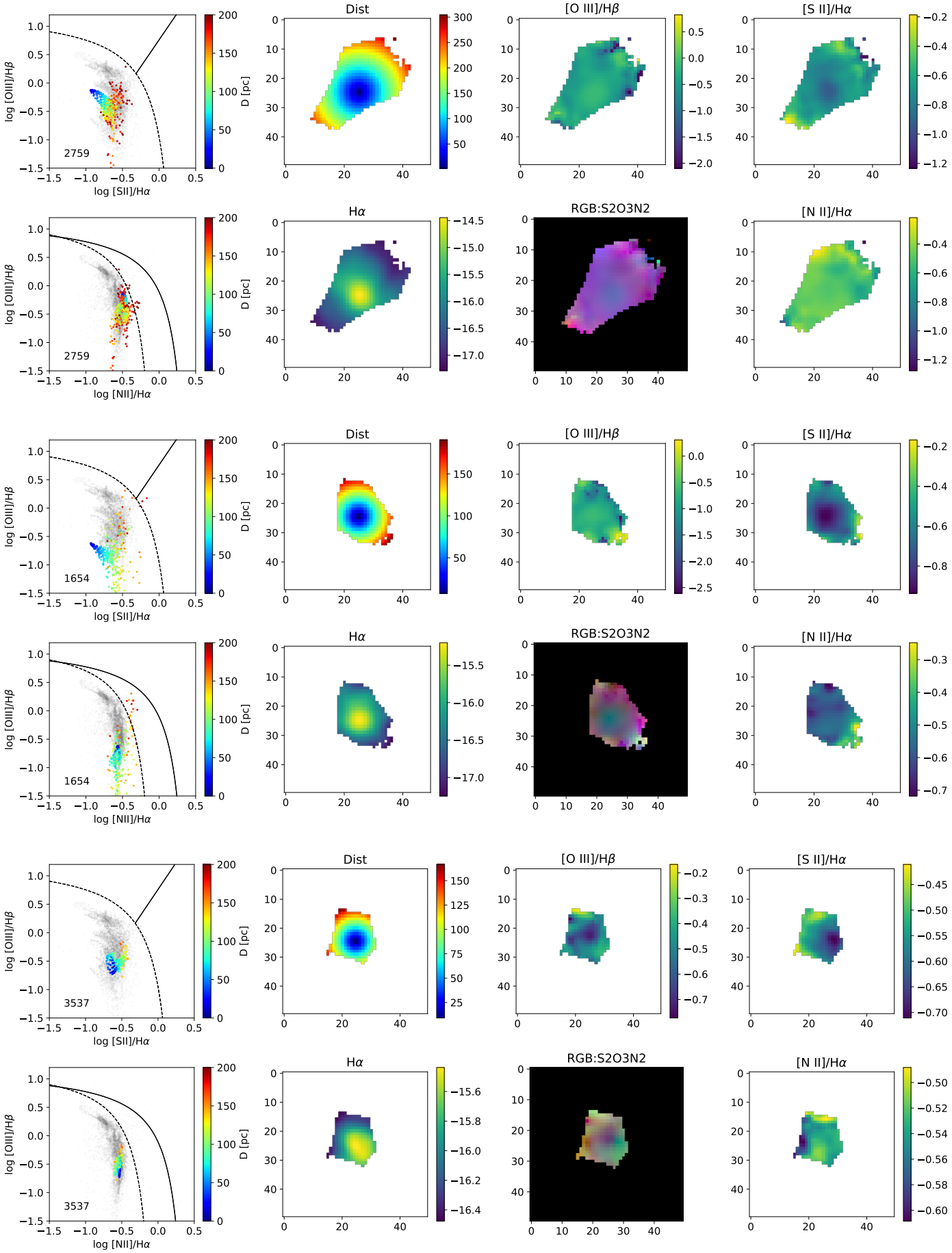

Figure 4.3: Same as fig. 4.1 for region 2759, 1654 and 3537, from top to bottom.

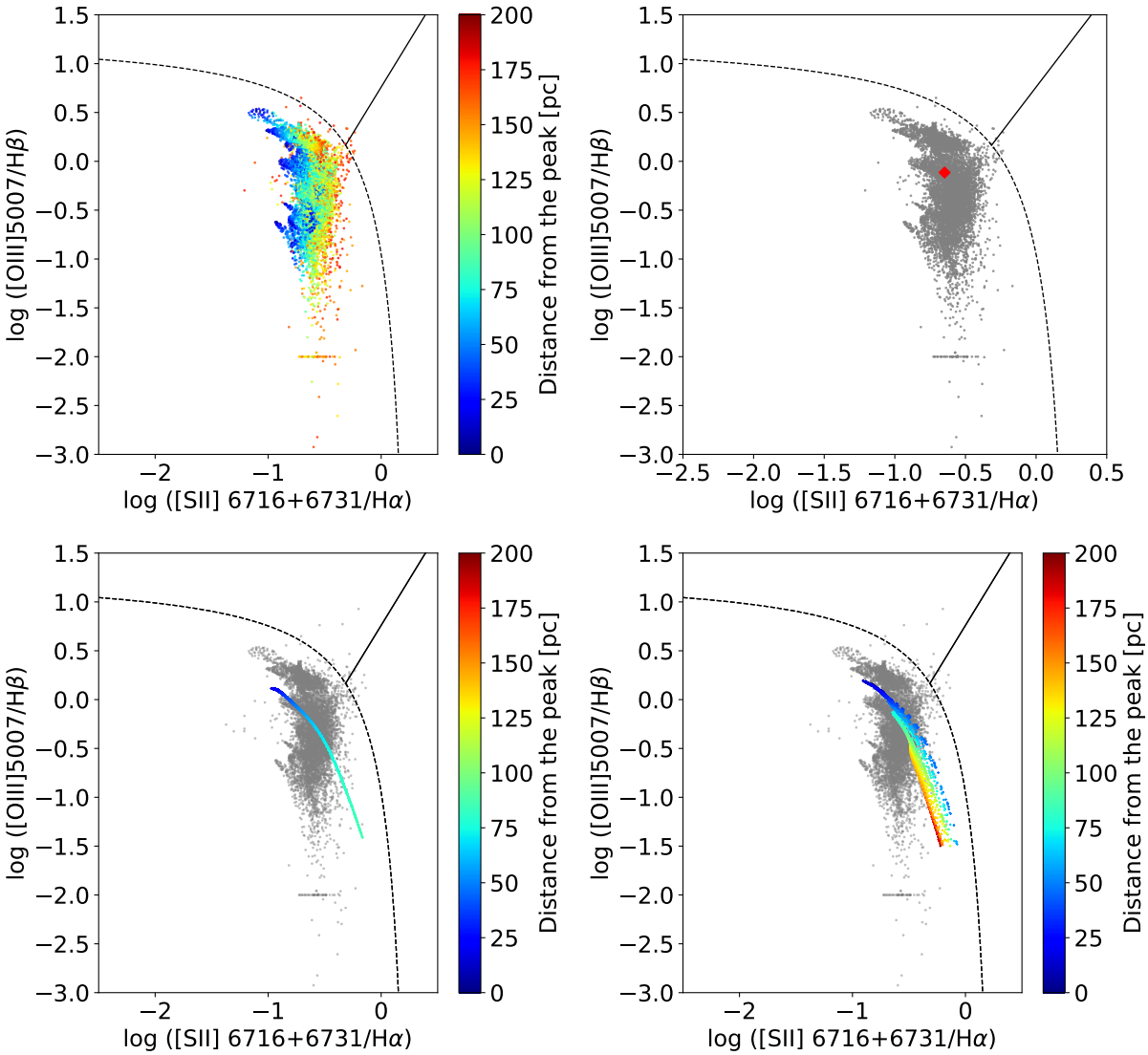

Figure 4.4: Top-left panel: BPT diagram of spatially resolved 25 brightest H II regions in NGC 628 (Rousseau-Nepton et al. 2018), where the colorbar represents the distance to the central peak of each region. In the other three panels these observations are plotted in gray. Top-right panel: Red diamond represents the integrated value for a 1D spherical H II region photoionization model. Bottom-left panel: 2D projection of spherical H II region photoionization model, color-bar represents the distance to the center of the cloud. Bottom-right panel: 2D projection of a non-spherical H II region photoionization model, color-bar represents the distance to the center of the cloud.

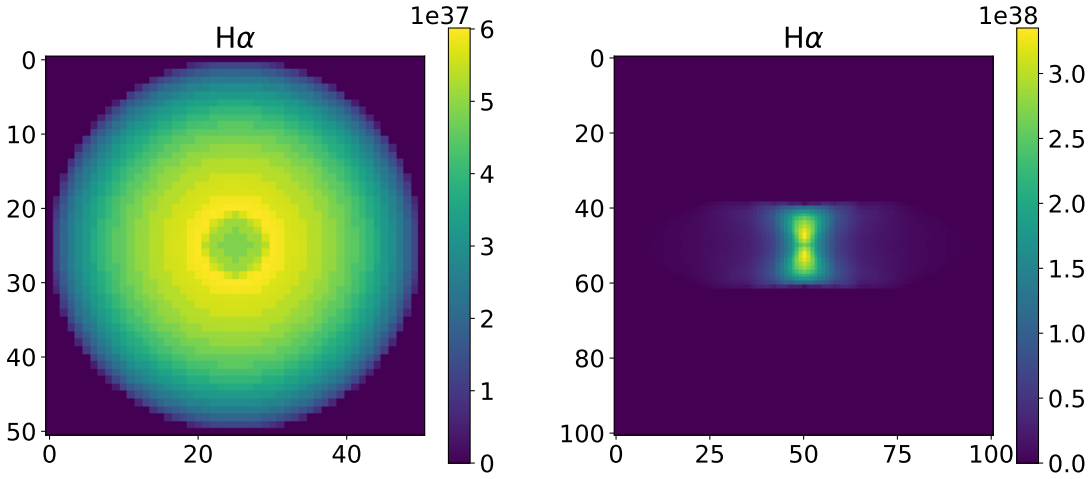

Figure 4.5: Left (right) panel shows a map of the 2D projection of the Hα distribution of an spherical (non-spherical) H II region photoionization model.

Chapter 5

Discussion and conclusions

We have developed multiple component models to address some questions on the nature of complex objects. We have successfully reproduced the temperature and abundance difference for PN NGC 6153 with a two-metallicity gas by combining three 1D models. The constraints on the model parameters were based on observations and previous models of the PN NGC 6153. The difference in metallicity and volume was explored between the two regions, up to extreme values of 3 orders of magnitude difference in the metallicity. A degeneracy was found between the volume and the difference in metallicity. When comparing with observations, two solutions were found that reproduce the difference in temperatures and chemical abundances: one with lower metallicity (log O/H = -1.15) and higher volume ($\sim$0.4% of the total volume) and other with higher metallicity (log O/H = -0.55) and lower volume ($\sim$0.2% of the total volume). Both solutions have a fraction of volume lower than 1%, and a mass of oxygen in the metal-rich zone between 25 y 60% of the total oxygen mass. The most relevant result of this work is that the ADF does not represent the difference in metallicities between the MR and the components with *cts* abundances, i.e. the ACF, the ACF being much higher.

From the results obtained with the two-metallicity models, an additional study was performed on the effect the recombination of [O III] λ 4363 has on electron temperature estimations under such dual metallicity conditions. This was done using observations of two PNe: Abell 46 and NGC 6778. It was found that the contribution of recombination to the total [O III] λ 4363 emission, can be up to 70% and 40%, for these two objects, respectively. If the cold metal-rich plasma is not considered, the electron temperature and the total abundances will be wrongly estimated. This shows the importance of taking into account the complexity when modeling astronomical objects, that is even more important when applying methods that are based on hypothesis of a simpler object (like the direct method).

The proof of concept presented in chapter 4 is another example where a simple spherical model can not account for the observed features. This work, although preliminary has an interesting potential on the possible features to be extracted from spatially resolved H II regions at the high spatial resolution of the SIGNALS survey. In this work we use the Mexican Million Models (3MdB) database combined with Machine Learning techniques to constrain (based on the observed data) the initial parameters of the models. The method developed initialy to reproduce the observations of the galaxy NGC 628 can be used latter for other galaxies of the SIGNALS survey.

When a model is not able to reproduce the observations, it does not always mean that the physical assumptions of the model are wrong, but it can also be an indication that a more complex description is necessary. The number of dimensions of the problem needs to be increased, increasing also the difficulty of finding enough observables to constrain all the free parameters to be determined. From the results obtained in this work (and from others in the literature), I show that, in the case of theoretical studies of astrophysical nebulae, a more complex model can be achieved by summing up two or more 1D models, leading to a multi-component model (see sec. 2.3 Morisset & Pequignot 1996; Morisset et al. 2002, 2004; Gesicki et al. 2016; Ramambason et al. 2020). So, many times it is not that the physics applied to the models needs to be improved, but rather that our simplifications in the description of the object may be too extreme.

Bibliography

Aller, L. H. & Menzel, D. H. 1945, Astrophysical Journal, 102, 239

Baldwin, J. A., Phillips, M. M., & Terlevich, R. 1981, Public. of the Astron. Soc. Pac., 93, 5

Barker, T. 1982, Astrophysical Journal, 253, 167

Barker, T. 1983, Astrophysical Journal, 267, 630

Barker, T. 1984, Astrophysical Journal, 284, 589

Borkowski, K. J., Harrington, J. P., Blair, W. P., & Bregman, J. D. 1994, Astrophysical Journal, 435, 722

Bowen, I. S. 1934, Public. of the Astron. Soc. Pac., 46, 146

Bowen, I. S. & Wyse, A. B. 1939, Lick Observatory Bulletin, 19, 1

Bundy, K., Bershady, M. A., Law, D. R., Yan, R., Drory, N., MacDonald, N., et al. 2015, Astrophysical Journal, 798, 7

Butler, K. & Zeippen, C. J. 1989, Astron. & Astrophys., 208, 337

Croom, S. M., Lawrence, J. S., Bland-Hawthorn, J., Bryant, J. J., Fogarty, L., Richards, S., et al. 2012, Mon. Not. of the Royal Astron. Soc., 421, 872

Davey, A. R., Storey, P. J., & Kisielius, R. 2000, Astron. & Astrophys., Supplement, 142, 85

Delgado-Inglada, G., Morisset, C., & Stasińska, G. 2014a, Mon. Not. of the Royal Astron. Soc., 440, 536

Delgado-Inglada, G., Morisset, C., & Stasińska, G. 2014b, in Revista Mexicana de Astronomia y Astrofisica Conference Series, Vol. 44, Revista Mexicana de Astronomia y Astrofisica Conference Series, 17–17

Dere, K. P., Del Zanna, G., Young, P. R., Landi, E., & Sutherland, R. S. 2019, Astrophysical Journal, Supplement, 241, 22

Dere, K. P., Landi, E., Mason, H. E., Monsignori Fossi, B. C., & Young, P. R. 1997, Astron. & Astrophys., Supplement, 125, 149

Draine, B. T. 1978, Astrophysical Journal, Supplement, 36, 595

Draine, B. T. 2003, Annual Review of Astron and Astrophys, 41, 241

Draine, B. T. & Kreisch, C. D. 2018, Astrophysical Journal, 862, 30

Dzifčáková, E. & Kulinová, A. 2003, Sol. Phys., 218, 41

Ercolano, B. 2006, in IAU Symposium, Vol. 234, Planetary Nebulae in our Galaxy and Beyond, ed. M. J. Barlow & R. H. Méndez, 259–266

Ercolano, B., Barlow, M. J., Storey, P. J., & Liu, X. 2003a, Mon. Not. of the Royal Astron. Soc., 340, 1136

Ercolano, B., Barlow, M. J., Storey, P. J., Liu, X., Rauch, T., & Werner, K. 2003b, Mon. Not. of the Royal Astron. Soc., 344, 1145

Ercolano, B. & Storey, P. J. 2006, Mon. Not. of the Royal Astron. Soc., 372, 1875

Escalante, V., Morisset, C., & Georgiev, L. 2012, Mon. Not. of the Royal Astron. Soc., 426, 2318

Esteban, C., Toribio San Cipriano, L., & García-Rojas, J. 2018, in Chemical Abundances in Gaseous Nebulae, ed. G. Hägele, M. Cardaci, & E. Pérez-Montero, 23

Fang, X., Storey, P. J., & Liu, X.-W. 2011, Astron. & Astrophys., 530, A18

Ferland, G. J., Chatzikos, M., Guzmán, F., Lykins, M. L., van Hoof, P. A. M., Williams, R. J. R., et al. 2017, Revista Mexicana de Astronomia y Astrofisica, 53, 385

Ferland, G. J., Henney, W. J., O'Dell, C. R., & Peimbert, M. 2016, Revista Mexicana de Astronomia y Astrofisica, 52, 261

Ferland, G. J., Korista, K. T., Verner, D. A., Ferguson, J. W., Kingdon, J. B., & Verner, E. M. 1998, Public. of the Astron. Soc. Pac., 110, 761

Ferland, G. J., Porter, R. L., van Hoof, P. A. M., Williams, R. J. R., Abel, N. P., Lykins, M. L., et al. 2013, Revista Mexicana de Astronomia y Astrofisica, 49, 137

Froese Fischer, C. & Tachiev, G. 2004, Atomic Data and Nuclear Data Tables, 87, 1

Gaia Collaboration. 2018, VizieR Online Data Catalog, I/345

Galbany, L., Anderson, J. P., Rosales-Ortega, F. F., Kuncarayakti, H., Krühler, T., Sánchez, S. F., et al. 2016, Mon. Not. of the Royal Astron. Soc., 455, 4087

García-Rojas, J., Corradi, R. L. M., Monteiro, H., Jones, D., Rodríguez-Gil, P., & Cabrera-Lavers, A. 2016, Astrophysical Journal, Letters, 824, L27

García-Rojas, J. & Esteban, C. 2007, Astrophysical Journal, 670, 457

García-Rojas, J., Wesson, R., Boffin, H. M. J., Jones, D., Corradi, R. L. M., Esteban, C., & Rodríguez-Gil, P. 2019, arXiv e-prints, arXiv:1904.06763

Gesicki, K., Zijlstra, A. A., & Morisset, C. 2016, Astron. & Astrophys., 585, A69

Giammanco, C. & Beckman, J. E. 2005, Astron. & Astrophys., 437, L11

Gómez-Llanos, V. & Morisset, C. 2020, Mon. Not. of the Royal Astron. Soc., 497, 3363

Gómez-Llanos, V., Morisset, C., García-Rojas, J., Jones, D., Wesson, R., Corradi, R. L. M., & Boffin, H. M. J. 2020, Mon. Not. of the Royal Astron. Soc., 498, L82

Gómez-Llanos, V., Morisset, C., Szczerba, R., García-Hernández, D. A., & García-Lario, P. 2018, Astron. & Astrophys., 617, A85

Heckathorn, J. 1971, Astrophysics and Space Science, 11, 309

Helou, G. & Walker, D. W. 1988, in Infrared astronomical satellite (IRAS) catalogs and atlases. Volume 7, Vol. 7

Henney, W. J. & Stasińska, G. 2010, Astrophysical Journal, 711, 881

Howarth, I. D. 1983, Mon. Not. of the Royal Astron. Soc., 203, 301

Jones, D., Wesson, R., García-Rojas, J., Corradi, R. L. M., & Boffin, H. M. J. 2016, Mon. Not. of the Royal Astron. Soc., 455, 3263

Juan de Dios, L. & Rodríguez, M. 2017, Mon. Not. of the Royal Astron. Soc., 469, 1036

Kaufman, V. & Sugar, J. 1986, Journal of Physical and Chemical Reference Data, 15, 321

Kingsburgh, R. L. & Barlow, M. J. 1994, Mon. Not. of the Royal Astron. Soc., 271, 257

Kisielius, R., Storey, P. J., Davey, A. R., & Neale, L. T. 1998, Astron. & Astrophys., Supplement, 133, 257

Kisielius, R., Storey, P. J., Ferland, G. J., & Keenan, F. P. 2009, Mon. Not. of the Royal Astron. Soc., 397, 903

Liu, X., Barlow, M. J., Cohen, M., Danziger, I. J., Luo, S., Baluteau, J. P., et al. 2001a, Mon. Not. of the Royal Astron. Soc., 323, 343

Liu, X., Luo, S., Barlow, M. J., Danziger, I. J., & Storey, P. J. 2001b, Mon. Not. of the Royal Astron. Soc., 327, 141

Liu, X.-W., Storey, P. J., Barlow, M. J., & Clegg, R. E. S. 1995, Mon. Not. of the Royal Astron. Soc., 272, 369

Liu, X.-W., Storey, P. J., Barlow, M. J., Danziger, I. J., Cohen, M., & Bryce, M. 2000, Mon. Not. of the Royal Astron. Soc., 312, 585

Luridiana, V., Morisset, C., & Shaw, R. A. 2015, Astron. & Astrophys., 573, A42

Maciel, W. J. & Pottasch, S. R. 1982, Astron. & Astrophys., 106, 1

McNabb, I. A., Fang, X., Liu, X.-W., Bastin, R. J., & Storey, P. J. 2013, Mon. Not. of the Royal Astron. Soc., 428, 3443

Méndez-Delgado, J. E., Esteban, C., García-Rojas, J., Henney, W. J., Mesa-Delgado, A., & Arellano-Córdova, K. Z. 2021, arXiv e-prints, arXiv:2101.02191

Mendoza, C. 1983, in IAU Symposium, Vol. 103, Planetary Nebulae, ed. D. R. Flower, 143–172

Mendoza, C. & Zeippen, C. J. 1982, Mon. Not. of the Royal Astron. Soc., 198, 127

Menon, T. K. & Terzian, Y. 1965, Astrophysical Journal, 141, 745

Menzel, D. H. & Aller, L. H. 1941, Astrophysical Journal, 94, 30

Morisset, C. 2013, pyCloudy: Tools to manage astronomical Cloudy photoionization code

Morisset, C. 2014, in Asymmetrical Planetary Nebulae VI conference, Proceedings of the conference held 4-8 November, 2013. Edited by C. Morisset, G. Delgado-Inglada and S. Torres-Peimbert.

Morisset, C., Delgado-Inglada, G., & Flores-Fajardo, N. 2015, Revista Mexicana de Astronomia y Astrofisica, 51, 103

Morisset, C. & Ercolano, B. 2004, in Astronomical Society of the Pacific Conference Series, Vol. 313, Asymmetrical Planetary Nebulae III: Winds, Structure and the Thunderbird, ed. M. Meixner, J. H. Kastner, B. Balick, & N. Soker, 240–+

Morisset, C., Luridiana, V., García-Rojas, J., Gómez-Llanos, V., Bautista, M., & Mendoza, C. 2020, Atoms, 8, 66

Morisset, C. & Pequignot, D. 1996, Astron. & Astrophys., 312, 135

Morisset, C., Schaerer, D., Bouret, J., & Martins, F. 2004, Astron. & Astrophys., 415, 577

Morisset, C., Schaerer, D., Martín-Hernández, N. L., Peeters, E., Damour, F., Baluteau, J., Cox, P., & Roelfsema, P. 2002, Astron. & Astrophys., 386, 558

Nicholls, D. C., Dopita, M. A., & Sutherland, R. S. 2012, Astrophysical Journal, 752, 148

Nussbaumer, H. & Storey, P. J. 1984, Astronomy and Astrophysics Supplement Series, 56, 293

O'Dell, C. R., Henney, W. J., & Ferland, G. J. 2005, Astronomical Journal, 130, 172

Oliveira, S. & Maciel, W. J. 1986, Astrophysics and Space Science, 126, 211

Osterbrock, D. E. & Ferland, G. J. 2006, Astrophysics of gaseous nebulae and active galactic nuclei (University Science Books)

Owocki, S. P. & Scudder, J. D. 1982, SAO Special Report, 1, A.107

Palay, E., Nahar, S. N., Pradhan, A. K., & Eissner, W. 2012, Mon. Not. of the Royal Astron. Soc., 423, L35

Parker, Q. A., Acker, A., Frew, D. J., Hartley, M., Peyaud, A. E. J., Ochsenbein, F., et al. 2006, Mon. Not. of the Royal Astron. Soc., 373, 79

Peña, M., Ruiz-Escobedo, F., Rechy-García, J. S., & García-Rojas, J. 2017, Mon. Not. of the Royal Astron. Soc., 472, 1182

Peimbert, A. & Peimbert, M. 2013, Astrophysical Journal, 778, 89

Peimbert, M. 1967, Astrophysical Journal, 150, 825

Peimbert, M. 1983, in Primordial Helium, ed. P. A. Shaver, D. Kunth, & K. Kjar, 267–278

Peimbert, M. & Costero, R. 1969, Boletin de los Observatorios Tonantzintla y Tacubaya, 5, 3

Peimbert, M. & Goldsmith, D. W. 1972, Astron. & Astrophys., 19, 398

Peimbert, M., Peimbert, A., & Delgado-Inglada, G. 2017, Public. of the Astron. Soc. Pac., 129, 082001

Peimbert, M., Sarmiento, A., & Fierro, J. 1991, Public. of the Astron. Soc. Pac., 103, 815

Pellegrini, E. W., Rahner, D., Reissl, S., Glover, S. C. O., Klessen, R. S., Rousseau-Nepton, L., & Herrera-Camus, R. 2020, Mon. Not. of the Royal Astron. Soc., 496, 339

Péquignot, D., Amara, M., Liu, X., Barlow, M. J., Storey, P. J., Morisset, C., Torres-Peimbert, S., & Peimbert, M. 2002, in Revista Mexicana de Astronomia y Astrofisica Conference Series, Vol. 12, Revista Mexicana de Astronomia y Astrofisica Conference Series, ed. W. J. Henney, J. Franco, & M. Martos, 142–143

Pequignot, D., Baluteau, J., Morisset, C., & Boisson, C. 1997, Astron. & Astrophys., 323, 217

Péquignot, D., Liu, X., Barlow, M. J., Storey, P. J., & Morisset, C. 2003, in IAU Symposium, Vol. 209, Planetary Nebulae: Their Evolution and Role in the Universe, ed. S. Kwok, M. Dopita, & R. Sutherland, 347

Pequignot, D., Petitjean, P., & Boisson, C. 1991, Astron. & Astrophys., 251, 680

Perinotto, M., Schönberner, D., Steffen, M., & Calonaci, C. 2004, Astron. & Astrophys., 414, 993

Podobedova, L. I., Kelleher, D. E., & Wiese, W. L. 2009, Journal of Physical and Chemical Reference Data, 38, 171

Pottasch, S. R., Baud, B., Beintema, D., Emerson, J., Harris, S., Habing, H. J., et al. 1984, Astron. & Astrophys., 138, 10

Raičević, M., Pawlik, A. H., Schaye, J., & Rahmati, A. 2014, Mon. Not. of the Royal Astron. Soc., 437, 2816

Ramambason, L., Schaerer, D., Stasińska, G., Izotov, Y. I., Guseva, N. G., Vílchez, J. M., Amorín, R., & Morisset, C. 2020, arXiv e-prints, arXiv:2009.09882

Ramsbottom, C. A. & Bell, K. L. 1997, Atomic Data and Nuclear Data Tables, 66, 65

Richer, M. G., Guillén Tavera, J. E., Arrieta, A., & Torres-Peimbert, S. 2019, Astrophysical Journal, 870, 42

Richer, M. G., Suárez, G., López, J. A., & García Díaz, M. T. 2017, Astronomical Journal, 153, 140

Rodríguez, M. 2020, Mon. Not. of the Royal Astron. Soc., 495, 1016

Rodríguez, M. & García-Rojas, J. 2010, Astrophysical Journal, 708, 1551

Rousseau-Nepton, L., Martin, R. P., Robert, C., Drissen, L., Amram, P., Prunet, S., et al. 2019, Mon. Not. of the Royal Astron. Soc., 489, 5530

Rousseau-Nepton, L., Robert, C., Martin, R. P., Drissen, L., & Martin, T. 2018, Mon. Not. of the Royal Astron. Soc., 477, 4152

Rubin, R. H. 1969, Astrophysical Journal, 155, 841

Rybicki, G. B. & Lightman. 1981, Radiative Processes in Astrophysics (WILEY-VCH Verlag GmbH and Co. KGaA), 1–50

Sánchez, S. F. 2020, Annual Review of Astron and Astrophys, 58, annurev

Sánchez, S. F., Kennicutt, R. C., Gil de Paz, A., van de Ven, G., Vílchez, J. M., Wisotzki, L., et al. 2012, Astron. & Astrophys., 538, A8

Schönberner, D., Jacob, R., Sandin, C., & Steffen, M. 2010, Astron. & Astrophys., 523, A86+

Skrutskie, M. F., Cutri, R. M., Stiening, R., Weinberg, M. D., Schneider, S., Carpenter, J. M., et al. 2006, Astronomical Journal, 131, 1163

Slater, J. C. 1930, Physical Review, 36, 57

Smits, D. P. 1996, Mon. Not. of the Royal Astron. Soc., 278, 683

Stasińska, G., Tenorio-Tagle, G., Rodríguez, M., & Henney, W. J. 2007, Astron. & Astrophys., 471, 193

Storey, P. J. 1994, Astron. & Astrophys., 282, 999

Storey, P. J. & Hummer, D. G. 1991, Computer Physics Communications, 66, 129

Storey, P. J. & Hummer, D. G. 1995, Mon. Not. of the Royal Astron. Soc., 272, 41

Storey, P. J., Sochi, T., & Badnell, N. R. 2014, Mon. Not. of the Royal Astron. Soc., 441, 3028

Storey, P. J., Sochi, T., & Bastin, R. 2017, Mon. Not. of the Royal Astron. Soc., 470, 379

Storey, P. J. & Zeippen, C. J. 2000, Mon. Not. of the Royal Astron. Soc., 312, 813

Sutherland, R. S. & Dopita, M. A. 1993, Astrophysical Journal, Supplement, 88, 253

Sutherland, R. S. & Dopita, M. A. 2017, Astrophysical Journal, Supplement, 229, 34

Tayal, S. S. 2011, Astrophysical Journal, Supplement, 195, 12

Tayal, S. S. & Zatsarinny, O. 2010, Astrophysical Journal, Supplement, 188, 32

Torres-Peimbert, S. & Peimbert, M. 1977, Revista Mexicana de Astronomia y Astrofisica, 2, 181

Torres-Peimbert, S., Peimbert, M., & Daltabuit, E. 1980, Astrophysical Journal, 238, 133

Torres-Peimbert, S., Peimbert, M., & Pena, M. 1990, Astron. & Astrophys., 233, 540

Tsamis, Y. G., Barlow, M. J., Liu, X., Storey, P. J., & Danziger, I. J. 2004, Mon. Not. of the Royal Astron. Soc., 353, 953

Tsamis, Y. G. & Pequignot, D. 2004, arXiv e-prints, astro

Tsamis, Y. G. & Péquignot, D. 2005, Mon. Not. of the Royal Astron. Soc., 364, 687

Tsamis, Y. G., Walsh, J. R., Péquignot, D., Barlow, M. J., Danziger, I. J., & Liu, X. 2008, Mon. Not. of the Royal Astron. Soc., 386, 22

Tylenda, R., Siódmiak, N., Górny, S. K., Corradi, R. L. M., & Schwarz, H. E. 2003, Astron. & Astrophys., 405, 627

Vale Asari, N., Stasińska, G., Morisset, C., & Cid Fernandes, R. 2016, Mon. Not. of the Royal Astron. Soc.

Viegas, S. M. & Clegg, R. E. S. 1994, Mon. Not. of the Royal Astron. Soc., 271, 993

Wesson, R., Jones, D., García-Rojas, J., Boffin, H. M. J., & Corradi, R. L. M. 2018, Mon. Not. of the Royal Astron. Soc., 480, 4589

Wesson, R., Liu, X., & Barlow, M. J. 2005, Mon. Not. of the Royal Astron. Soc., 362, 424

Wood, K., Mathis, J. S., & Ercolano, B. 2004, Mon. Not. of the Royal Astron. Soc., 348, 1337

Wyse, A. B. 1942, Astrophysical Journal, 95, 356

Yuan, H., Liu, X., Péquignot, D., Rubin, R. H., Ercolano, B., & Zhang, Y. 2011, Mon. Not. of the Royal Astron. Soc., 411, 1035

Zhang, Y., Liu, X. W., Wesson, R., Storey, P. J., Liu, Y., & Danziger, I. J. 2004, Mon. Not. of the Royal Astron. Soc., 351, 935